8-2014

Modified-Electrodes for Redox-Magnetohydrodynamic (MHD) Pumping for Microfluidic Applications

Christena Kayl Nash
University of Arkansas, Fayetteville

Modified-Electrodes for Redox-Magnetohydrodynamic (MHD) Pumping for Microfluidic Applications

Modified-Electrodes for Redox-Magnetohydrodynamic (MHD) Pumping for Microfluidic Applications

A dissertation submitted in partial fulfillment
of the requirements for the degree of
Doctor of Philosophy in Chemistry

by

Christena Nash
University of Arkansas
Bachelor of Science in Chemistry, 2009
University of Arkansas
Master of Arts in Teaching in Secondary Education, 2010

August 2014
University of Arkansas

This dissertation is approved for recommendation to the Graduate Council.

_____
Dr. Ingrid Fritsch
Dissertation Director

_____
Dr. Bill Durham
Committee Member

_____
Dr. David Paul
Committee Member

_____
Dr. Charles Wilkins
Committee Member

Abstract

A new microfluidic pumping and stirring technique was demonstrated for lab-on-a-chip applications. Microfluidics was accomplished via redox-MHD, which takes advantage of a body force ($\mathbf{F_B}$) that is generated when there is a net movement of ions in solution (**j**) in the presence of a perpendicular magnetic field (**B**), according to the equation $\mathbf{F_B} = \mathbf{j} \times \mathbf{B}$. In this work the movement of ions in solution was generated using electrodes modified with the conducting polymer poly(3,4-ethylenedioxythiophene) (PEDOT) rather than a redox species in solution, which can interfere with analyte detection and with biological species. The monomer solution and electrochemical method used for electrodeposition has a profound effect on the morphology and the electrochemical behavior of the film. These conditions were investigated to improve the properties of the PEDOT film for redox-MHD applications, such as coulombic capacity, current response, and electrochemical stability. PEDOT-modified microband electrodes were shown to be effective for microfluidic pumping applications, exhibiting a fairly flat flow across a 5600 μm gap. PEDOT-modified concentric ring-disk electrodes demonstrated a rotational fluid flow with non-uniform velocity between the disk and ring electrodes. This created a spiraling fluid flow that could be useful for stirring applications. PEDOT-modified electrodes were shown to be capable of initially high currents, and therefore velocities (up to 980 $\mu m \cdot s^{-1}$ at microband electrodes during an applied potential experiment), until the film was exhausted, limiting the time scale of pumping. This limitation was solved by taking advantage of the reversible nature of PEDOT. The bias of the PEDOT-modified electrodes was switched by applying a sinusoidal potential waveform while a synchronized potential waveform was driving an electromagnet under the chip, creating an AC magnetic field. This generated continuous fluid flow in a single direction. AC redox-MHD pumping was demonstrated at PEDOT-modified microband electrodes (115 $\mu m \cdot s^{-1}$) and at concentric ring-disk electrodes (<268 $\mu m \cdot s^{-1}$) for pumping and stirring applications respectively.

Acknowledgements

First and foremost, I would like to express my gratitude to Dr. Ingrid Fritsch. I have learned so much from her over the years. From her classes to her mentoring my research project, she has molded me into the scientist I am today. This research is her brain-child, and I have been lucky to work on such an innovative project. Working with her has truly been a privilege.

I would also like to thank my committee members, Dr. Bill Durham, Dr. David Paul, and Dr. Charles Wilkins. Their discussions have always been insightful and thought provoking, offering decades of scientific exploration experience.

I am appreciative of the years of support given by Jerry Homesley. His services go far beyond keeping instruments running. I learned design and problem solving skills and benefitted greatly from his extensive knowledge of circuitry.

I am especially thankful to my family for their years of unfailing support throughout my educational journey. I thank my parents especially for teaching me a healthy work ethic and the importance of finishing what I have started. Their unconditional love and support have made all of this possible.

I would especially like to thank my husband, Will. His support has always been a crucial part of my academic success, even more so at the end. Thank you for taking amazing care of me while I finished this degree and serving as a reminder that there is a life after graduate school. Being your wife is my honor and privilege.

I would like to thank Rogena Sheets and Marsha Petty, two of my most influential teachers in high school. I very strongly disliked science until I took their classes. This truly would not have been possible without their influence.

Research was supported through the National Science Foundation (NSF) (CHE-0719097 and CBET-1336853) and the Arkansas Biosciences Institute, the major research component of the Arkansas Tobacco Settlement Proceeds Act of 2000.

Table of Contents

1. Introduction to Redox-MHD at PEDOT-Modified Microelectrodes

1.1 Introduction

Microfluidics is the technology of manipulating small amounts of fluid in a system. Microfluidics hold certain advantages in the field of analysis including small sample and reagent volumes, low cost, shorter analysis times, ability to carry out separation and detection with high resolution and sensitivity, and portability.[1-3] The field has grown as genomics, proteomics, and drug discovery has become more crucial. [3, 4] In a microfluidic system, the device must have a way of introducing reagents and samples, the ability to pump and/or mix components, and means to detect (if analysis is the ultimate goal).[5] This work will focus on a new method for the pumping and mixing of fluid in a microfluidic device. As this field has grown, the need for miniaturizing pumping methods has also grown. In larger systems, effects such as magnetohydrodynamics, electrochemical, acoustic streaming, and electrokinetic have been ignored due to their negligible effects to fluid movement of large volumes.[4] In these systems those effects are no longer negligible in all cases and can be exploited to move solution through the device. Ideally, a microfluidic pumping system should be relatively easy to fabricate, require low power, and take advantage of inexpensive materials to move a variety of solutions in controlled directions.

Micropumps are classified as either mechanical or non-mechanical depending on whether external mechanical or non-mechanical energy (i.e. electrical, optical, thermal, acoustic, and magnetic energies) is converted to kinetic energy.[6] Mechanical pumps use moving parts to move a constant amount of solution per cycle. Because of these moving parts such as valves, oscillating membranes, and turbines, mechanical pumps are difficult to miniaturize and require complicated fabrication procedures. Also, reversing flow in these systems requires additional valves. Non-mechanical pumps add momentum to the solution through the conversion of some form of energy into kinetic energy. For example, electrohydrodynamic pumps utilize the electrostatic forces which act upon dielectric fluids to move solution and electro-kinetic pumps move conductive fluids by applying an electric field, providing a flat flow profile without high external pressures. Electro-hydrodynamic pumps are limited by the electrical properties of the fluids and require very high electric fields. Electrokinetic pumps require high voltages, which can cause bubble generation from the electrolysis of water.

Magnetohydrodynamics (MHD) works under the application of electric and magnetic fields perpendicular to each other and generates a body force which induces the fluid convection. MHD provides a novel method for manipulating fluid flow which can be used to overcome some of the disadvantages of the previously discussed techniques. MHD micropumps take advantage of the magnetic portion of the Lorentz force equation, the magnetohydrodynamic force, $\mathbf{F_B}$. MHD force in a fluid is generated by the movement of ions perpendicular to a magnetic field, producing a force that has a direction perpendicular to both the ion movement and the magnetic field:

$$\mathbf{F_B} = \mathbf{j} \times \mathbf{B}$$

where $\mathbf{F_B}$ ($N \cdot m^{-3}$) is the magnetic portion of the Lorentz force, $\mathbf{j}$ ($C \cdot m^{-2} \cdot s^{-1}$), ionic current density, is the net movement of ions in a unit volume of the fluid, and $\mathbf{B}$ is the magnetic flux density (T).[7] Figure 1.1 illustrates the forces involved in MHD convection at (a) microband electrodes and between (b) concentric microdisk and ring electrodes. Permanent magnets or electromagnets can be used to generate the magnetic field needed for convection. The ion flux is created by electron transfer reactions and positive $\mathbf{j}$ is defined as the movement of positive ions.

To prevent the production of bubbles from electrolysis of water, corrosion of anode electrode materials, and oxidation or reduction of electrolyte when large overpotentials are applied to generate flux, electroactive species are added to the electrolyte to generate current and ion flux and serve as the “pumping” species. With the addition of redox species, low voltages are required to generate enough current for pumping applications and bubbles are avoided.[8, 9] Redox MHD has some attractive features for microfluidic applications such as channel-less, no moving parts, easily fabricated devices, and bi-directional pumping, convection, and stirring. Through programming which electrodes are active at certain times and by careful design of the placement and geometry of electrodes on a chip, fine-tuned fluid control is possible without channels, greatly simplifying device fabrication. Also, the conducting medium can be non-aqueous or aqueous, making it a good candidate for either synthetic organic chemistry or biological applications. The addition of redox species keeps voltages low, and bubble generation is avoided. Video microscopy of the fluid in which beads have been added make it possible to

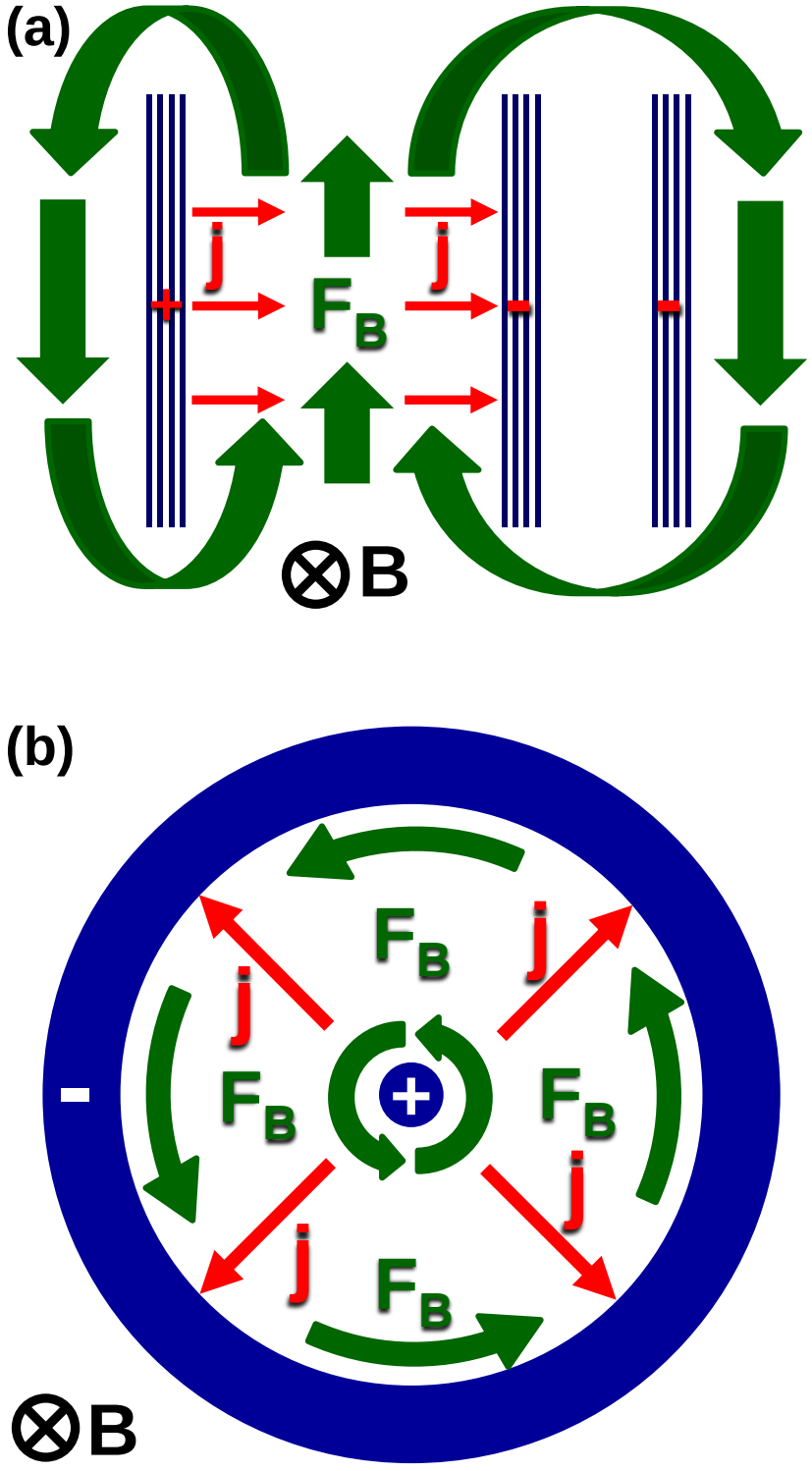

Figure 1.1. (a) Illustration of MHD at PEDOT-modified microband electrodes. (b) Illustration of MHD at PEDOT-modified concentric microdisk and ring electrodes.

map fluid flow velocity and flow patterns as a function of a variety of experimental parameters.[7, 8, 10, 11]

The inspiration for this research comes from concerns that the addition of redox species could interfere with analytical detection or with biological species. Low concentrations of redox species have been shown to have compatibility with alkaline phosphatase, an enzyme commonly used in immunoassay applications.[12] It has also been shown to be compatible with viable heart tissue.[13] Nonetheless, it is still desirable to avoid the need to add chemicals to a sample, which would otherwise require careful scrutiny of selecting a redox species based on an application-to-application basis. One method of alleviating this issue is to immobilize the redox species on the electrode surface to limit the interaction between the redox species and the solution containing the sample.

There are multiple ways of immobilizing redox species to an electrode surface. First, redox species can be entrapped or electrostatically bound into thin polymer films on electrode surfaces. This has been done with polymer-redox couples such as ruthenium (II) hexaammine or ruthenium (II) bipyridine in insulating polymers of Nafion and ferri and ferrocyanide in poly-vinyl pyridine.[14-16] This method raises concerns of the redox species leaching over time leading to ever decreasing currents. Also, polymer films can slow down electron transfer and must allow for charge compensation from ions in the adjacent solution. Another way of immobilizing redox species to an electrode surface is through covalent attachment of a redox center to the polymer. Metallopolymers, especially ruthenium or osmium complexes covalently attached to poly-vinyl pyridine have received a lot of attention due to their stability, fast electron-exchange dynamics, efficient charge-transport rates, and their synthetic flexibility.[17, 18] These metallopolymers are not widely available and must be synthesized as needed. Yet another way of confining redox species is to utilize the oxidation and reduction properties of conducting polymers. Conducting polymers have recently attracted much attention in the biosensor and biofuel cell community because of their rapid electron transfer characteristics and ability to immobilize biomolecules.[19] Conducting polymers have low ionization potential, high electron affinity, and electrical conductivity due to their π–electron backbones, which also make them very susceptible to oxidation and reduction

reactions.[20] Electrochemical polymerization is quickly becoming the preferred method of preparing conducting polymer films. This method of preparation has several advantages over other synthesis including reproducibility, control of film thickness with varying potential or current with time, and well-defined areas of polymer deposition.[21] Commonly used conducting polymers include polypyrrole, polyaniline, polyacetylene, polythiophene, and polyphenylene.

Poly(3,4-ethylenedioxythiophene) (PEDOT), a conducting polymer in the polythiophene family, has been the most successful immobilized redox species for generating MHD thus far. It is a stable conducting polymer whose electrochemical and spectrochemical properties have made it an attractive material in a variety of applications including antistatic coatings, solid electrolyte capacitors, chemical sensors, field effect transistors, photovoltaic cells, light emitting diodes, and biosensors.[22-24] Conducting polymers have alternating double and single bonds between the carbon atoms in the polymer backbone. This bond conjugation is responsible for the electrical conductivity of PEDOT.[25] PEDOT can be prepared using standard oxidative chemical polymerization or electrochemical polymerization. [26] The advantages that electrochemical polymerization offers are: (1) requires small amounts of the monomer; (2) the films produced are uniform and adherent; (3) dopants are incorporated into the film as it is produced; (4) PEDOT can be deposited on desired electrode geometries with good spatial resolution; (5) film thickness can be controlled by the number of growth cycles (for potentiodynamic methods) or by the deposition time (for chonoponentiometric methods).[27, 28]

PEDOT can be electropolymerized in both aqueous and organic solvents. Electrosynthesis of PEDOT is more difficult in aqueous media because thiophene containing compounds are weakly soluble in water, its oxidation potential is higher than water, and the thienyl cation radicals which are formed during polymerization readily react with water.[29] Sakmeche et al. found that adding anionic surfactant, sodium dodecyl sulfate (SDS), increases the solubility of thiophenes as well as lowers its oxidation potential.[29-31] The ability to electropolymerize in aqueous solutions is important for biochemical applications.

For the MHD experiments, the same chip design was used for consistency. The chip contained three sets of four microband electrodes (100 μm × 2.5 cm) with a 5600 μm gap

between the first and second sets and a 2000 µm gap between the second and third sets. The chip also contained four concentric disk and ring electrodes of varying sizes. The largest two disk and ring electrode sets are used in this study. The work done in Chapter 2 had a disk diameter of 160 µm and the ring electrode had an inner diameter of 1600 µm and an outer diameter of 2000 µm. The work performed in Chapter 4 used a disk electrode with a diameter of 320 µm and a ring electrode with an inner diameter of 3200 µm and an outer diameter of 4000 µm. An autocad design of the chip and the geometries used in this work are found in Figure 1.2.

For all of the MHD studies described in this work, 10 µm (diameter) polystyrene beads were added to solution to visualize the fluid flow. The fluid flow was viewed under a microscope and recorded using an interfaced video camera. The recorded fluid flow was quantified using particle imaging velocimetry (PIV) analysis. PIV basically divides the video into square interrogation regions and identifies bead patterns that move through them through subsequent frames. PIV then takes the displacement of the bead patterns and divides by the time between frames to obtain the velocity vector for each interrogation region, producing a flow profile.

In Chapter 2, PEDOT-modified microband electrodes were used to demonstrate the microfluidic MHD-pumping capabilities. A relatively flat fluid flow profile was observed between the 5600 µm gap between the working and counter microband electrodes. Using potential step, impressive velocities were achieved, but could not be maintained for long time periods. Using applied current, fluid flow could be sustained for longer periods of time, but at lower velocities. Both horizontal and vertical fluid flow profiles were examined in this chapter.

Chapter 3 focuses on PEDOT-modified concentric microdisk and ring electrodes for generating rotational flow. It was demonstrated that the velocity changes radially from the disk electrode according to the ionic current density. The flow profile throughout the height of the cell was illustrated using contour plots. The majority of the fluid flow occurs at height below 600 µm above the chip because the horizontal component of the ionic current density is strongest there. This rotational flow could be of use in stirring applications (such as on-chip reaction and incubation) and eventually in microfluidic mixing applications.

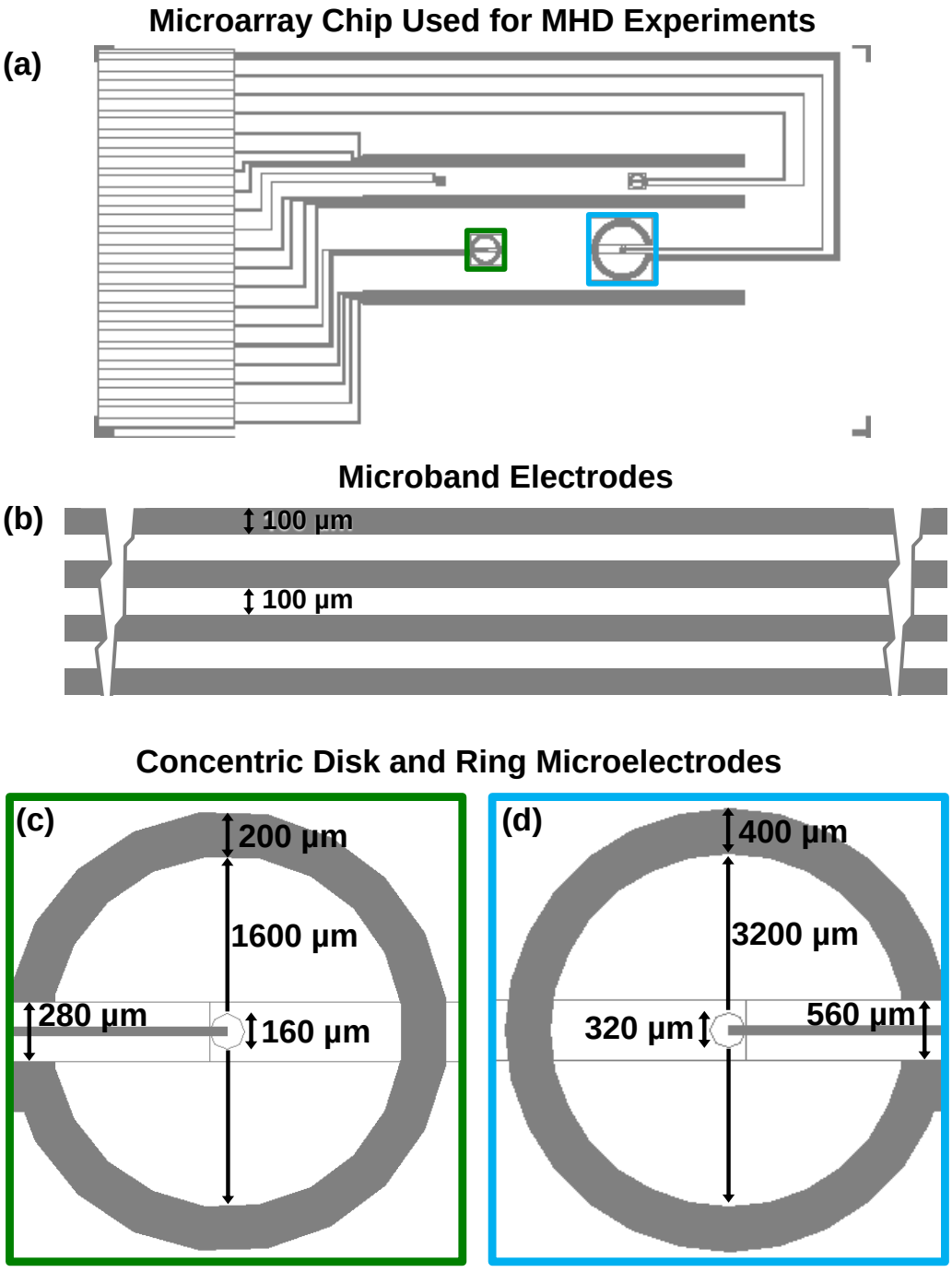

Figure 1.2. (a) Autocad design of electroarray chip used for MHD experiments performed in this work. (b) Expanded view of microband electrodes (100 µm × 2.5 cm) used for pumping. (c) Expanded view of concentric disk (160 µm dia.) and ring (1600 µm inner dia.; 2000 µm outer dia.) electrodes used in Chapter 2. (d) Expanded view of concentric disk (320 µm dia.) and ring (3200 µm inner dia.; 4000 µm outer dia.) electrodes used in Chapter 4.

Chapter 4 is a study on the effect of electropolymerization conditions on the properties of PEDOT films to improve the coulombic capacity of the films, the current response time, and the stability of the film. Four different solubilizers were used: sodium dodecyl sulfate, bis(2-ethylhexyl) sulfosuccinate, 4-dodecylbenzenesulfonic acid, and polystyrene sulfonate. The films were deposited using cyclic voltammetry and the number of deposition cycles was varied. The PEDOT films were characterized electrochemically using cyclic voltammetry, chronoamperometry, and electrochemical impedance spectroscopy. Scanning electron microscopy was used to examine the morphology of the films.

Chapter 5 explores AC-MHD at PEDOT-modified electrodes to extend the amount of time pumping can be sustained. A sinusoidal potential waveform is applied to PEDOT-modified electrodes and is synchronized with an AC magnetic field. Fluid flow profiles were examined at microband electrodes and at concentric microdisk and ring electrodes.

Chapter 6 addresses the impact of DC- and AC-MHD micropumping at PEDOT-modified electrodes and lessons learned from electropolymerizing thick PEDOT films. Future directions are envisioned and discussed.

This dissertation is written in a format that is compatible to be published in peer reviewed journals. An individual chapter has the main text and the supporting information at the end of each chapter. Chapters, sections, and figures pertaining to the supplemental information are labeled as Chapter Number.S.

1.2 References

(1) Polson, N. A.; Hayes, M. A. *Analytical chemistry* **2001**, *73*, 312 A-319 A.

(2) Whitesides, G. M. *Nature* **2006**, *442*, 368-373.

(3) Figeys, D.; Pinto, D. *Analytical Chemistry* **2000**, *72*, 330 A-335 A.

(4) Nguyen, N.-T.; Huang, X.; Chuan, T. K. *Journal of Fluids Engineering* **2002**, *124*, 384-392.

(5) Stone, H. A.; Stroock, A. D.; Ajdari, A. *Annu. Rev. Fluid Mech.* **2004**, *36*, 381-411.

(6) Amirouche, F.; Zhou, Y.; Johnson, T. *Microsystem Technologies* **2009**, *15*, 647-666.

(7) Weston, M. C.; Gerner, M. D.; Fritsch, I. *Analytical Chemistry*, *82*, 3411-3418.

(8) Anderson, E. C.; Weston, M. C.; Fritsch, I. *Analytical Chemistry*, *82*, 2643-2651.

(9) Weston, M. C.; Nash, C. K.; Fritsch, I. *Analytical Chemistry*, *82*, 7068-7072.

(10) Fritsch*, M. C. W. a. I. *Sensors and Actuators B* **Submitted**.

(11) Preston G. Scrape, M. D. G., Melissa C. Weston, and Ingrid Fritsch* *Analytical Chemistry* **Soon to be submitted**.

(12) Weston, M. C.; Nash, C. K.; Fritsch, I. *Analytical Chemistry* **2010**, *82*, 7068-7072.

(13) Cheah, L. T.; Fritsch, I.; Haswell, S. J.; Greenman, J. *Biotechnology and Bioengineering* **2012**, *109*, 1827-1834.

(14) Buttry, D. A.; Anson, F. C. *Journal of the American Chemical Society* **1983**, *105*, 685-689.

(15) Bertoncello, P.; Ciani, I.; Marenduzzo, D.; Unwin, P. R. *The Journal of Physical Chemistry C* **2006**, *111*, 294-302.

(16) Fritsch-Faules, I.; Faulkner, L. R. *Analytical Chemistry* **1992**, *64*, 1118-1127.

(17) Wang, B.; Brown, S.; Rusling, J. F. *Electroanalysis* **2005**, *17*, 1601-1608.

(18) Forster, R. J.; Vos, J. G.; Lyons, M. E. G. *Journal of the Chemical Society, Faraday Transactions* **1991**, *87*.

(19) Vidal, J.-C.; Garcia-Ruiz, E.; Castillo, J.-R. *Microchimica Acta* **2003**, *143*, 93-111.

(20) Malhotra, B. D.; Chaubey, A.; Singh, S. P. *Analytica Chimica Acta* **2006**, *578*, 59-74.

(21) Gerard, M.; Chaubey, A.; Malhotra, B. D. *Biosensors and Bioelectronics* **2002**, *17*, 345-359.

(22) Wang, X.; Sjoberg-Eerola, P.; Eriksson, J.-E.; Bobacka, J.; Bergelin, M. *Synthetic Metals* **2010**, *160*, 1373-1381.

(23) Poverenov, E.; Li, M.; Bitler, A.; Bendikov, M. *Chemistry of Materials* **2010**, *22*, 4019-4025.

(24) Bobacka, J.; Lewenstam, A.; Ivaska, A. *Journal of Electroanalytical Chemistry* **2000**, *489*, 17-27.

(25) Tamburri, E.; Orlanducci, S.; Toschi, F.; Terranova, M. L.; Passeri, D. *Synthetic Metals* **2009**, *159*, 406-414.

(26) Groenendaal, L.; Jonas, F.; Freitag, D.; Pielartzik, H.; Reynolds, J. R. *Advanced Materials* **2000**, *12*, 481-494.

(27) Kumar, S.; Mathiyarasu, J.; Phani, K.; Yegnaraman, V. *Journal of Solid State Electrochemistry* **2006**, *10*, 905-913.

(28) Xiao, Y.; Li, C. M.; Wang, S.; Shi, J.; Ooi, C. P. *Journal of Biomedical Materials Research Part A* **2009**, *92A*, 766-772.

(29) Sakmeche, N.; Aeiyach, S.; Aaron, J.-J.; Jouini, M.; Lacroix, J. C.; Lacaze, P.-C. *Langmuir* **1999**, *15*, 2566-2574.

(30) Sakmeche, N.; Bazzaoui, E. A.; Fall, M.; Aeiyach, S.; Jouini, M.; Lacroix, J. C.; Aaron, J. J.; Lacaze, P. C. *Synthetic Metals* **1997**, *84*, 191-192.

(31) Manisankar, P.; Vedhi, C.; Selvanathan, G.; Gurumallesh Prabu, H. *Journal of Applied Polymer Science* **2007**, *104*, 3285-3291.

2. Poly(3,4-ethylenedioxythiophene)-Modified Microband Electrodes for Magnetohydrodynamic (MHD) Microfluidics

2.1 Abstract

A new approach using electrodes modified with poly(3,4-ethylenedioxythiophene) (PEDOT) was investigated for implementing redox-magnetohydrodynamics (Redox-MHD) for microfluidics, making it possible to eliminate redox species in solution, thus addressing concerns about redox species interfering with detection, sample, and biological reagents for lab-on-a-chip applications. PEDOT, a biocompatible conducting polymer, was electropolymerized on microband gold electrodes (25 mm long $\times$ 103.0 μm wide ± 0.1 μm). A cell with distant side walls containing a volume of 325 μL was formed by placing a 620 μm thick poly(dimethyl siloxane), PDMS, gasket with an opening of 3.2 cm $\times$ 1.5 cm on the chip and a glass slide resting on the PDMS gasket served as the ceiling preventing evaporation. A 0.37 T magnet was placed under the chip to generate a magnetic field perpendicular to the chip surface. The cell was filled with 0.0950 M NaCl electrolyte and 10 μm polystyrene beads to visualize and quantify fluid flow using video microscopy. Fluid speeds as high as 550.0 μm/s were observed during the initial 0.1667 s after applying a potential step. Current and fluid velocities that were 80 times higher than past studies involving unmodified electrodes and redox species in solution were observed. A linear relationship between applied current and the fluid velocity was shown. Vertical and horizontal flow profiles were examined for applied current experiments, revealing a parabolic vertical flow profile and a generally flat horizontal flow profile. These results show promise for the implementation of PEDOT-modified electrodes for MHD-based microfluidic applications.

2.2 Introduction

Microfluidic devices hold certain advantages in the field of analysis including small sample and reagent volumes, low cost, shorter analysis times, portability, and ability to carry out separations and detection with high resolution and sensitivity.[1] The field of microfluidics has grown as genomics, proteomics, and drug discovery have become important fields of study.[2] In a microfluidic system, the device must have a way of introducing reagents and samples, the ability to pump and/or mix components, and a means to detect (if analysis is the ultimate goal). MHD pumping has found a niche in microfluidic applications.[3-6]

MHD micropumps take advantage of the magnetic portion of the Lorentz force, the magnetohydrodynamic force, $\mathbf{F_B}$ (N/m^3). The MHD force is generated by the movement of ions perpendicular to a magnetic field, producing a force that is perpendicular to both the movement of ions and the magnetic field according to the equation:

$$\mathbf{F_B} = \mathbf{j} \times \mathbf{B}$$

where $\mathbf{j}$ ($C/m \cdot s^2$), ionic current density, is the net movement of ions in a unit volume, and $\mathbf{B}$ (T) is the magnetic flux density.[3] In redox-MHD, the ionic current results from electron transfer reactions at the electrode-solution interface, where the positive $\mathbf{j}$ is defined as in the direction of movement of positive ions. The addition of chemical species that can undergo electrochemistry at less extreme applied voltages prevents the generation of bubbles from electrolysis of water and prevents the corrosion of electrode material.[6, 7] Redox-MHD has some attractive features for microfluidic applications such as no moving parts, easily fabricated devices, and bi-directional pumping and rotational flow.[8] Fine-tuned fluid control is possible without channels through programming the activation of different electrodes and by careful design of the placement and geometry of electrodes on a chip. The lack of the need for channels greatly simplifies device fabrication.

Concerns of interference of the added redox species with detection and of compatibility issues with biological species have arisen. Low concentrations of ruthenium (II/III) hexaammine (i.e. 5 mM) were used to pump a plug of *p*-aminophenyl phosphate through a solution filled with

alkaline phosphatase, an enzyme used in ELISA. Alkaline phosphatase maintained its activity in low concentration of ruthenium hexaammine, but the pumping speeds were limited by the low concentration. It is also important to note that in one example, low concentrations of a redox couple did not interfere with the biological samples in terms of heart tissue viability, but did affect the sensitivity of the lactate dehydrogenase assay.[7, 9] Nonetheless, it is still desirable to avoid the need to add additional chemicals to a sample, whose selection would require careful scrutiny on an application-to-application basis. We recently showed that in redox-MHD, only supporting electrolyte is required between electrodes to perform MHD microfluidics, and that the redox species are only needed at the activated electrodes to maintain the faradaic current.[10] This important outcome suggests that MHD microfluidics should be possible by immobilizing the redox species to the electrode surfaces, thereby limiting its interaction with the sample and detection downstream. That concept is demonstrated herein.

Poly(3,4-ethylenedioxythiophene) (PEDOT) is a stable conducting polymer whose electrochemical and spectrochemical properties have made it an attractive material in a variety of applications including antistatic coatings, solid electrolyte capacitors, chemical sensors, field effect transistors, photovoltaic cells, light emitting diodes, and biosensors.[11-13] Conducting polymers have bond conjugation along the polymer backbone, which is responsible for the electrical conductivity of PEDOT.[14] The polymer can be prepared using standard oxidative chemical or electrochemical polymerization.[15] The advantages that electrochemical polymerization offers are: (1) that it requires small amounts of the monomer; (2) the films produced are uniform and adherent; (3) dopants are incorporated into the film as it is produced; (4) it can be deposited on desired electrode geometries with good spatial resolution; (5) film thickness can be controlled by the number of growth cycles (for potentiodynamic methods) or by the deposition time (for chronopotentiometric and chronoamperometric methods).[11, 12, 16-23]

PEDOT can be electropolymerized in both aqueous and organic solvents. Electrosynthesis of PEDOT is more difficult in aqueous media because thiophene-containing compounds are weakly soluble in water, its oxidation potential is higher than water, and the thienyl cation radicals which are formed during polymerization readily react with water.[24]

Sakmeche et al. found that adding anionic surfactant, sodium dodecyl sulfate (SDS), increases the solubility of thiophenes as well as lowers its oxidation potential.[24-26] The ability to electropolymerize in aqueous solutions is important for some biochemical applications.[11] PEDOT has also found a niche in the biosensor community due to its high conductivity, high stability, high transparency, and cost efficiency.[27] PEDOT-modified electrodes have been used in the study of neural processes because of its stability in biological environments, showing improvements in long-term performance.[28, 29] They have been found effective for the detection of dopamine in the presence of ascorbic acid and other interferents.[16, 30, 31] PEDOT has also been used to entrap enzymes during electrodeposition for biosensor applications.[17, 27, 32-36]

In the work presented here, PEDOT was electropolymerized onto gold microband electrodes and MHD microfluidic pumping was performed using an applied potential step (chronoamperometry) and an applied constant current (chronopotentiometry) in the presence of a permanent NdFeB magnet. Fluid velocities were investigated over time by tracking microbeads in electrolyte solution of 0.0950 M NaCl in a cell containing the PEDOT-modified electrodes. Chronopotentiometry was used to control the fluid velocity and to extend the time that flow could be sustained.

2.3 Experimental Section

2.3.1 Chemicals and Materials. Aqueous solutions were made with reagent grade, 18 megohm, deionized water from Ricca Chemical Company (Arlington, TX). Potassium chloride was purchased from VWR International LLC (West Chester, PA). Sodium dodecyl sulfate was bought from AMRESCO (Solon, OH). 3,4-ethylenedioxythiophene was obtained from Sigma-Aldrich (St. Louis, MO). Sodium chloride was obtained from EMD Chemicals Inc. (Gibbstown, NJ). Polystyrene latex microspheres, 10.0 μm diameter (2.5 wt% dispersion in water) and ruthenium(II) hexaammine for characterizing the bare gold electrodes before modification were purchased from Alfa Aesar (Ward Hill, MA). The as-received ruthenium(II) hexaammine chloride contained the oxidized form, as well, resulting in near 1:1 mixture of each species. The substrate materials for the electrode arrays were silicon wafers (125-mm diameter and 600-650-μm thick with 2 μm of thermally grown SiO_2 on the surface) and purchased from Silicon Quest International

(Santa Clara, CA). To form the electrode arrays, a chromium-plated tungsten rod (Kurt J. Lesker Company, Clairton, PA) and gold pieces cut from a coin (Canadian Maple Leaf, 99.99%) and placed in a molybdenum boat (Kurt J. Leskar Company, Pittsburg, PA) were used for metal deposition onto silicon wafers. Wafers were cleaned using Radio Corporation of America (RCA) procedure. Positive photoresist (AZ 4330) was used for the gold electrode pattern transfer from photo plot masks (Advance Reproductions Corporation, North Andover, MA) to the silicon wafer. To remove excess photoresist in the photolithography process, tetramethyl ammonium hydroxide (TMAH) solution was used as a developer. Gold etchant (Transene, GE8148) and chromium etchant (HTA enterprise, CEP200) were used as received. To insulate the electrode leads, Benzocyclobutene, BCB, (Cyclotene 4024-40) was used and purchased from Dow Corning Company (Midland, MI). A detailed procedure of the microfabrication used can be found in work previously done in our group.[37] Connection from the chip to the potentiostat was made via an edge connector (solder contact, 20/40 position, 0.05 in. pitch) purchased from Sullins Electronics Corp. (San Marcos, CA). A poly(dimethyl siloxane), PDMS, gasket was fabricated using Sylgard184 silicon elastomer base, Sylgard 184 silicon elastomer curing agent and OS-30 solvent (Ellsworth Adhesives, Milwaukee, WI). Pre-cleaned microscope glass slides (1.5 × 1.0 × 0.1 $in.^3$) were obtained from VWR.

2.3.2 Microelectrode Chips and Electrochemical Control. A detailed description of the fabrication process of these chips can be found in previously published work.[6] The chips are 1 in. × 2 in. The design on the chip includes 12 microband electrodes which are in three sets of four (each electrode is 100 µm wide and 2.5 cm long with a 100 µm gap between electrodes in the set) and four sets of concentric ring and disk electrodes varying in size (Figure 2.1a), however, only microband electrodes were used for this work. A CHI 760B bipotentiostat (CH Instruments, Austin, TX) was used to perform cyclic voltammetry (CV), chronoamperometry (CA), and chronopotentiometry (CP). The microband electrodes were characterized before and after deposition of PEDOT in electrolyte alone, 0.100 M NaCl, and in a solution-based redox species, 5 mM $Ru(NH_3)_6^{2+/3+}$ and 0.100 M NaCl. The characterization experiments were done using a two-electrode configuration where four band electrodes were shorted together as the working

electrode and the remaining eight microband electrodes served as the auxiliary and quasi-reference electrode. The characterization experimental results are discussed in the supplementary information section.

2.3.3 Preparation of PEDOT-modified gold microelectrodes. Monomer 3,4-ethlenedioxythiophene (EDOT) was electropolymerized and deposited onto an array of gold microelectrodes. The chip was cleaned using an oxygen plasma cleaner prior to deposition. An aqueous solution of 0.0100 M EDOT in 0.0100 M SDS in 0.100 M potassium chloride was prepared and sonicated for 1 h. EDOT was polymerized onto the electrode by cycling the potential from -0.455 V to 1.125 V vs a Ag/AgCl (saturated KCl) reference electrode at 0.005 V/s. The PEDOT film was allowed to grow for six successive scans, depositing a dark blue film; electrodes remained individually addressable (Figure 2.1b). A platinum flag was used as the auxiliary electrode.

2.3.4 Experimental Setup. In all of the MHD experiments described below, a PDMS gasket (620 μm thick when dry with a rectangular opening cut out of 3.2 cm $\times$ 1.5 cm) defined the dimensions of the cell (Figure 2.1b). The opening in the PDMS gasket was wide enough that the pumping electrodes were more than 1 mm away from the walls, therefore containing the solution, while not defining any sort of channel. A glass slide was placed on top of the PDMS gasket to serve as a ceiling of the cell and limit movement in the vertical direction (Figure 2.1a). It should be noted that the height of the cell was higher than the dry height of the PDMS gasket due to a thin layer of solution between it and the glass. The experimental cell height was 750 μm when 325 μL of solution was added to the cell. The chip and gasket were placed onto a NdFeB cylindrical permanent magnet (diameter of 1.5 in. and height of 0.5 in., Amazing Magnets LLC, Irvine, CA) and positioned so that it was centered over active microband electrodes. A magnetic field of 0.37 T was measured at the array with a dc magnetometer, AlfaLab, Inc (Salt Lake City, UT).

2.3.5 Electrochemical Techniques for Redox-MHD Pumping. CA and CP were performed to characterize the PEDOT film and to monitor the electrochemical response over time. For both electrochemical techniques, one set of four band electrodes (shorted together

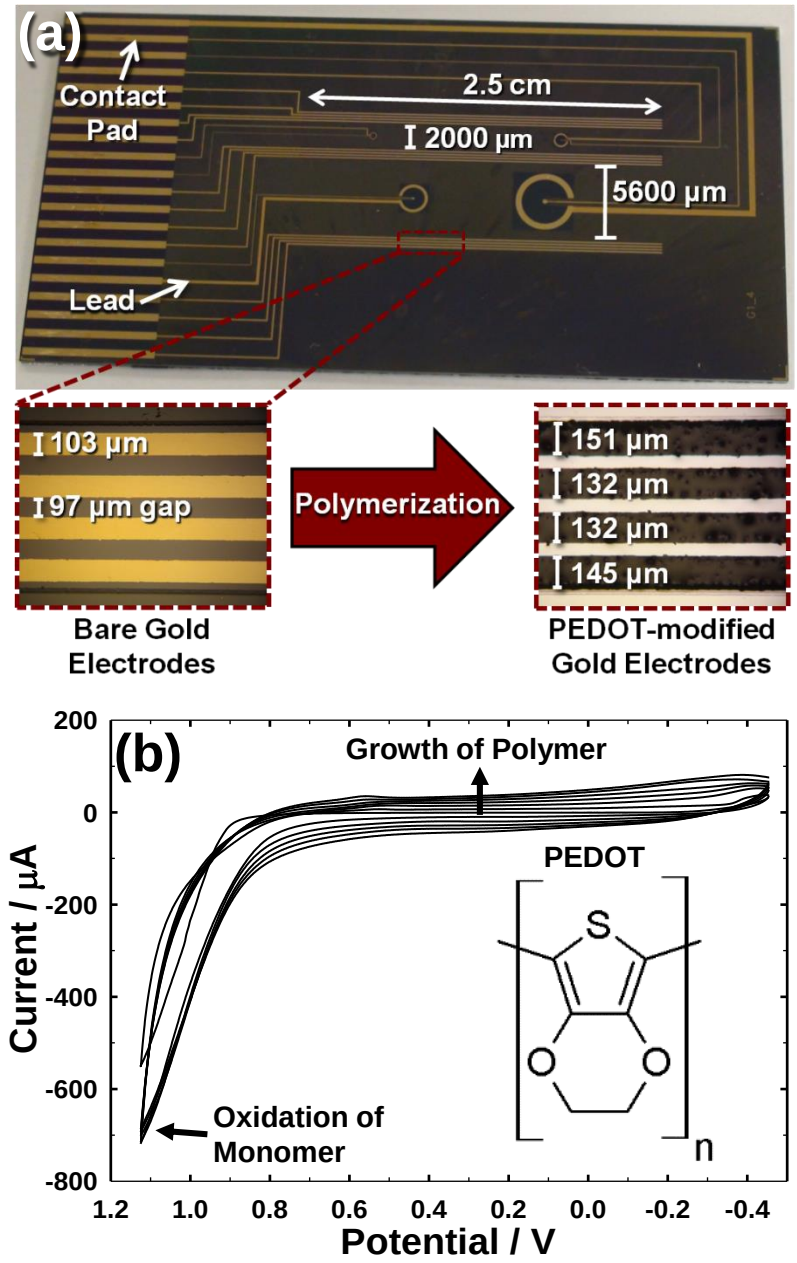

Figure 2.1 (a) Photograph of microelectrode array chip showing electrode features and dimensions. Expanded view photographs show unmodified gold and PEDOT-modified gold band electrodes under a microscope. (b) Cyclic voltammogram during electrodeposition of PEDOT onto the active electrode surfaces. Inset picture of chip shows chemical structure of PEDOT.

using the wires emerging from the edge connector) that were coated with PEDOT served as the working electrode and the two sets (separated by 2000 μm) of four band electrodes modified with PEDOT served as the combined auxiliary and quasi-reference electrodes. The working electrodes were separated from the auxiliary/quasi-reference electrodes by a gap of 5600 μm (Figure 2.2b). For the CA experiment, the potential at the working electrodes was held at 1.0 V for 5 s after a quiet time of 10 s at -0.3 V. The 10 s quiet time was used to regenerate the PEDOT film prior to applying an oxidizing potential step for video microscopy. For the CP experiments, current was chosen based on the desired flow rate. To prevent the PEDOT film from becoming over-oxidized, the current was held until a potential of 1.2 V versus the PEDOT-modified auxiliary/quasi-reference electrodes was reached. Currents specified throughout this study follow the standard convention; negative current indicates that the working electrode serves as the anode and positive current indicates the working electrode serves as the cathode.

2.3.6 Setup for Video Microscopy. To visualize the flow of solution around the PEDOT-modified electrodes, polystyrene microbeads were added to solution and tracked using a microscope interfaced with a Sony Handycam camera (Figure 2.2a). The x- and y-position of the recorded video were adjusted using the microscope stage. The height above the chip surface was adjusted for the video recording by raising and lowering the focus of the microscope objective. The average speed of the beads over a given time were analyzed using particle imaging velocimetry (PIV) analysis with Dynamic Studios.[10] The beads analyzed by PIV were in the solution and within ±75 μm of the microscope's focal plane. The PIV software measures the displacement of the beads in solution to determine the 2D velocity field by breaking the video frames into interrogation regions, and then following bead patterns in subsequent frames. An average velocity vector is generated for each interrogation region. PIV was used to analyze the fluid flow profiles for the applied current experiments.

To find instantaneous bead speed during the applied potential experiments, better time resolution is needed to quantify transient bead velocities, which follow the current response. Particle tracking software (World-In-Motion Physics Toolkit software (WIM, www.physicstoolkit.com)) was used to track the movement of individual beads during the

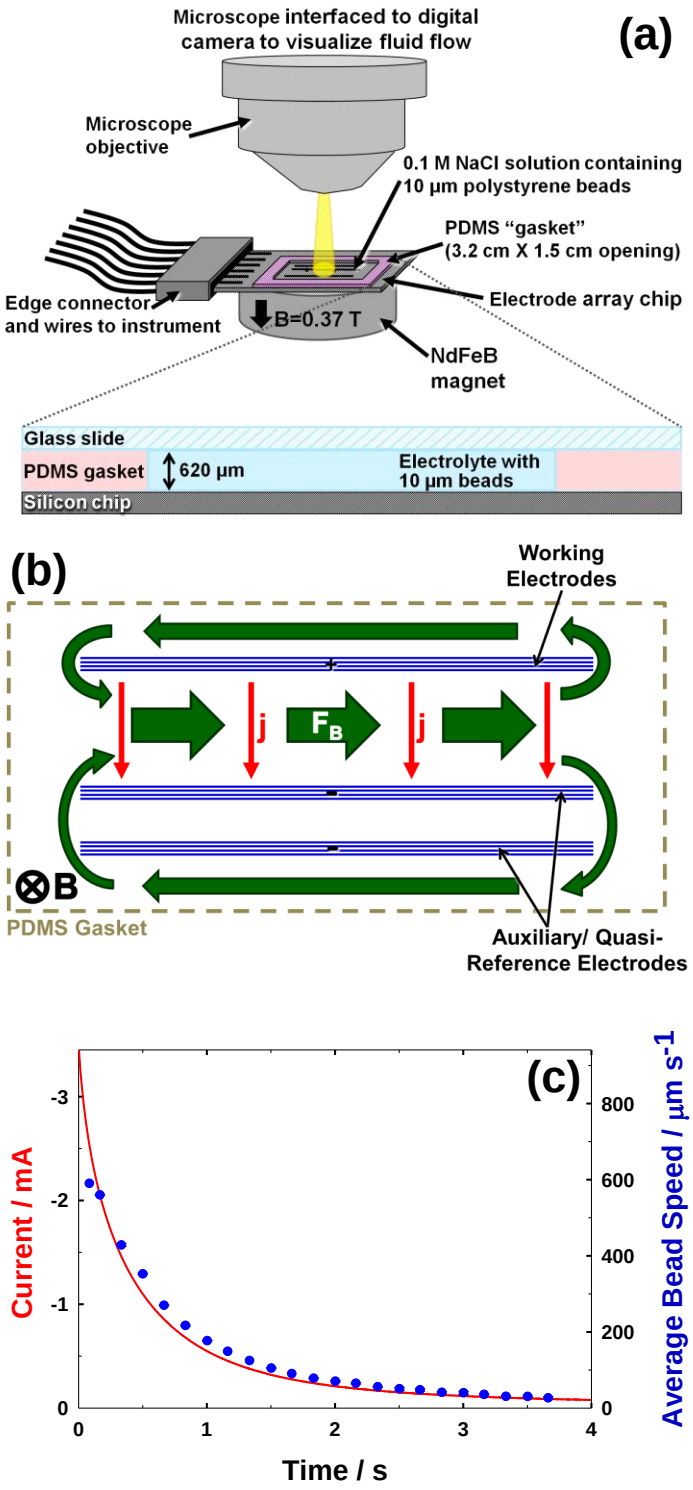

Figure 2.2 (a) Schematic of experimental setup showing method for tracking microbeads in solution. (b) Schematic of electrode configuration during for redox-MHD experiments. The working electrode consists of four PEDOT-modified band electrodes (100 µm X 2.5 cm). Eight band electrodes, separated from the working electrodes by a gap of 5600 µm, serve as auxiliary and quasi-reference. (c) Overlay of current response and averaged instantaneous bead speed over time during an applied potential experiment (+1.00 V) (microscope was focused 300 µm above chip).

experiment. Bead velocity determined using particle tracking software was done by tracking the displacement of four individual beads over a given amount of time as determined by the time stamp on the video. The scale of the video was determined based on the width of the electrodes recorded at the start of every video. The average and standard deviation of the bead speed were calculated by dividing the displacement of the beads by the time as determined by the time stamp on the video.

2.3.7 Characterization of Vertical and Horizontal Flow Profiles. The flow profile in the gap between the inner edges of the sets of working and auxiliary/quasi-reference band electrodes was examined vertically and horizontally. The cell volume examined to determine the vertical flow profile was in the middle of the gap between the working and auxiliary band electrodes and halfway along the length of the electrodes. The vertical flow profile during an applied anodic current of -50.00 μA was examined by initially focusing the microscope on the surface of the chip and shifting the focal plane in the positive z-direction (from the electrode chip to the glass slide) every 5 s until reaching the ceiling of the cell. The flow profiles were examined throughout the cell at 75, 150, 300, 450, and 600 μm above the chip. The average velocity of the beads in focus at each position was averaged for four experiments using the same chip and modified electrodes and pooled standard deviations were calculated.

The horizontal flow profile was also examined during four different applied current (-50 μA) experiments. The microscope was initially focused on the PEDOT-modified electrodes and was gently moved by 1 mm every 5 s across the 5600-μm gap until the auxiliary electrodes came into view. Two of the experiments began with the camera focused on the working electrodes and two experiments focused on the auxiliary electrodes. The PIV software generates columns of velocity vectors across the video screen (see Figure 2.4a). The distance from the working electrode was calculated for each column of velocity vectors and was sorted accordingly. The data for four experiments was organized into bins (to the nearest 0.1 mm) and the average and standard deviation of each bin were calculated. Because the video recorded a location that was 1.53 mm wide at each position and the stage was moved in 1 mm increments across the gap for

each position, areas of overlap exist; these data points were averaged together and the pooled standard deviation was calculated accordingly.

2.4 Results and Discussion

2.4.1 MHD Pumping at PEDOT-Modified Electrodes under Controlled Potential Conditions. As previously mention, MHD force follows changes in the ionic current density; therefore, it is worthwhile to discuss the current response at the electrodes under different situations because it is a predictor of the effect on fluid velocity.[38] When a potential that is sufficiently past the standard electrode potential of the pumping species is applied to electrodes, the current response features an initial spike corresponding to the combination of charging the double layer at the electrode surface and of the faradaic current from redox species at the electrode surface. For solution-based redox chemistry, after the double layer has been charged, the current decreases with a $t^{-1/2}$ falloff due to linear diffusion of redox species to the electrode. At microelectrodes, a pseudo-steady state is eventually reached once radial diffusion of the redox species to the electrode dominates.[6, 39] Fluid flow, which is proportional to the ionic current density, follows the same trend in current with high initial velocities, then drops off over time, and finally reaches a pseudo-steady state. In the work reported in this paper, the redox species were immobilized onto the electrode surface in the form of a conducting polymer PEDOT. Figure 2.S1b demonstrates the current response of bare electrodes in electrolyte and in solution redox species, RuHex, and of PEDOT-modified electrodes in electrolyte. PEDOT-modified electrodes exhibit much higher currents initially, but quickly drop to zero while the bare electrodes in RuHex continues to produce a current limited by mass-transport of fresh redox species arriving at the electrode from the surrounding solution.

In order to see what magnitude of current and maximum fluid speeds these PEDOT-modified electrodes are capable of producing, a potential of +1.00 V was applied. When a potential is applied to the film, electrons are shuttled through the PEDOT film until all of the redox centers have been converted resulting in currents that are initially high (3.5 mA), but decrease quickly over time until it eventually reaches low µA range (Figure 2.2c). The bead velocities achieved in the first seconds of the experiment are initially as high as 600 µm s^{-1}, but cannot be

sustained and quickly drop off to zero with the current (Figure 2.2c). This is a factor of 80 times the velocity observed in past studies with redox-MHD with the same electrode geometries involving 0.095 M $K_3Fe(CN)_6$ and 0.095 M $K_4Fe(CN)_6$ in a solution of 0.1 M KCl as supporting electrolyte, illustrating a major advantage of the PEDOT-modified electrodes. The velocities with the PEDOT are impressive but the short duration may not yet be suitable for microfluidic applications that require longer pumping times or constant flow velocity.

2.4.2 MHD Pumping at PEDOT-Modified Electrodes under Controlled Current Conditions. The fluid flow can be manipulated more precisely by applying a current directly, instead of applying a potential (Figure 2.3a). We have previously demonstrated in systems with the redox species in solution under controlled current conditions, for a fixed electrode geometry, and a given magnetic flux density, $|\mathbf{B}|$, the magnitude of the fluid velocity, $|\mathbf{v}|$, is proportional to the electronic current passing through the electrodes, i(t).[39] This effect is also shown here for MHD generated from PEDOT-modified electrodes. Our studies find that as in the solution redox systems, increasing the applied current increases fluid speed proportionally. A least squares fit to a line yielded a slope of 0.4978 ± 0.0097 $\mu m \cdot s^{-1} \cdot \mu A^{-1}$ and a y-intercept of 2.7979 ± 1.8570 $\mu m \cdot s^{-1}$ with a R^2 value of 0.9985 (Figure 2.3b). This relationship makes it possible to simply fine-tune fluid speeds for a fixed electrode geometry. In these applied current experiments, the potential increased linearly over time. To prevent the PEDOT on the electrodes from over-oxidation, a cut-off potential of 1.2 V was set. The time that a current could be applied before the potential reached 1.2 V varied from 75 s for an applied current of -25 µA to 3.2 s for an applied current of -400 µA. The time decreased with increasing current. Therefore, depending on the needs of the microfluidic application, the velocity and time needed for fluid flow can be adjusted by controlling the magnitude of the applied current, but restricted ultimately to the total coulombic capacity (the product of the current and time) that is available.

2.4.3 Vertical Flow Profile under Controlled Current Conditions. The flow profile between the working and combined auxiliary/quasi-reference microband electrodes was examined vertically and horizontally. The vertical flow profile was

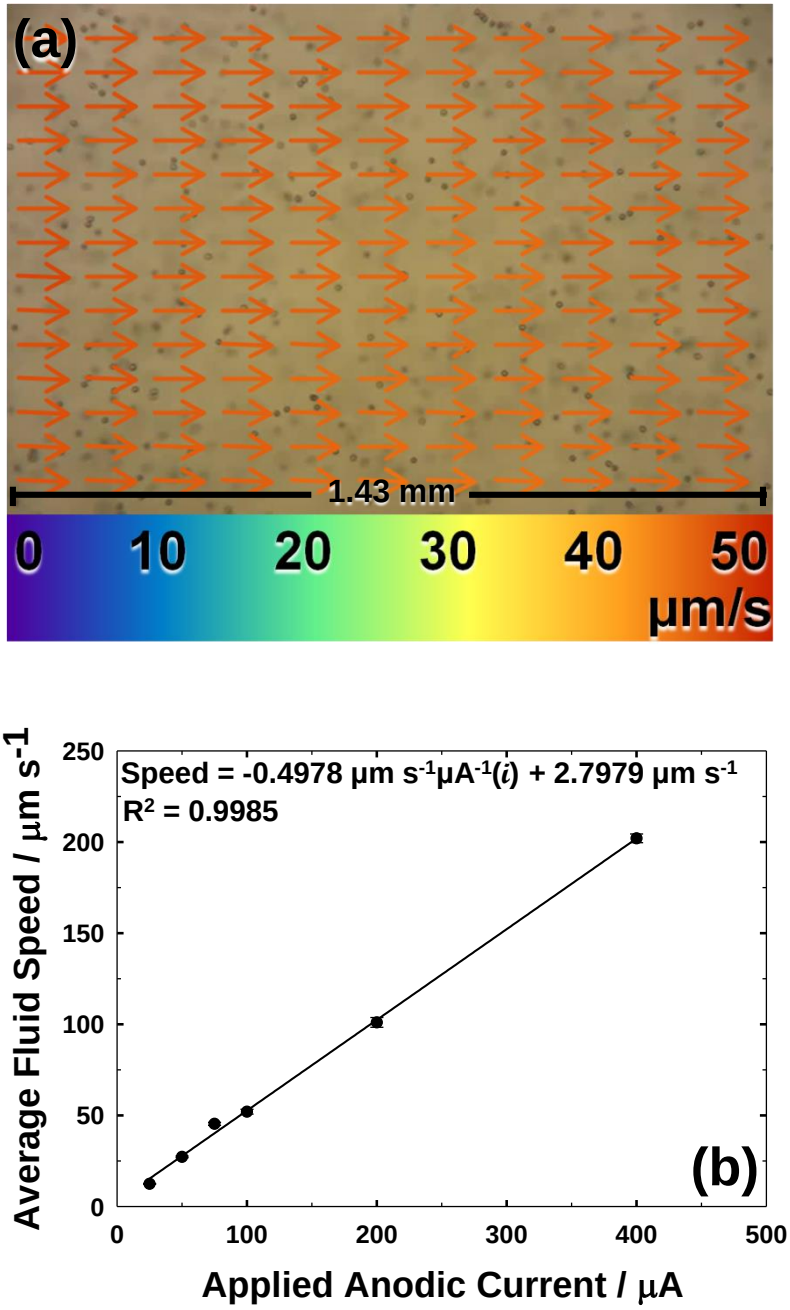

Figure 2.3 (a) PIV analysis during applied current experiment (-75.0000 μA). Video was taken in the middle of the 5600 μm gap between working and auxiliary band electrodes and 300 μm above the chip surface. (b) Plot of average fluid velocities for different applied current experiments. Fluid Velocity = -0.4978 $\mu ms^{-1}\mu A^{-1}$ (current) + 2.7979 μms^{-1}.

examined by measuring the average velocity using PIV at different heights within the cell while applying a current of -50 µA (Figure 2.4a). The vertical flow profile was fit to a parabola with an R^2 value of 0.9926, following the equation:

$$\text{Velocity} = -0.0001\ \mu m^{-1}\ s^{-1}\ (\text{Height})^2 + 0.1165\ s^{-1}\ (\text{Height}) + 0.274\ \mu m\ s^{-1}$$

This indicates that the highest velocity (23 µm s^{-1}) is in the center of the cell (400 µm) while the fluid flow greatly decreases close to the chip and close to the glass slide ceiling where no-slip boundary conditions exist. This result differs from previous results obtained with the same electrode geometry, but with redox species, $Fe(CN)_6^{3-/4-}$ in solution during an applied current of -307 µA.[37] This variance could indicate a difference in vertical ionic current density distribution throughout the height of the cell, or could be due to a combination of differences in solution viscosity and the magnitude of applied current.

2.4.4 Horizontal Flow Profile under Controlled Current Conditions. The horizontal flow profile was also examined during four different applied current (-50 µA) experiments (Figure 4b) and velocity vectors in 0.1 mm sections across the 5600 µm gap were averaged and pooled standard deviations for each section was calculated. Multiple applied current experiments were performed partially due to the restrictions of the current sustainability of PEDOT and to investigate the variability between experiments. At the anode, PEDOT goes from its neutral state to its +1 oxidation state, and this is associated with ions moving into or out of the film from the surrounding solution to compensate for the change in charge. Based on work done by Zoski et al., most likely chlorine ions are migrating into the film to compensate for the change in charge.[40] At the cathode, PEDOT is converted from its +1 oxidation state to its neutral state, causing anions to leave the PEDOT film and go into the surrounding solution. This generates a net movement of anions toward the anode, thus completing the circuit. It is expected that the fluid flow velocity should be proportional to the ionic current density, assuming that the magnetic field is uniform across the gap. The PIV analysis done for each position showed that the horizontal flow profile was indeed flat, demonstrating that the flow profile

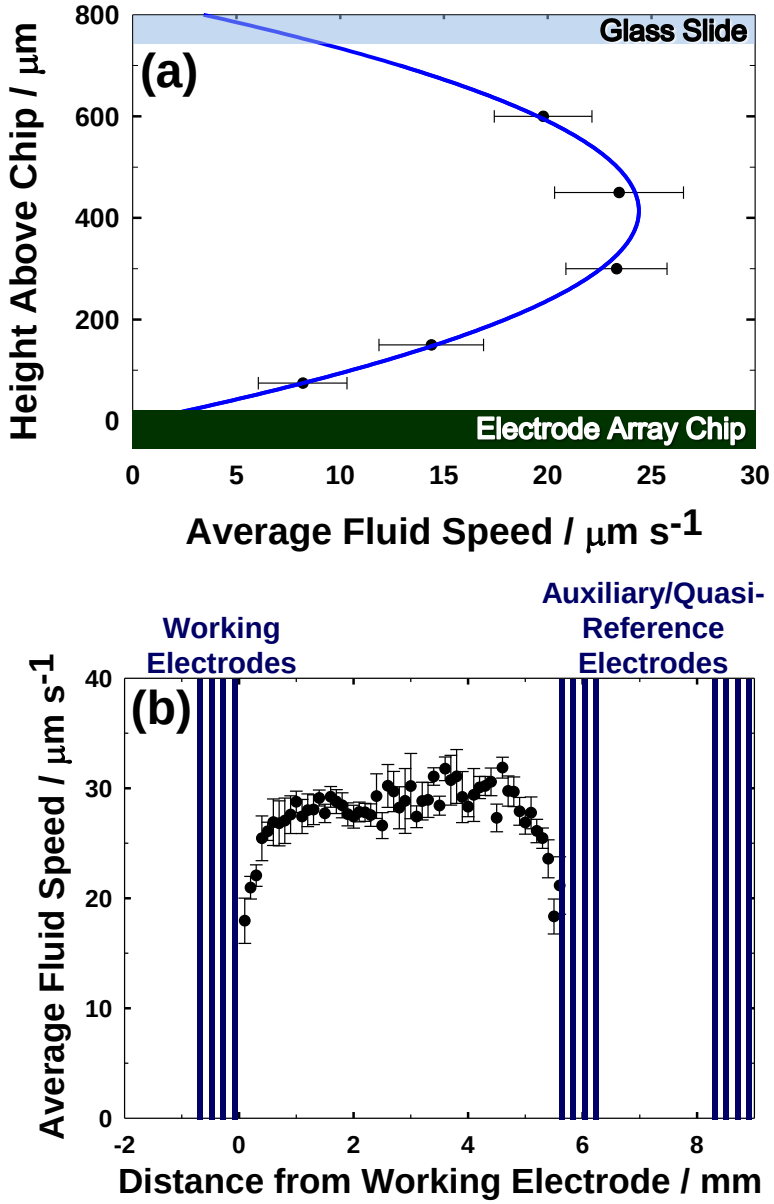

Figure 2.4 (a) Vertical flow profile in the middle of the 5600 μm gap between working and auxiliary band electrodes. Video microscopy was done using approximately 5 seconds of video at each height shown (75, 150, 300, 450, and 600 μm). The vertical flow profile was parabolic in shape and was fitted with an R^2 value of 0.9926 to the equation:

Velocity = -0.0001 $\mu m^{-1} s^{-1}$ $(Height)^2$ + 0.1165 s^{-1} (Height) +0.274 μm s^{-1}

(b) Horizontal flow profile across 5600 μm gap between working and combined auxiliary/quasi-reference band electrodes. Velocity vectors from four applied current experiments were divided into bins at 0.1 mm increments and bins were averaged across the gap.

species with bare electrodes.[37] The average velocity for the middle of the gap where the fluid flow profile was the most flat (from 0.5 mm to 5.1 mm) was 28.7 (± 3.51) µm/s. The flow profile for redox-MHD at the same electrode geometry in the presence of $K_3Fe(CN)_6$ and $K_4Fe(CN)_6$ during an applied current experiment of 120 µA generated a flat profile with velocities of 47.1 ± 1.7 $\mu m \cdot s^{-1}$. The increased variation between fluid velocities across the gap for MHD flow generated at PEDOT-modified electrodes was observed due to the limited time of data collection for each position across the gap. The length of time a potential of -50 µA could be applied was 34 s before the coulombs were exhausted. This meant that order to move across the 5600 µm gap in 1 mm segments during that time, the stage had to be moved every 5 s. Moving the stage causes the solution to slosh, which disturbs the flow profile. PIV analysis was performed 2 s after the stage had been moved to reduce the effects of solution sloshing. PIV analyses done for MHD flow for solution based redox species can wait indefinitely until the solution has stopped moving completely for several seconds.

2.5 Conclusions

In this study, we have demonstrated redox-MHD fluid flow around PEDOT-modified microband electrodes. By eliminating redox species in solution, interferences with detection and with biological components can be easily avoided. The PEDOT films exhibited excellent electrochemical reversibility and longevity (>50 microfluidic pumping experiments) which make PEDOT an outstanding immobilized redox species for MHD applications. In addition, because the PEDOT films were deposited in aqueous solutions, it is possible that enzymes could be copolymerized making biosensing applications possible. Furthermore, redox-MHD fluid flow can be generated using applied potential if a quick burst of fluid flow is needed or using applied current if carefully fine-tuned fluid flow is required for the specific application. The level of control of the fluid flow velocity and the pumping time is attractive for designing systems to meet the requirements of a given microfluidic application, especially those involving biological samples.

2.6 Acknowledgements

Research was supported through the National Science Foundation (NSF) (CHE-0719097 and CBET-1336853) and the Arkansas Biosciences Institute, the major research component of the Arkansas Tobacco Settlement Proceeds Act of 2000.

2.7 Supporting Information

Video clips of microbead movement during redox-MHD experiments at PEDOT-modified electrodes showing flow patterns in the middle of the gap between working and combined auxiliary/quasi-reference microband electrodes during an applied potential and an applied current experiment. This material is available free of charge via the Internet at http://pubs.acs.org.

2.8 References

(1) Whitesides, G. M. *Nature* **2006**, *442*, 368-373.

(2) Nguyen, N.-T.; Huang, X.; Chuan, T. K. *Journal of Fluids Engineering* **2002**, *124*, 384-392.

(3) Weston, M. C.; Gerner, M. D.; Fritsch, I. *Analytical Chemistry* **2010**, *82*, 3411-3418.

(4) Qian, S.; Bau, H. H. *Mechanics Research Communications* **2009**, *36*, 10-21.

(5) Pamme, N. *Lab on a Chip* **2006**, *6*, 24-38.

(6) Anderson, E. C.; Weston, M. C.; Fritsch, I. *Analytical Chemistry* **2010**, *82*, 2643-2651.

(7) Weston, M. C.; Nash, C. K.; Fritsch, I. *Analytical Chemistry* **2010**, *82*, 7068-7072.

(8) Sahore, V.; Fritsch, I. *Microfluidics and Nanofluidics* **2014**, 1-8.

(9) Cheah, L. T.; Fritsch, I.; Haswell, S. J.; Greenman, J. *Biotechnology and Bioengineering* **2012**, *109*, 1827-1834.

(10) Scrape, P. G.; Gerner, M. D.; Weston, M. C.; Fritsch, I. *Journal of The Electrochemical Society* **2013**, *160*, H338-H343.

(11) Wang, X.; Sjoberg-Eerola, P.; Eriksson, J.-E.; Bobacka, J.; Bergelin, M. *Synthetic Metals* **2010**, *160*, 1373-1381.

(12) Poverenov, E.; Li, M.; Bitler, A.; Bendikov, M. *Chemistry of Materials* **2010**, *22*, 4019-4025.

(13) Bobacka, J.; Lewenstam, A.; Ivaska, A. *Journal of Electroanalytical Chemistry* **2000**, *489*, 17-27.

(14) Tamburri, E.; Orlanducci, S.; Toschi, F.; Terranova, M. L.; Passeri, D. *Synthetic Metals* **2009**, *159*, 406-414.

(15) Groenendaal, L.; Jonas, F.; Freitag, D.; Pielartzik, H.; Reynolds, J. R. *Advanced Materials* **2000**, *12*, 481-494.

(16) Kumar, S.; Mathiyarasu, J.; Phani, K.; Yegnaraman, V. *Journal of Solid State Electrochemistry* **2006**, *10*, 905-913.

(17) Xiao, Y.; Li, C. M.; Wang, S.; Shi, J.; Ooi, C. P. *Journal of Biomedical Materials Research Part A* **2009**, *92A*, 766-772.

(18) Cui, X.; Martin, D. C. *Sensors and Actuators B: Chemical* **2003**, *89*, 92-102.

(19) Randriamahazaka, H.; Noel, V.; Chevrot, C. *Journal of Electroanalytical Chemistry* **1999**, *472*, 103-111.

(20) Hass, R.; GarcÃ-a-CaÃ±adas, J.; Garcia-Belmonte, G. *Journal of Electroanalytical Chemistry* **2005**, *577*, 99-105.

(21) Snook, G. A.; Peng, C.; Fray, D. J.; Chen, G. Z. *Electrochemistry communications* **2007**, *9*, 83-88.

(22) Kayinamura, Y. P.; Roberts, J. H.; Rubinson, J. F. *ACS applied materials & interfaces* **2012**, *4*, 1601-1607.

(23) Kayinamura, Y. P.; Ovadia, M.; Zavitz, D.; Rubinson, J. F. *ACS applied materials & interfaces* **2010**, *2*, 2653-2662.

(24) Sakmeche, N.; Aeiyach, S.; Aaron, J.-J.; Jouini, M.; Lacroix, J. C.; Lacaze, P.-C. *Langmuir* **1999**, *15*, 2566-2574.

(25) Sakmeche, N.; Bazzaoui, E. A.; Fall, M.; Aeiyach, S.; Jouini, M.; Lacroix, J. C.; Aaron, J. J.; Lacaze, P. C. *Synthetic Metals* **1997**, *84*, 191-192.

(26) Manisankar, P.; Vedhi, C.; Selvanathan, G.; Gurumallesh Prabu, H. *Journal of Applied Polymer Science* **2007**, *104*, 3285-3291.

(27) Rozlosnik, N. *Analytical and bioanalytical chemistry* **2009**, *395*, 637-645.

(28) Green, R. A.; Lovell, N. H.; Wallace, G. G.; Poole-Warren, L. A. *Biomaterials* **2008**, *29*, 3393-3399.

(29) Ludwig, K. A.; Uram, J. D.; Yang, J.; Martin, D. C.; Kipke, D. R. *Journal of neural engineering* **2006**, *3*, 59.

(30) Bello, A.; Giannetto, M.; Mori, G.; Seeber, R.; Terzi, F.; Zanardi, C. *Sensors and Actuators B: Chemical* **2007**, *121*, 430-435.

(31) Colleran, J. J.; Breslin, C. B. *Journal of Electroanalytical Chemistry* **2012**, *667*, 30-37.

(32) Xiao, Y. H.; Li, C. M.; Toh, M. L.; Xue, R. *Journal of applied electrochemistry* **2008**, *38*, 1735-1741.

(33) Vedrine, C.; Fabiano, S.; Tran-Minh, C. *Talanta* **2003**, *59*, 535-544.

(34) Fabiano, S.; Tran-Minh, C.; Piro, B. Ì. t.; Dang, L. A.; Pham, M. C.; Vittori, O. *Materials Science and Engineering: C* **2002**, *21*, 61-67.

(35) Istamboulie, G.; Sikora, T.; Jubete, E.; Ochoteco, E.; Marty, J.-L.; Noguer, T. *Talanta*, *82*, 957-961.

(36) Piro, B. Ì. t.; Dang, L. A.; Pham, M. C.; Fabiano, S.; Tran-Minh, C. *Journal of Electroanalytical Chemistry* **2001**, *512*, 101-109.

(37) Sahore, V.; Fritsch, I. *Analytical Chemistry* **2013**.

(38) Weston, M. C.; Fritsch, I. *Sensors and Actuators B: Chemical* **2012**, *173*, 935-944.

(39) Weston, M. C.; Nash, C. K.; Homesley, J. J.; Fritsch, I. *Analytical Chemistry* **2012**, *84*, 9402-9409.

(40) Yang, N.; Zoski, C. G. *Langmuir* **2006**, *22*, 10338-10347.

2.S Supporting Information: Poly(3,4-ethylenedioxythiophene)-Modified Electrodes for Magnetohydrodynamic (MHD) Microfluidics

Supporting Information contains **v**ideo clips of microbead movement during redox-MHD experiments at PEDOT-modified electrodes. Files are available showing flow patterns in the middle of the gap between working and counter/quasi-reference electrodes during an applied potential (2S_001.mpg) and an applied current experiment (2S_002.mpg). Supporting information also includes the characterization of the microband electrodes before and after electrodeposition of PEDOT in 0.1 M NaCl and in 5 mM $Ru(NH_3)_6^{2+/3+}$ in 0.1 M NaCl. The current response of PEDOT-modified electrodes during a chronoamperometry experiment was modeled at different times during the experiment.

2.S1 Captions to Video Clips

2S _001.mpg Video of microbead movement between working and counter/quasi-reference electrodes during an applied potential experiment. A 620 µm thick PDMS gasket was placed on the chip and filled with 325 µL of a solution containing 0.095 M NaCl and polystyrene beads. A NdBFe magnet was used to generate a magnetic field of 0.37 T. A potential of +1.0 V vs. the PEDOT-modified gold quasi-reference was applied to the PEDOT-modified microband electrodes. For this video, the microscope was focused 300 µm above the chip surface.

2S_002.mpg Video of microbead movement between working and counter/quasi-reference electrodes during an applied current experiment. An applied current of -50 µA was applied to the PEDOT-modified microband electrodes until the cutoff potential of +1.2 V was reached. All other experimental parameters are the same as described in the caption for **2S_001.mpg .**

2.S2 Characterization of Microband Electrodes Before and After PEDOT-Deposition via CV. CV of bare microband electrodes in 0.100 M NaCl at different scan rates were performed and the charging current vs. scan rate was plotted to find the double layer capacitance. The scan rate study revealed a double layer capacitance, C_{dl}, of 44.66 $\mu F \cdot cm^{-2}$. CV of bare microband electrodes in $Ru(NH_3)_6^{2+}$ at 0.05 $V \cdot s^{-1}$ generated a peak of -62.02 µA and $Ru(NH_3)_6^{3+}$ a peak of 59.82 µA with a peak splitting of 0.149 V (see Figure 2.S1a).

The PEDOT-modified microband electrodes were also electrochemically characterized using CV in a solution of 0.100 M NaCl and a solution of 2.5 mM $Ru(NH_3)_6^{2+}$, $Ru(NH_3)_6^{3+}$, and 0.100 M NaCl . The cyclic voltammogram in electrolyte alone had broad oxidation-reduction peaks of ±50 µA. The broadness of the peaks occurs because these films are composed of multiple redox sites with different levels of accessibility to ions coming in to compensate for the change in charge, it is probable that a distribution of oxidation-reduction potentials exist.[41] The cyclic voltammogram also exhibits capacitive behavior due to the large surface area to volume ratio of PEDOT. PEDOT modified electrodes were also characterized in a solution containing $Ru(NH_3)_6^{2+/3+}$. This cyclic voltammogram shows the $Ru(NH_3)_6$ peaks riding on top of the current response generated by the PEDOT film on the electrode surface. $Ru(NH_3)_6^{2+}$ generated a peak of -65.70 µA and $Ru(NH_3)_6^{3+}$ a peak of 75.90 µA with a peak splitting of 0.210 V. Using the ratio of peaks at the cathode and assuming that the diffusion coefficient of $Ru(NH_3)_6^{3+}$ remains the same, it is estimated that the area increased by 16% due to the rough topology of the PEDOT film. In addition to the increase in current that is achievable by modifying these electrodes with PEDOT, more extreme oxidizing potentials could be applied without oxidizing the gold electrodes. Successive cyclic voltammograms of PEDOT-modified electrodes were similar indicating electrochemical reversibility and film stability.

2.S3 Characterization of Microband Electrodes Before and After PEDOT-Deposition via CA. Prior to electrodeposition of PEDOT, the gold microband electrodes were characterized via CA in pure electrolyte alone (0.100 M NaCl) to assess charging current and in a solution of 5.00 mM $Ru(NH_3)_6^{2+/3+}$ (total concentration with a 1:1 ratio of oxidation states) and 0.100 M NaCl to provide a comparison for PEDOT-modified electrodes of a redox species contained in solution

(see Figure 2.S1b). A 5.00 mM concentration of $Ru(NH_3)_6^{3+}$ has been shown to be compatible with viable heart tissue[9] and with alkaline phosphatase, a common immunoassay component.[7] To get a sense of the charging current and resistance of the bare Au microband electrodes, CA in 0.100 M NaCl was performed. At an applied potential of +0.400 V, a maximum current of 373.0 µA was measured. The current response over time was fit to the equation:

$$i_c(t) = \frac{E}{R_u} e^{(-t/R_u C)}$$

where i_c is the charging current over time (A), E is the potential applied (V), R_u is the uncompensated resistance (Ω), and C is the capacitance (F). The R^2 value for this fit was 0.974. R_u was determined to be 506 Ω and C was 1.51 F. The RC-time constant, τ, was 2.000 ms.

Bare microband electrodes were also characterized in 2.5 mM $Ru(NH_3)_6^{2+}$ and 2.5 mM $Ru(NH_3)_6^{3+}$ in 0.100 M NaCl. The maximum current was measured at -766.90 µA and the pseudo-steady state current was -14.610 µA.

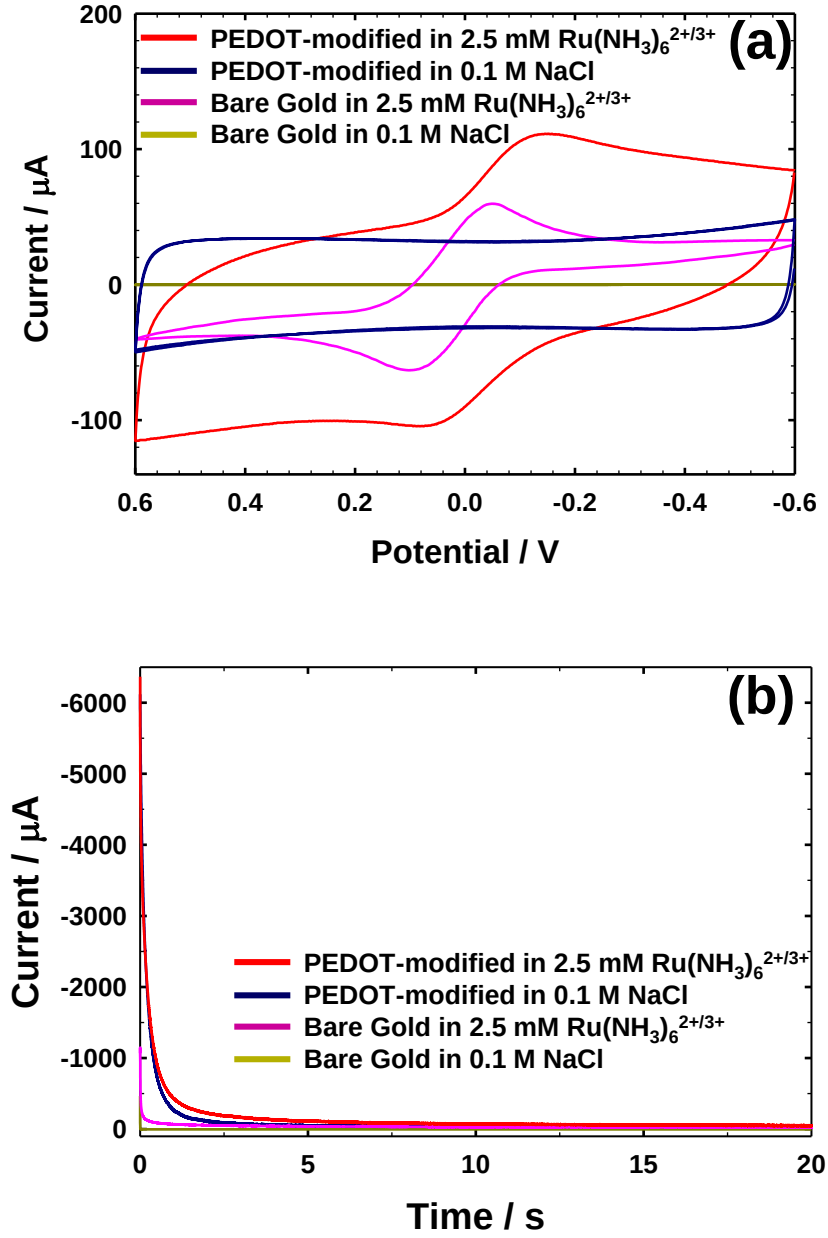

Figure 2.S1 (a) Cyclic voltammogram of bare gold electrodes in 0.100 M NaCl (gold), bare gold electrodes in 5.00 mM $Ru(NH_3)_6^{3+/2+}$ in 0.100 M NaCl (purple), and PEDOT-modified electrodes in 0.100 M NaCl (blue). (b) CA of bare gold electrodes in 0.100 M NaCl (gold), bare gold electrodes in 5.00 mM $Ru(NH_3)_6^{3+/2+}$ in 0.100 M NaCl (purple), and PEDOT-modified electrodes in 0.100 M NaCl (blue).

2.S4 Modeling Current Response of PEDOT during Chronoamperometry. The chronoamperometric results obtained with PEDOT-modified gold microband electrodes in 0.1 M NaCl agree well with results observed by She and Wang in 2005.[42] The chronoamperometric response can be divided depending on the time into three sections, corresponding to double layer charging ($t < 0.3$ ms), semi-infinite diffusion (1.5 ms $< t <$ 3 ms), and exhausted finite diffusion ($t >$ 3 s). When time is less than 0.3 ms, the double layer is charged and the equivalent circuit can be simplified to C_{dl} and R_Ω in series. When the –ln(current) is plotted versus time, the slope represents $1/R_\Omega C_{dl}$. Once double layer charging is complete, but when $Dt/d^2 << 0.12$, which for this film corresponds to times between 1.5 ms and 3 ms. During this time period, the diffusion process is controlled by semi-infinite diffusion where the Cl^- ions diffuse into the film during the charging process. Therefore, the slope of current versus $t^{-1/2}$ is equal to $\frac{nFAD^{1/2}c}{\pi^{1/2}(1+\lambda)}$, resembling the Cottrell equation, where D is the diffusion coefficient, c is the concentration of electrolyte, d is the film thickness, and λ is the initial potential, $\lambda=\exp(\frac{-nF\Delta E}{RT})$. The equivalent circuit becomes R_Ω and T in series. When $Dt/d^2 >> 0.12$ (when $t > 3$), the exhausted finite diffusion process can be observed where the chargeable sites are exhausted and thin-layer behavior transpires. The equivalent circuit can be modeled as R_Ω, R_L, and C_L in series. Plotting –ln(current) versus time gives a straight line with a slope representing $1/(R_\Omega+R_L)C_L$.

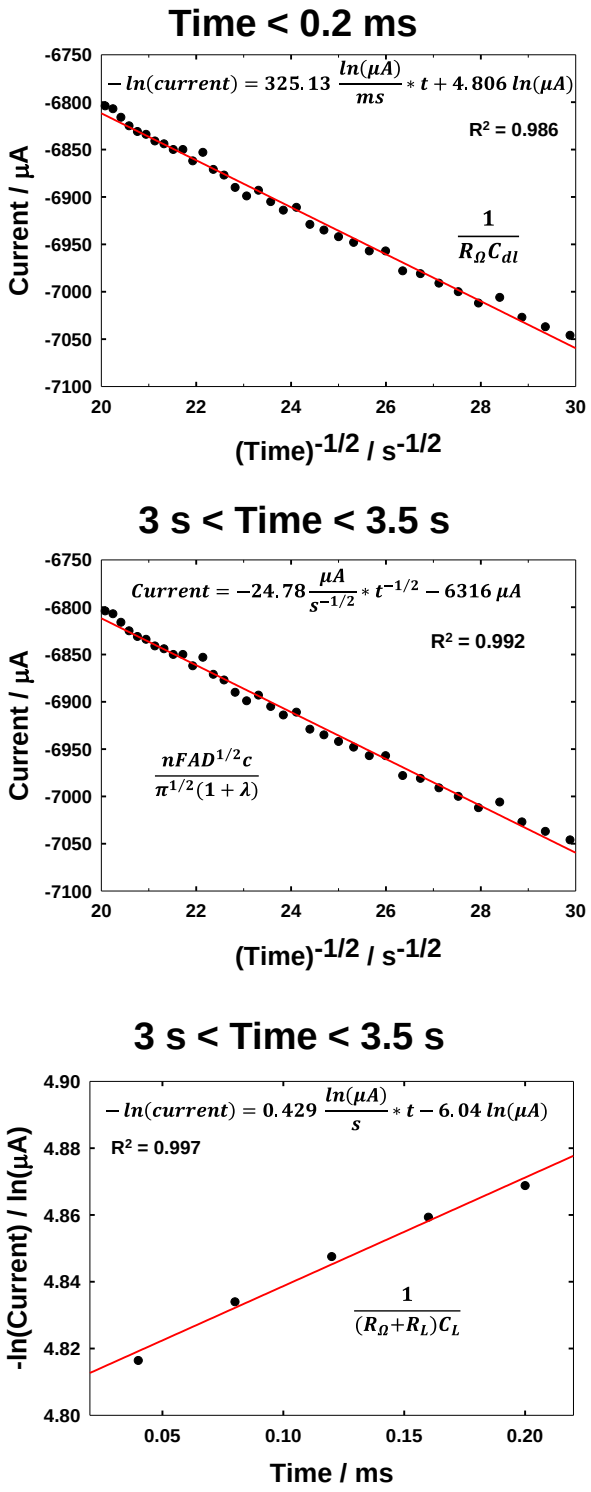

Figure 2.S2 The chronoamperometric response of PEDOT-modified microband electrodes was modeled during three periods of time during the applied current experiment corresponding to double layer charging (t < 0.3 ms), semi-infinite diffusion (1.5 ms < t < 3 ms), and exhausted finite diffusion (t > 3 s).

2.S5 References

(1) Audebert, P.; Miomandre, F. *Handbook of conducting polymers* **2007**, *3*.

(2) Cheah, L. T.; Fritsch, I.; Haswell, S. J.; Greenman, J. *Biotechnology and Bioengineering* **2012**, *109*, 1827-1834.

(3) Weston, M. C.; Nash, C. K.; Fritsch, I. *Analytical Chemistry* **2010**, *82*, 7068-7072.

(4) Ping-Ping, S.; Zheng-Hao, W. *Chinese Journal of Chemistry* **2005**, *23*, 806-810.

3. Redox-Magnetohydrodynamic (MHD) Microfluidics at Poly(3,4-ethylenedioxythiophene)-Modified Concentric Disk and Ring Electrodes

3.1 Abstact

Rotational redox-magnetohydrodynamic (redox-MHD) flow was generated between concentric gold microdisk (160 µm diameter) and ring electrodes (800 µm inner radius and 1000 µm outer radius) modified with the conducting polymer, poly(3,4-ethylenedioxythiophene), PEDOT. The PEDOT-modified electrodes were used to generate the ionic current needed for pumping in the presence of a magnetic field, instead of adding redox species in solution as previously reported, thereby avoiding interferences and producing higher fluid speeds, but with a tradeoff of shorter duration. PDMS gaskets of two thicknesses (750 µm and 1050 µm) were placed on top of the silicon chip that contained the electrodes to define different cell volumes and heights. Fluid flow was monitored via video microscopy of 10 µm polystyrene latex beads in 0.100 M NaCl. The movement of beads was quantified with particle image velocimetry (PIV) analysis. It was observed that the fluid flow was strongest close to the electrodes (300 µm above the chip) where the ionic current density is the highest regardless of cell height. The speeds generated between the disk and ring electrodes are proportional to both the current applied and the magnetic flux density. The speed decreases with increasing radial distance from the disk electrode due to the proportionally increasing cross sectional area, which could be useful for microfluidic mixing applications.

3.2 Introduction

Driven by the need to lower cost by decreasing the required amount of sample and reagents, as well as by increasing throughput and portability, miniaturization has been the dominating trend in analytical techniques over the last two decades.[1] Lab-on-a-chip (LOAC) applications seek to take all of the processes done in a full-size analytical lab, including sample preparation and transfer, reagent mixing, separation and purification of products, and detection of analyte, and scale them down to be performed in a single hand-held device.[2, 3] Of these processes, microfluidic mixing is perhaps the most difficult to achieve. Mixing is typically a crucial aspect of microfluidic devices used in drug delivery, chemical reactions, and biochemistry analysis.[4, 5] In a variety of microfluidic systems, low Reynolds numbers are observed (<1), meaning that the flows are considered laminar and mixing is often difficult and relies on diffusion for mixing, which is inherently slow.[3, 6] Using a redox-MHD approach at PEDOT-modified concentric ring-disk electrodes, microfluidic mixing can be achieved simply by turning on electrodes in the presence of a permanent magnet.

In general, micromixers can be classified into two broad categories: passive mixers and active mixers.[3, 5-8] Passive mixers do not require external energy, relying on diffusion and chaotic advection through the manipulation of laminar flows in microchannels to improve mixing.[5] In passive mixers, specific microchannel configurations are designed to increase the contact area between the mixing species so that they are folded multiple times as they travel down the channel. The complex design of microchannels can increase fabrication costs; therefore, there seems to be a shift in micromixer design toward active chaotic mixers.[6] Active mixers apply an external force to the fluid flows to expedite the diffusion process. Such external forces include pressure disturbance, thermal, acoustics, electrohydrodynamics, electrokinetics, dielectrophoretics, and magnetohydrodynamics (MHD).[3-8] Thermal and acoustic mixing can only be used for applications involving samples that are not sensitive to higher temperatures such as many biological fluids.[5] The latter five techniques require high voltages, which can cause bubble generation in aqueous solutions and the corrosion of electrodes.

MHD microfluidic devices take advantage of the body force, $\mathbf{F_B}$ ($N \cdot m^{-3}$), that occurs when a charged species (ion or electron) moves with a velocity ($m \cdot s^{-1}$) with a component perpendicular to the magnetic flux density, **B** (T). If there is a net movement of ions through a cross sectional area in a cell, it can be described as an ionic current density, **j** ($C \cdot m^{-2}$), where the sign convention is positive for positive ions.[9] The MHD force, then, is governed by the right hand rule where $\mathbf{F_B}$ is perpendicular to both the ionic current density as well as the magnetic field according to the equation:

$$\mathbf{F_B} = \mathbf{j} \times \mathbf{B} \quad (1)$$

MHD offers the advantages of bidirectional pumping, pumping in a loop without channels or valves, and compatibility with aqueous and nonaqueous solutions.[10-14]

MHD has been used in the past to achieve microfluidic mixing. Bau et al. have used low temperature, co-fired ceramic tapes to construct annular MHD devices for circular pumping but required high operating voltages (2 V) which resulted in the degradation of the electrodes over time.[15] They also reported an active micromixer using MHD-convection in an electrolyte solution. The micromixer was inspired by Hassan Aref's design of an inviscid blinking vortex pair for chaotic advection.[16] The stirrer consisted of a circular cavity with an electrode (C) made of a metal washer (7.8 mm radius and 2 mm height) around the circumference and two electrodes (A and B) made from copper wire (0.35 mm radius) positioned on the bottom halfway between the center of the cavity and the inner radius of the metal washer on opposite sides. A uniform magnetic field parallel to the axis of the cylinder was applied to the cavity. Fluid movement was induced by applying a potential bias between the circular electrode and one of the electrodes on the bottom of the cavity, thus creating circular flow centered around the active electrode. The device switches the potential bias between electrode pairs AC and BC periodically to induce mixing. Passive tracers added to the solution to examine the flow field indicated that successful mixing was achieved within several seconds.[17] West et al. designed and fabricated an annular MHD device for enhanced mixing consisting of concentric brass disk (radius of 4 mm) and ring (inner radius of 6 mm) electrodes, both 500 µm thick, creating a 2 mm wide, 500-µm high channel

which was filled with aqueous KCl solution.[18-20] Because only solutions containing supporting electrolyte were used, high voltages were applied to generated sufficient ionic current density for pumping, which can lead to bubble generation from water electrolysis and to electrode degradation. To avoid these problems, some investigators used an approach where an AC power source was connected to the device and to an electromagnet, generating synchronized sinusoidal electric and magnetic fields using high frequencies (>1 kHz).[21-23] The rapid reversal of the electrochemistry at the electrodes avoided electrode degradation and electrolytic bubble generation. Mixing was achieved on the order of 10s of seconds depending on the fluid velocity within the device.

However, the use of electromagnets complicates experimental design when compared to the simplicity of permanent magnets. In recent years, significant improvements in MHD microfluidics have been achieved via the addition of redox species to the pumping solution, allowing for high currents at low applied voltages, avoiding bubbles and electrode corrosion.[24-28] Low concentrations of redox-species (5 mM $Ru(NH_3)_6^{2+/3+}$) have been shown to be compatible with a biological species, alkaline phosphatase (an enzyme commonly used in immunoassay applications), and have been used while performing on-chip detection of an enzymatically-generated substrate, *p*-aminophenol.[26] This low concentration of $Ru(NH_3)_6^{2+/3+}$ has been shown to be compatible with heart tissue, as well.[29] At higher concentrations, which would produce higher currents and therefore higher achievable speeds, the addition of redox species to sample solutions can interfere with analytical detection and the activity of biological species. To minimize the interaction between the redox species and the sample, redox species can be immobilized to the electrode surface. In the work described below, poly(3,4-ethylenedioxythiophene), PEDOT, which has been electrochemically deposited onto the electrode surface, generates the ionic current needed for convection.

In studies by other investigators on the materials properties and behavior of PEDOT-modified electrode it has been shown that the polymer remains electroactive with a wide range of electrolytes and buffers (e.g. NaCl, KCl, $LiClO_4$, phosphate buffer, tetrabutylammonium perchlorate, acetate buffer)[30-36] and with more complex matrices (e.g. human blood, human urine,

and the motor cortex of rats).[37-39] Thus, it is expected that PEDOT-modified MHD should be possible in a broad range of solutions to accommodate the needs of the sample, rather than the needs of the pumping species. In a previous study at oppositely biased long microband electrodes, PEDOT-modified electrodes were shown to be an effective replacement in MHD microfluidics for adding redox species to solution. Moreover, PEDOT-modified electrodes can produce higher currents and therefore higher achievable fluid speeds than solution-based redox species at similar geometries. There is a tradeoff, however; because there are a finite number of coulombs available, unlike in the mass transport limited case when there is a larger reservoir of redox species added to the solution. When a potential is applied, electrons are shuttled through the PEDOT film until all of the redox centers have been converted resulting in currents that are initially high (0.6 $mA \cdot cm^{-2}$) yielding fluid speeds as high as 600 $\mu m\ s^{-1}$, but cannot be sustained, quickly dropping to zero with the current. The current and fluid speeds that are possible with PEDOT-modified electrodes are a factor of 80 times the speeds obtained with redox species in solution for similar electrode and cell geometries and dimensions.

The use of PEDOT-modified ring-disk electrodes were investigated because of their value for on-chip mixing. Due to the variation in ionic current density between the disk and ring electrodes, the fluid flow is fast close to the disk electrodes and slower at the ring electrode, creating a spiraling fluid flow which is of interest for microfluidic mixing. Previously in our group, we have demonstrated circular redox-MHD flows using solution-based redox species at the same ring-disk electrode geometry.[40] In these studies, the ionic current density was generated via the electrochemistry of 0.095 M $K_3Fe(CN)_6$ and 0.095 M $K_4Fe(CN)_6$ in a supporting electrolyte solution of 0.1 M KCl. The fluid flow demonstrated was localized to the cylinder of solution directly above the ring electrode without the presence of side walls. Also, the fluid flow decreased with radial distance from the disk electrode, creating a spiraling flow that was used to enhance the interactions between two separate fluids within the cylinder of fluid above the ring. Fluid speeds up to 14 $\mu m \cdot s^{-1}$ were observed. PEDOT-modified electrodes are capable of higher currents, and therefore higher velocities than solution based redox species and have minimal threat of interfering with the sample or detection. This paper not only demonstrates redox-MHD

without redox species in solution, but also addresses the impact of different currents, cell heights, and magnetic fields with the new PEDOT-modified approach that was not investigated even with the redox species in the solution previously.

In the work described here, laminar rotational flow was observed around PEDOT-modified concentric disk and ring microelectrodes in the presence of a magnetic field from a permanent magnet using redox-MHD. The fluid flow throughout the height of the cell was examined as the magnitude of applied current and the magnitude of the magnetic field was changed. Two different cell heights created by two PDMS gaskets of different thicknesses were used.

3.3 Experimental Section

3.3.1 Chemicals and Materials. Aqueous solutions were made with reagent grade, 18 megohm, deionized water from Ricca Chemical Company (Arlington, TX). All other chemicals were reagent grade and used without further purification unless otherwise specified. The monomer of PEDOT, 3,4-ethylenedioxythiophene, was obtained from Sigma-Aldrich (St. Louis, MO). Sodium chloride was obtained from EMD Chemicals Inc. (Gibbstown, NJ). Potassium chloride was bought from VWR International LLC (West Chester, PA). Sodium dodecyl sulfate was purchased from AMRESCO (Solon, OH). Polystyrene latex microspheres, 10.0 micron diameter (2.5 wt% dispersion in water) and ruthenium (II) hexaammine chloride for characterizing the bare gold electrodes before modification were purchased from Alfa Aesar (Ward Hill, MA). The as-received ruthenium (II) hexaammine chloride also contained the oxidized form, resulting in near 1:1 mixture of each species. The silicon wafers (125-mm diameter and 600-650-µm thick with 2 µm of thermally grown SiO_2 on the surface) used as substrate materials on which electrode arrays were fabricated were purchased from Silicon Quest International (Santa Clara, CA). A chromium-plated tungsten rod (Kurt J. Lesker Company, Clairton, PA) and a gold coin (Canadian Maple Leaf, 99.99%) were used for metal deposition onto the silicon wafers. Benzocyclobutene, BCB, (Cyclotene 4024-40) purchased from Dow Corning Company (Midland, MI) was used to insulate the electrode leads. The edge connector (solder contact, 20/40 position, 0.05 in. pitch)

was purchased from Sullins Electronics Corp. (San Marcos, CA). A poly(dimethyl siloxane), PDMS, gasket was fabricated using OS-30 solvent to clean casting substrate, Sylgard 184 silicon elastomer base, Sylgard 184 silicon elastomer curing agent (Ellsworth Adhesives, Milwaukee, WI). Pre-cleaned microscope glass slides (1.5 × 1.0 × 0.1 $in.^3$) were obtained from VWR.

3.3.2 Microelectrode Chips and Electrochemical Control. Previously published work describe details of the fabrication process of the microelectrode chips (1 in. x 2 in.).[24] The design on the chip includes 12 microband electrodes which are in three sets of four (each electrode is 100 µm wide and 2.5 cm long with a 100 µm gap between electrodes in the set) and four sets of concentric ring and disk electrodes varying in size (Figure 3.1a). Only the set with the disk having a radius 80.03 µm and the ring having an inner radius of 800.25 µm and outer radius of 10003.95 µm was used in this study because the majority of the area within the ring electrode could be visualized under the microscope with the selected magnification. The ring electrode had a 280 µm opening for the lead to the disk electrode (Figure 3.1b). This gives both electrodes the ability to be addressed individually. A CHI 760B bipotentiostat (CH Instruments, Austin, TX) was used to perform cyclic voltammetry (CV), chronoamperometry (CA), and chronopotentiometry (CP).

3.3.3 Characterization of Concentric Ring-disk Electrodes Before PEDOT Electrodeposition. Before characterization and deposition, the bare chip was cleaned in an O2 plasma cleaner for 15 min. The ring-disk electrodes were characterized in electrolyte alone (0.100 M NaCl) and in 5 mM total concentration of Ru(NH3)62+/3+ (2.5 mM of each form) in 0.100 M NaCl. Ru(NH3)62+/3+ was used because it is an ideal redoxspecies and has been used in previous studies to generate MHD fluid flow at low concentrations.26 CV and CA were used to examine the charging current and active electrode area. During the CV experiments, the potential was cycled between -0.6 V and +0.6 V versus a gold pseudo-reference at 0.05 V s-1. For the CA experiments, the potential was stepped from 0 V to +0.3 V for 20 s.

3.3.4 Preparation and Characterization of PEDOT-Modified Ring-disk Microelectrodes. A solution containing 0.010 M of monomer 3,4-ethylene dioxythiophene (EDOT), 0.010 M sodium dodecyl sulfate (SDS), and 0.100 M KCl was prepared and sonicated for 1.5 hr until all of the monomer was dissolved. The chip was submerged in the solution and PEDOT was

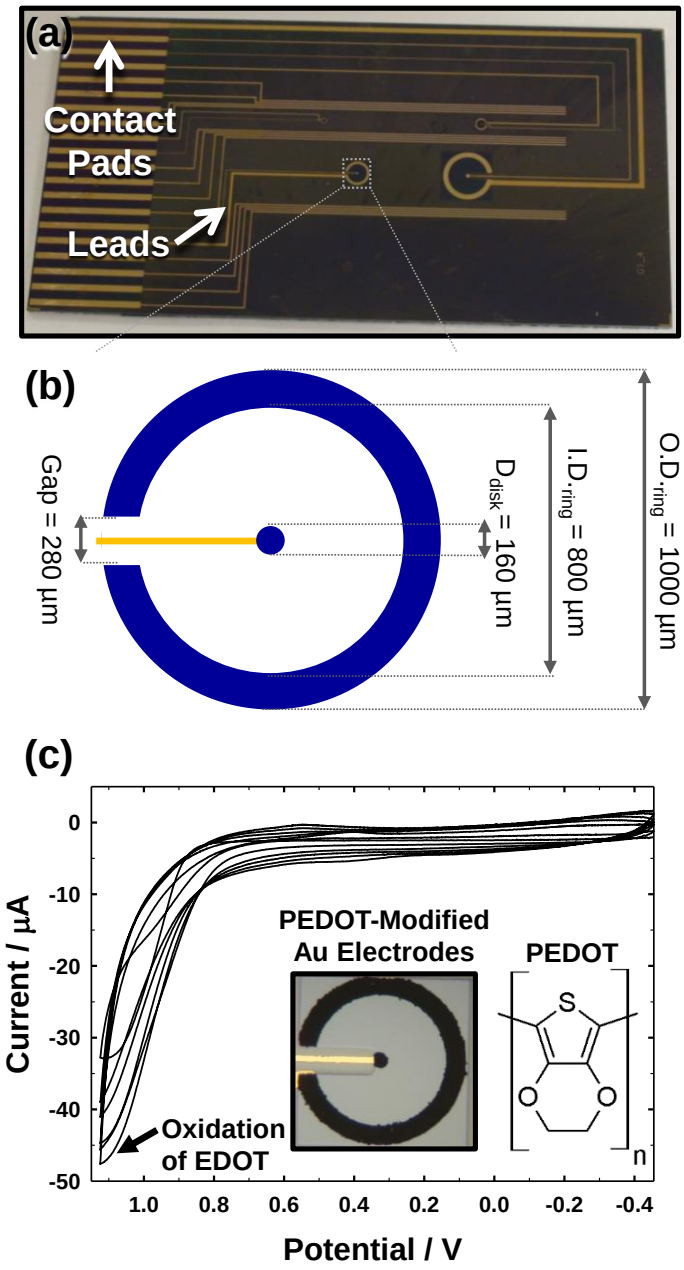

Figure 3.1 (a) Photograph of unmodified electrode array chip used in the studies. (b) Top-down view of concentric ring-disk electrode design with nominal electrode dimensions. All of the experiments performed in this paper used this set of electrodes. (c) Cyclic voltammetry of PEDOT electrodeposition onto concentric ring-disk electrodes, where the disk served as the working electrode and the ring served as the combined auxiliary/quasi-reference electrode. This figure shows current recorded for each cycle and exhibits features representing the oxidation of monomer and the growth of PEDOT onto the electrodes. Insets: a photograph of the PEDOT-modified ring-disk microelectrodes and the chemical structure of PEDOT.

electrodeposited onto active electrode areas by cycling the electrodes from -0.455 V to +1.125 V versus a Ag/AgCl (in saturated KCl) reference electrode at 0.005 V s-1 for 6 cycles. A platinum flag electrode served as the auxiliary electrode during electrodeposition. A dark blue film of PEDOT covered the entire active areas of the electrodes (Figure 3.1c). PEDOT-modified disk electrode was characterized in 0.100 M NaCl via CV and CA using a two-electrode configuration where the PEDOT-modified microring electrode served as combined auxiliary and quasi-reference electrodes (Figure 3.2). During the CV experiments, PEDOT-modified disk electrode was cycled between -1.00 V and +1.00 V at 0.05 V s-1 (Figure 3S.1) and during the CA experiments, the potential was stepped from -0.300 V to +1.00 V for 20 s after a quiet time of 10 s.

3.3.5 Experimental Setup. For the MHD studies, the microfluidic cell was formed by placing a PDMS gasket (with an opening of 1.5 cm × 3.0 cm) on the chip surface to serve as the cell walls (Figure 3.3a). The walls of the gasket were over 0.5 cm away from the ring-disk electrode set to contain the solution while not affecting the fluid movement. Two gasket thicknesses were used in these studies, 750 µm and 1050 µm (measured with solution in the cell), forming two cell volumes, 325 µL and 500 µL respectively. A glass slide was placed on top of the PDMS gasket to serve as the ceiling of the cell to limit vertical fluid movement and to prevent evaporation. A permanent NdFeB magnet was placed under the chip, generating a magnetic field perpendicular to the plane of the chip. Two permanent magnets (from Amazing Magnets LLC, Irvine, CA) of different strengths of magnetic field were used: 0.37 T (diameter of 1.5 in. and height of 0.5 in.) and 0.50 T (diameter of 2 in. and height of 1 in.). The magnetic field was measured at the array with a DC magnetometer, AlfaLab, Inc.

3.3.6 Magnetic Field Simulations. Figure 3a shows a cross-sectional view of the magnet, array chip, PDMS gasket, and glass slide lid with a superimposition of the magnetic field lines throughout the height of the 1050 µm thick cell. It also includes the coordinate system that is used throughout the paper. The z-component of the magnetic field lines was calculated for the surface adjacent to the cell for both the 0.37 T and 0.50 T permanent magnets using AMPERES

(see Figures 3.3b and 3.3c). The simulated magnitudes matched well with measurements with the DC magnetometer.

3.3.7 Electrochemical Experiments for Generating MHD Convection at Ring-disk Electrodes. For these MHD studies, a two-electrode configuration was used where the disk electrode served as the working electrode while the ring electrode served as the auxiliary and quasi-reference electrode. The ionic current needed for MHD convection was generated by applying a current to the disk electrode. First, the film was reduced by applying a cathodic current until a cutoff potential of -1.00 V was reached to charge the film. The current bias was immediately switched and an anodic current was applied until a cutoff potential of +1.00 V was reached to protect the PEDOT film from over-oxidation. The flow profiles during the anodic portion of the applied current experiments were examined. Anodic currents of -2.5 μA and -5.0 μA were examined and their flow profiles were compared.

3.3.8 Visualization of Fluid Movement and Data Analysis. Fluid flow was visualized by tracking 10 μm polystyrene beads in the cell solution under a microscope interfaced to a Sony Handycam. The x- and y- position of the recorded video was adjusted by moving the microscope stage. The z- position (height within the cell) was controlled by adjusting the focal plane of the microscope objective. A 50 μL solution of 10 μm polystyrene beads was mixed with a 1 mL solution of 0.100 M NaCl, changing the concentration of NaCl to 0.095 M. The movement of beads that were within ±75 μm of the focal plane of the microscope was captured on video and averaged over the duration of the experiment using particle imaging velocimetry (PIV) analysis (Dynamic Studios). PIV analysis calculates the 2D velocity of the beads breaking the video into square interrogation regions, identifying bead patterns over subsequent frames, and measuring the displacement over time to give the average velocity. The scale of the video frames was determined by initially focusing on an electrode feature of known dimension.

3.3.9 Mapping of Fluid Flow around Ring-disk Electrodes throughout Height of Cell. The fluid flow profile was examined at several heights throughout the cell to give a full picture of the fluid dynamics. For experiments with the 750 μm thick gasket, the fluid flow was examined at 150, 300, 450, 600, and 675 μm above the surface of the chip. For experiments with the 1050

μm thick gasket, the fluid flow was examined at 150, 300, 450, 600, 750, and 900 μm above the surface of the chip. At each height, four applied current experiments were done and the velocity vectors along the diameter of the ring electrode were averaged together (see Figure 3.5). A filled contour plot for each of the MHD experiments was made by plotting the distance from the chip surface (μm) versus the distance from the center of the disk electrode (μm) as the xy-plane and the average fluid speed (scaled in color). Positions where measurements were taken are represented as white dots on the contour plots.

3.4 Results and Discussion

3.4.1 Characterization of Microdisk Electrode Before and after PEDOT Modification.

MHD force is proportional to the ionic current density; therefore it is beneficial to understand the electrochemistry at the electrodes. The microdisk electrode was characterized before electrodeposition of PEDOT in both electrolyte alone and in a low concentration of solution-based redox species 2.5 mM $Ru(NH_3)_6^{2+}$ and 2.5 mM $Ru(NH_3)_6^{3+}$ in 0.100 M NaCl (Figure 3.2). After deposition, the PEDOT-modified disk electrode was characterized in 0.100 M NaCl. The current response over time during CA experiments was modeled using the equation with an R^2 value of 0.9577:

$$i(t) = \frac{E}{R_s} e^{(-t/R_s C_d)} = (-7.513 \times 10^{-6} \pm 3.499 \times 10^{-8}) e^{(-t/9.009 \times 10^{-4})} \quad (2)$$

R_s of the bare gold microelectrode was calculated to be 39.931 kΩ using the coefficient in the equation from the best fit line. The current response for the CA experiments was integrated from t = 0 s to t = 20 s to determine the number of coulombs available for pumping. The calculated coulombs were 0.04589 μC, 2.922 μC, and 34.59 μC for bare electrodes in 0.1 M NaCl, in $Ru(NH_3)_6^{2+/3+}$, and PEDOT-modified electrodes in 0.1 M NaCl respectively. During an applied potential of +1.00 V, the maximum current was 84.97 μA (13.7× higher than 2.5 mM $Ru(NH_3)_6^{2+/3+}$). The time constant was calculated by finding the time for 67% of the maximum current. The lower the time constant, the faster the current response and, therefore, capable of higher fluid velocities. The time constant for the bare disk electrode, was the lowest at 0.006 s,

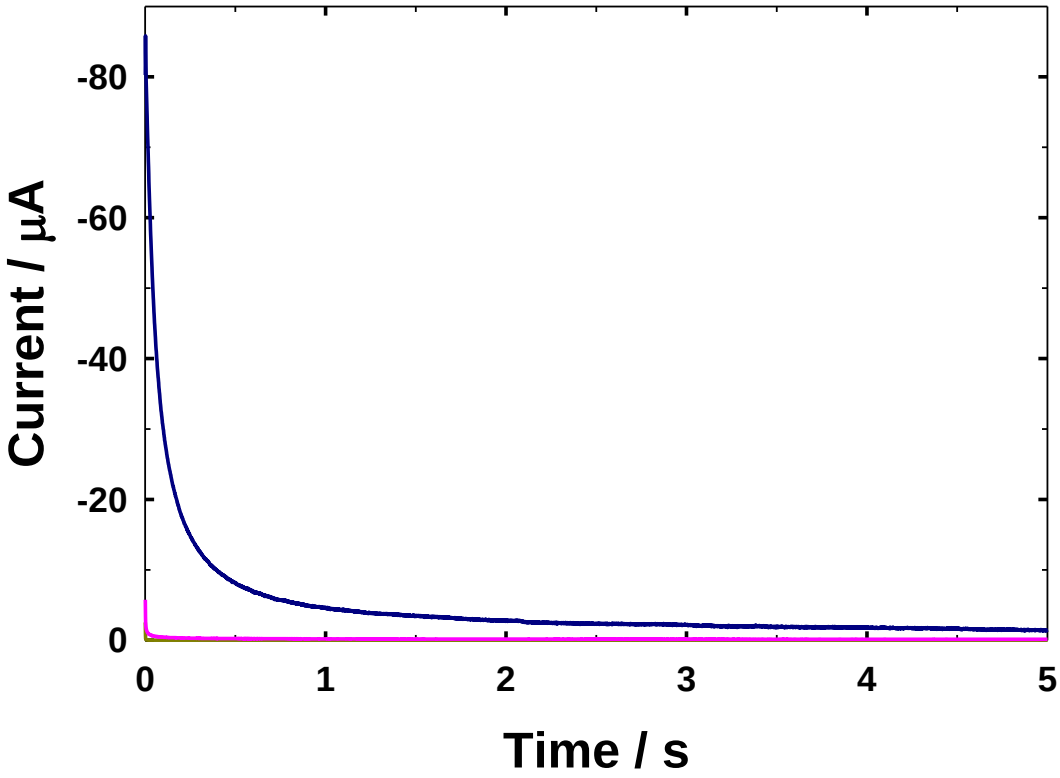

Figure 3.2. Characterization of the disk electrode before and after deposition of PEDOT using chronoamperometry (stepped from 0 V to 0.3 V for the bare and 1.0 V for PEDOT-modified electrode). The bare disk electrode was characterized in 0.1 M NaCl (gold line) and in 2.5 mM $Ru(NH_3)_6^{2+}$/2.5 mM $Ru(NH_3)_6^{3+}$ (pink line) vs. a bare gold quasi-reference ring electrode. The PEDOT-modified disk electrode was characterized in 0.1 M NaCl (blue line) vs. a PEDOT-modified gold quasi-reference ring electrode. These studies were performed in the absence of a magnet and without the addition of microbeads in the solution.

indicating a fast current response, but the current decreased quickly, making it unsuitable for MHD. Bare electrodes in $Ru(NH_3)_6^{2+/3+}$ had a similar time constant (0.004 s), but were capable of higher currents. At PEDOT-modified electrodes, the redox species is immobilized to the electrode surface; therefore, the maximum current is much higher and is sustained over a longer time (time constant of 0.092 s), which is advantageous for MHD applications. It should also be noted that the PEDOT films protect the gold microelectrodes at more extreme oxidation potentials, expanding the potential window of the electrode.

3.4.2 Simulations of Magnetic Flux Density. Eq. 1 asserts that for a given magnetic field, the MHD force, and therefore, fluid flow, should track the ionic current density. Due to a fairly uniform magnetic field, this should mostly hold true. Figure 3.3b and 3.3c show B_z for the area of solution above the ring electrode. For the 0.37 T magnet, the average B_z across the ring electrode is 0.347 ± 0.002 T, representing above 99+% of the magnetic field. B_z only changes by 0.0034 T, or 1.7 T/m laterally over the area across the ring electrode. B_z changes the most vertically by 0.021 T, or 10.3 T/m. For the 0.5 T magnet, the average B_z across the ring electrode is 0.447 ± 0.001 T, representing over 99+% of the magnetic field. B_z changes by 0.002 T laterally, or 1 T/m and by 0.016 T, or 8 T/m. B_x and B_y are very small in comparison and contribute very little to the overall fluid flow.

3.4.3 Two-Dimensional Evaluation of Horizontal Fluid Flow Around Ring-Disk Electrodes. Figure 3.4 shows top-down (Figure 3.4a) and cross-sectional schematics of the MHD force, ionic current density, and magnetic field (Figure 3.4b) at PEDOT-modified ring-disk electrodes. Figure 3.4c shows the electrochemistry at the anode. When PEDOT is oxidized to its +1 oxidation state, chlorine ions enter the film to compensate for the change in charge. The movement of ions between the working and auxiliary electrodes is the ionic current density needed for pumping. The flow pattern in the gap between concentric disk and ring electrodes was quantified using PIV analysis at several different heights throughout the electrochemical cell (see Figure 3.5). By examining the flow velocity vectors along the diameter of the ring electrode, it is evident that the highest velocity for a given height is close to the disk electrode. After this maximum, the fluid speed decreases with increasing distance from the disk electrode.

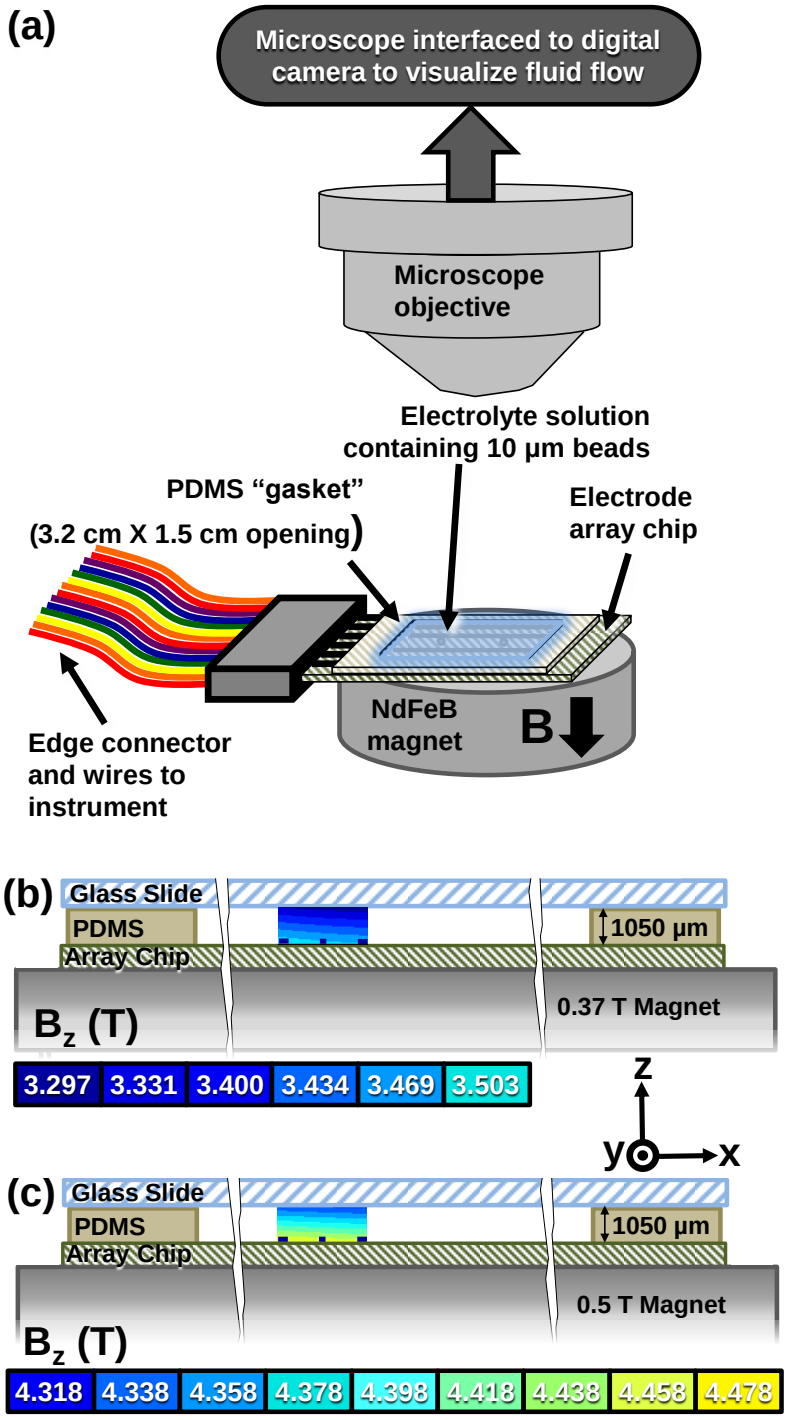

Figure 3.3 (a) Experimental setup for visualizing redox-MHD fluid flow: the magnet, chip, and electrochemical cell are placed under a microscope for viewing 10 μm polystyrene beads that are added to the solution. Simulation of the z-component of the magnetic field in the cell for (b) the 0.37 T magnet, and (c) the 0.5 T magnet.

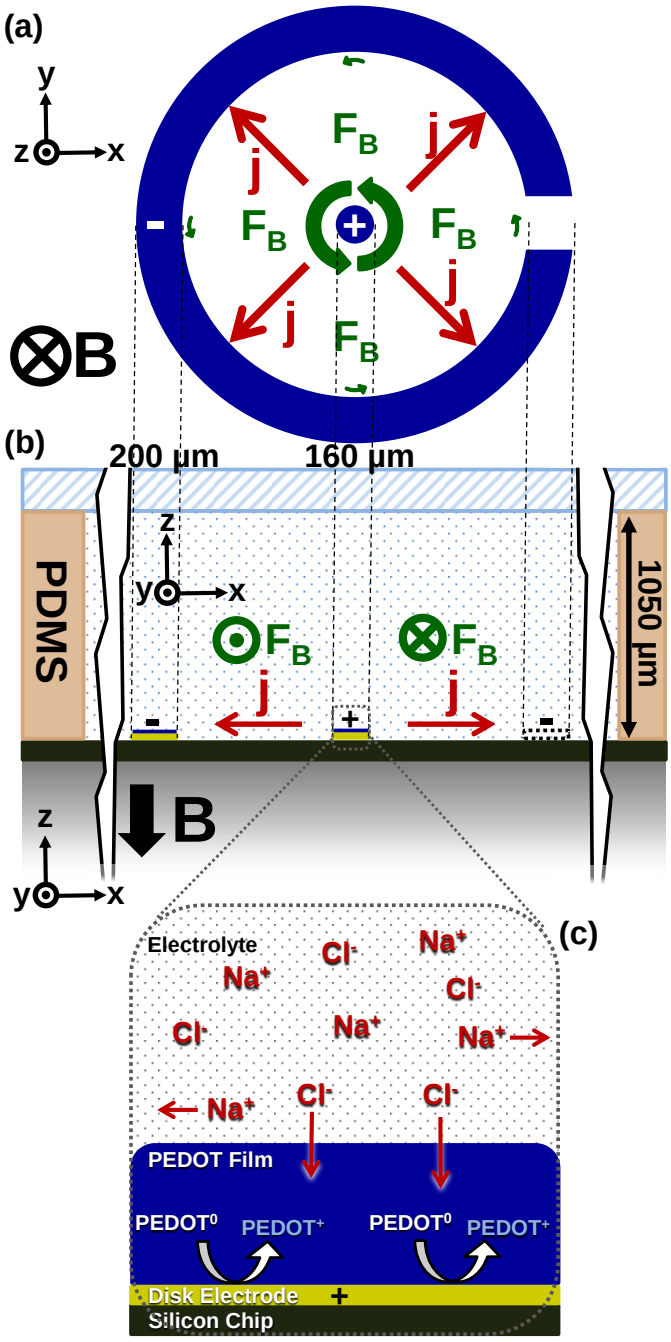

Figure 3.4. (a) Top-down schematic of the forces governing redox-MHD at the PEDOT-modified concentric ring-disk electrodes. The MHD force is perpendicular to ionic current density and the magnetic field, producing rotational flow around the disk electrode, faster at the disk and slower at the ring. (b) Cross sectional schematic of the forces. The widths of the electrodes, gaps between them, and the height of the electrochemical cell are drawn to-scale. (c) Expanded view of the overall mechanism involved in the oxidation of the PEDOT film on the anode, showing incorporation of anions into the film and simultaneous migration of cations toward the cathode.

This corresponds to the decrease in ionic current density which results from the difference in vertical cross sectional area from the edge of the disk (3.77×10^{-3} cm^2) to the edge of the ring electrode (3.77×10^{-2} cm^2) for a cell height of 750 µm. Figure 3.5 shows the change in fluid flow speed with increasing radial distance from the disk electrode at 150 µm above the chip during an applied current experiment of -2.5 µA in the presence of a 0.37 T magnetic field. This relationship is fairly linear between -175 µm and -800 µm and between 350 µm and 800 µm. The least squares best fit for these two regions are $|v| = (0.01707 \pm 0.001324\ s^{-1})d + (21.99 \pm 0.6918\ \mu m \cdot s^{-1})$ and $|v| = (-0.01588 \pm 0.0008395\ s^{-1})d + (22.09 \pm 0.4949\ \mu m \cdot s^{-1})$ with R^2 values of 0.965 and 0.989 respectively where $|v|$ is the horizontal fluid speed and d is the distance from the center of the disk electrode. The radial change in fluid speed creates a swirling type flow, which could be of value for mixing applications. The x-intercepts for both the side with the complete ring electrode and the side with the opening in the ring electrode indicate that the flow extends beyond the ring electrode. The x-intercepts, which represents where the flow has a magnitude of zero, are -1288 ± 107.8 µm and 1391 ± 80.21 µm respectively and are not significantly different. The flow on the outside of the ring electrode is in the same direction as the flow within, but is much smaller in magnitude, (average of 0.6324 ± 0.6642 µm·s-1 on the side with the complete ring and 3.337 ± 2.074 µm·s-1 on the side with the opening) indicating that the ionic current density between the disk and ring electrode is dominant. This feature suggests that fluid motion can be localized to a certain area on a chip without walls or wells. Another feature of the fluid flow is the dramatic decrease in the horizontal fluid speed directly over the disk electrode, approximately where the center of fluid flow rotation occurs. This can partially be explained by the ionic current distribution at the disk electrode. Most of the ionic current is concentrated at the edge of the disk electrode and that in the center is dominated by its vertical component, which is parallel with the magnetic field, and thus does not contributing to the MHD force. Shear forces caused by flows of opposing direction on either side of the disk could also contribute to the lower magnitude of fluid flow speeds over the disk electrode. These observations have been made in redox-MHD at the same electrode

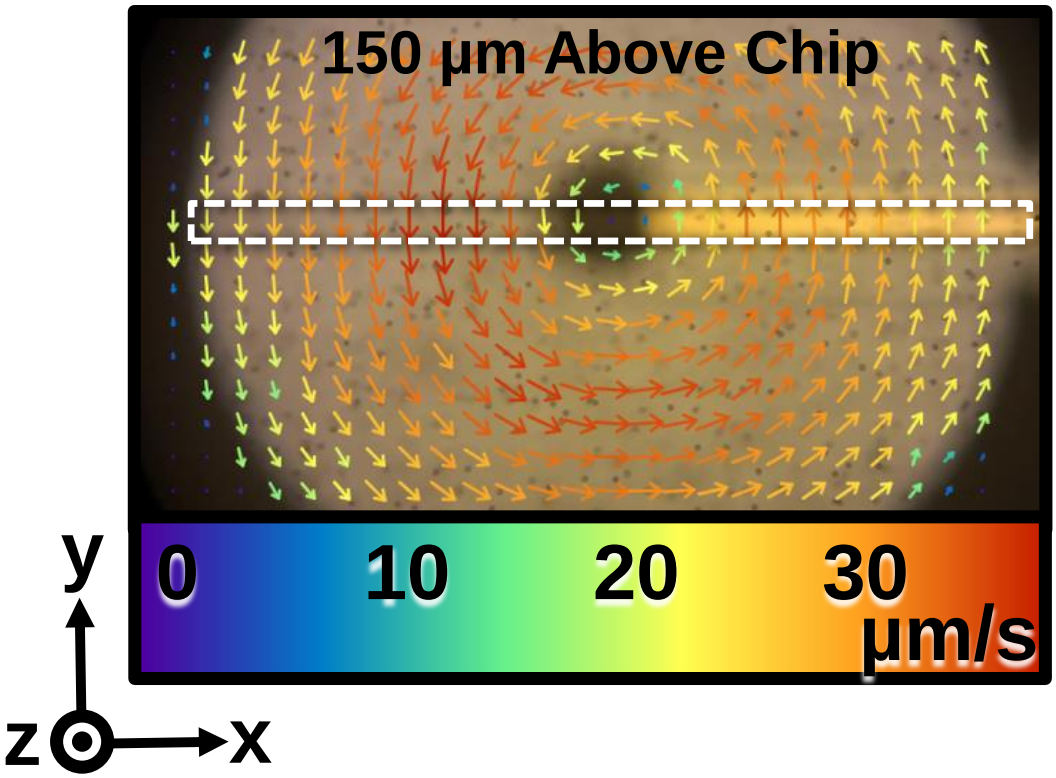

Figure 3.5. PIV image showing velocity vectors and quantifying fluid flow at the ring-disk electrode geometry. The PIV image was taken 150 µm above the chip in the presence of a 0.37 T magnet during an applied current experiment of -2.5 µA. The PDMS gasket was 750 µm thick. Bead speed was taken across the horizontal diameter of the ring electrode (shown in white dashed box).

geometry but unmodified and with solution-based redox species (0.1 M of each form of $Fe(CN)_6^{3-/4-}$ in 0.1 M KCl).[40] It was suggested in that system that density gradients could play a role as well, but is not likely at work here, because redox species were not added to the solution and thus a diffusion layer does not develop. Supporting this argument is the fact that we have not observed fluid motion due to density gradients at our PEDOT-modified electrodes during electrochemical experiments in the absence of a magnetic field (see discussion in Supporting Information).

3.4.4. Asymmetry of Rotational Flow Profile. From careful examination of the PIV images, there is an obvious difference between the peak magnitude of fluid flow speed on either side of the disk electrode. This difference exists because of the 280 µm long opening in the ring electrode which allows passage of the lead from the disk electrode to the contact pad so that both disk and ring electrodes can be individually addressed (Figure 3.6a). Figure 3.6b shows that the solution adjacent to the opening in the ring electrode has lower speed (by 8.2 %) than the solution on the other side of the disk electrode, indicating lower ionic current density. Figure 3.6c and 3.6d show PIV images for both sides of the disk electrode whose vectors were used to make Figure 3.6b. These images also show the flow outside of the ring electrode. According to the continuity equation for a steady state process:

$$\frac{\partial \rho}{\partial t} + \nabla \cdot (\rho \vec{u}) = 0 \tag{3}$$

where ρ is the fluid density, t is time and $\vec{u}$ is the flow velocity vector field, the mass that enters the field must be equal to the mass that leaves the field. For an incompressible fluid where the density remains constant, the equation can be simplified to a volume continuity equation:

$$\nabla . \vec{u} = 0 \tag{4}$$

The displaced volume on either side of the disk electrode must match. Therefore, in order for a discrepancy in magnitude of fluid speed on opposite sides of the disk to exist, the fluid flow next to the gap must expand horizontally outward beyond the ring electrode. The integration of the average fluid speed over the distance from the edge of disk electrode to 500 µm outside of the

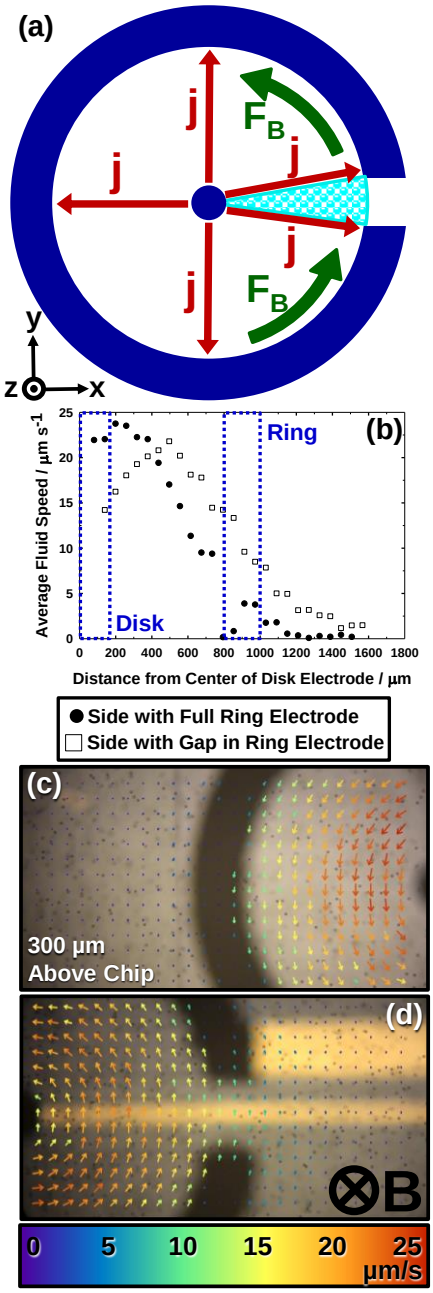

Figure 3.6 (a) Top-down schematic of redox-MHD at concentric ring-disk electrodes showing forces subjected on volume of solution in the gap between the electrodes. (b) Overlay of bead speed versus absolute distance from the center of the disk electrode for the side where the ring electrode is complete and for the side where the ring electrode has an opening to accommodate passage of the lead from the disk electrode. (c) PIV image showing fluid flow on side with complete ring electrode. (d) PIV image on side with opening in ring electrode. The videos taken for these experiments were focused 300 µm above the chip.

ring electrode (Figure 3.6b) for the side with the complete ring (13,898 $\mu m^2 \cdot s^{-1}$) and for the side with the gap in the ring electrode (16,291 $\mu m^2 \cdot s^{-1}$). The fluid fluxes on both sides of the disk electrode differ by 16%. These fluid fluxes were calculated at a single height in the cell (300 µm). The discrepancy between the two sides most likely results from the vertical distribution of fluid flow. In addition, the difference in the distance from the center of the disk electrode where the maximum fluid speed occurs supports this explanation

3.4.5 Effect of Cell Height on Rotational Flow Profile. For these studies, two cell heights were investigated: 750 µm and 1050 µm. In the past, we have used a cell height of 750 µm (620 µm when measured dry) more MHD experiments at PEDOT-modified microband electrodes and at bare microring-disk electrodes in solution-based redox species.[40] A 1050 µm cell height was chosen because it is about 50% more than the other. In a pressure-driven flow, the highest fluid flow speed would be located in the middle of the cell due to no-slip boundary conditions at the floor and ceiling of the cell. For both cell heights, the maximum speed occurred at 300 µm above the chip surface regardless of cell height, rather than in the middle of the cell. This effect is due to the ionic current density distribution throughout the height of the cell. Closer to the electrodes, the electric field and therefore ionic current density is strongest in the direction perpendicular to the magnetic field. Increases in magnetic or electric field will result in increases in fluid speed that will be observable closer to the electrodes where the electric field is parallel to the chip surface. For this given electrode geometry at 600 µm or more above the chip surface, the ionic current density is low and does not increase with applied current and magnetic field. From the magnetic flux density simulations, the z-component of the magnetic field throughout a 1050 µm cell height changes by 5.88% and 3.57% from the chip to the ceiling for the 0.37 T and 0.5 T magnet respectively. In these regions at the top of the cell, the fluid flow is much lower than what can be attributed to the change in magnetic field throughout the cell. Therefore, the fluid flow is caused by much lower ionic current density ($\mathbf{j_x}$) and by transfer of momentum from the fluid below that is propelled by $\mathbf{F_B}$. Consequently, for the studies described below on the effects of applied current and magnetic flux density on fluid flow, only the cross-sectional area between the

chip surface and 600 µm above the chip and between the outside of the disk electrode and the inside of the ring electrode was considered. The fact that the lid and therefore the no slip boundary condition has moved farther away from the active electrodes should have influenced the fluid flow, essentially, allowing it to be higher for a fixed point for the higher cell. However, this is not the case. This suggests that the current density becomes more diluted, offsetting the diminished resistance to flow. The ionic current distributions will be simulated and reported upon in future papers.

3.4.6 Effect of Magnitude of Applied Current on Rotational Flow Profile. Fluid speed can be carefully controlled to meet the requirements of specific applications by adjusting the magnitude of the applied current as we have shown previously for parallel band electrode geometries and with redox species in solution.[41] Two magnitudes of applied current (-2.5 and -5.0 µA) were investigated in the presence of a 0.37 T magnetic field with cell heights of 750 and 1050 µm. Assuming a constant magnetic field, it is predicted that doubling the magnitude of the applied current should double the MHD force, and have a similar doubling effect on the fluid speed between the ring-disk electrodes. For each experiment, the average speed versus distance from center of disk electrode was plotted for each height. Flow rates ($\mu m^3 \cdot s^{-1}$) were determined from these curves between -80 µm and -800 µm from the disk electrode and for each height below 600 µm. The curves were integrated with respect to distance from the disk electrode and the height to determine the average flow rate. For the 750 µm thick cell (Figure 3.7a and c), the flow flux increased by a factor of 1.98. For the 1050 µm thick cell (Figure 3.7b and d), the flow flux increased by a factor of 1.95 (see Table 1). These results are consistent with a proportional enhancement to the MHD force and therefore fluid speed with the magnitude of the applied current.

3.4.7 Effect of Magnetic Flux Density on Rotational Flow Profile. Two magnetic flux densities were investigated, 0.37 T and 0.5 T, for both cell heights, 750 µm and 1050 µm. According to eq. 1, the MHD force also should be proportional to the magnetic field strength. We have reported such a linear dependence for a fixed geometry at band electrodes previously.[24] Therefore, the fluid speed generated with 0.5 T permanent magnet should be a factor of 1.35

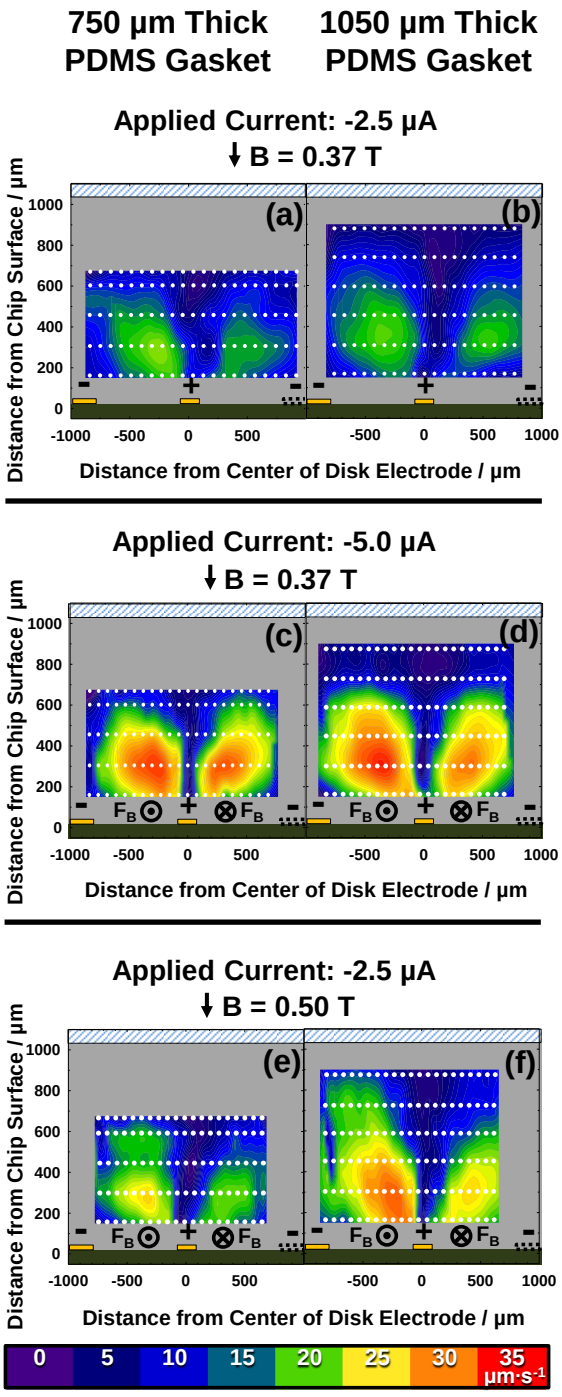

Figure 3.7 Contour plots illustrating horizontal fluid flow versus distance from center of disk electrode throughout the height of the electrochemical cell and comparing the effects of different applied currents, -2.5 µA (a, b, e, and f) and -5.0 µA (c and d), different cell heights 750 µm (a, c, and e) and 1050 µm (b, d, and f), and different magnetic flux densities, 0.37 T (a, b, c, and d) and 0.5 T (e and f).

that generated with 0.37 T magnet. The flow flux was calculated using the same method described above. For the 750 μm thick cell, the flow flux increased by a factor of 1.32 when the magnetic field strength was increased by a factor of 1.35 (Figure 3.7a and 3.7e). For the 1050 μm thick cell, the flow flux increased by a factor of 1.36 (Figure 3.7b and 3.7f) (see Table 1). These results demonstrate that the MHD force, and therefore the fluid speed at disk-ring geometry with PEDOT-modified electrodes increases proportionally with B, and is consistent with the prior work involving other geometries and redox species in solution.

3.5 Conclusions

This study demonstrates rotational flow at PEDOT-modified concentric ring-disk electrodes in a microfluidic setting via redox-MHD without fabrication of walls, channels, or valves and without the presence of redox species in solution. The absence of redox species in solution broadens the range of viable microfluidic applications for redox-MHD. It was demonstrated that the fluid flow could be fine-tuned by adjusting the magnitude of applied current or magnetic field. The swirling flow resulting from non-uniform distribution of ionic current between disk and ring electrodes could be useful for microfluidic mixing and stirring applications such as immunoassays, DNA hybridization, and on-chip reactions. Future work will focus on extending the amount of time that pumping can be sustained in a single direction by improving the coulombic capacity of the deposited PEDOT films.

3.6 Supporting Information

This document contains additional discussion on the electrochemical characterization of the microdisk electrode before and after deposition. It also includes a discussion on the lack of density gradients at PEDOT-modified electrodes as well as a video of bead movement during an applied potential experiment (+1 V) in the absence of a magnetic field. In addition, there is a video of bead movement during an applied current (-2.5 μA) experiment in the presence of a 0.37 T magnet.

3.7 Acknowledgements

Research was supported through the National Science Foundation (NSF) (CHE-0719097 and CBET-1336853) and the Arkansas Biosciences Institute, the major research component of the Arkansas Tobacco Settlement Proceeds Act of 2000.

3.8 References

(1) Polson, N. A.; Hayes, M. A. *Analytical chemistry* **2001**, *73*, 312 A-319 A.

(2) Whitesides, G. M. *Nature* **2006**, *442*, 368-373.

(3) Figeys, D.; Pinto, D. *Analytical Chemistry* **2000**, *72*, 330 A-335 A.

(4) Nguyen, N.-T.; Huang, X.; Chuan, T. K. *Journal of Fluids Engineering* **2002**, *124*, 384-392.

(5) Stone, H. A.; Stroock, A. D.; Ajdari, A. *Annu. Rev. Fluid Mech.* **2004**, *36*, 381-411.

(6) Amirouche, F.; Zhou, Y.; Johnson, T. *Microsystem Technologies* **2009**, *15*, 647-666.

(7) Weston, M. C.; Gerner, M. D.; Fritsch, I. *Analytical Chemistry*, *82*, 3411-3418.

(8) Anderson, E. C.; Weston, M. C.; Fritsch, I. *Analytical Chemistry*, *82*, 2643-2651.

(9) Weston, M. C.; Nash, C. K.; Fritsch, I. *Analytical Chemistry*, *82*, 7068-7072.

(10) Fritsch*, M. C. W. a. I. *Sensors and Actuators B* **Submitted**.

(11) Preston G. Scrape, M. D. G., Melissa C. Weston, and Ingrid Fritsch* *Analytical Chemistry* **Soon to be submitted**.

(12) Weston, M. C.; Nash, C. K.; Fritsch, I. *Analytical Chemistry* **2010**, *82*, 7068-7072.

(13) Cheah, L. T.; Fritsch, I.; Haswell, S. J.; Greenman, J. *Biotechnology and Bioengineering* **2012**, *109*, 1827-1834.

(14) Buttry, D. A.; Anson, F. C. *Journal of the American Chemical Society* **1983**, *105*, 685-689.

(15) Bertoncello, P.; Ciani, I.; Marenduzzo, D.; Unwin, P. R. *The Journal of Physical Chemistry C* **2006**, *111*, 294-302.

(16) Fritsch-Faules, I.; Faulkner, L. R. *Analytical Chemistry* **1992**, *64*, 1118-1127.

(17) Wang, B.; Brown, S.; Rusling, J. F. *Electroanalysis* **2005**, *17*, 1601-1608.

(18) Forster, R. J.; Vos, J. G.; Lyons, M. E. G. *Journal of the Chemical Society, Faraday Transactions* **1991**, *87*.

(19) Vidal, J.-C.; Garcia-Ruiz, E.; Castillo, J.-R. *Microchimica Acta* **2003**, *143*, 93-111.

(20) Malhotra, B. D.; Chaubey, A.; Singh, S. P. *Analytica Chimica Acta* **2006**, *578*, 59-74.

(21) Gerard, M.; Chaubey, A.; Malhotra, B. D. *Biosensors and Bioelectronics* **2002**, *17*, 345-359.

(22) Wang, X.; Sjoberg-Eerola, P.; Eriksson, J.-E.; Bobacka, J.; Bergelin, M. *Synthetic Metals* **2010**, *160*, 1373-1381.

(23) Poverenov, E.; Li, M.; Bitler, A.; Bendikov, M. *Chemistry of Materials* **2010**, *22*, 4019-4025.

(24) Bobacka, J.; Lewenstam, A.; Ivaska, A. *Journal of Electroanalytical Chemistry* **2000**, *489*, 17-27.

(25) Tamburri, E.; Orlanducci, S.; Toschi, F.; Terranova, M. L.; Passeri, D. *Synthetic Metals* **2009**, *159*, 406-414.

(26) Groenendaal, L.; Jonas, F.; Freitag, D.; Pielartzik, H.; Reynolds, J. R. *Advanced Materials* **2000**, *12*, 481-494.

(27) Kumar, S.; Mathiyarasu, J.; Phani, K.; Yegnaraman, V. *Journal of Solid State Electrochemistry* **2006**, *10*, 905-913.

(28) Xiao, Y.; Li, C. M.; Wang, S.; Shi, J.; Ooi, C. P. *Journal of Biomedical Materials Research Part A* **2009**, *92A*, 766-772.

(29) Sakmeche, N.; Aeiyach, S.; Aaron, J.-J.; Jouini, M.; Lacroix, J. C.; Lacaze, P.-C. *Langmuir* **1999**, *15*, 2566-2574.

(30) Sakmeche, N.; Bazzaoui, E. A.; Fall, M.; Aeiyach, S.; Jouini, M.; Lacroix, J. C.; Aaron, J. J.; Lacaze, P. C. *Synthetic Metals* **1997**, *84*, 191-192.

(31) Manisankar, P.; Vedhi, C.; Selvanathan, G.; Gurumallesh Prabu, H. *Journal of Applied Polymer Science* **2007**, *104*, 3285-3291.

(32) Weston, M. C.; Gerner, M. D.; Fritsch, I. *Analytical Chemistry* **2010**, *82*, 3411-3418.

(33) Qian, S.; Bau, H. H. *Mechanics Research Communications* **2009**, *36*, 10-21.

(34) Pamme, N. *Lab on a Chip* **2006**, *6*, 24-38.

(35) Anderson, E. C.; Weston, M. C.; Fritsch, I. *Analytical Chemistry* **2010**, *82*, 2643-2651.

(36) Sahore, V.; Fritsch, I. *Microfluidics and Nanofluidics* **2014**, 1-8.

(37) Scrape, P. G.; Gerner, M. D.; Weston, M. C.; Fritsch, I. *Journal of The Electrochemical Society* **2013**, *160*, H338-H343.

(38) Cui, X.; Martin, D. C. *Sensors and Actuators B: Chemical* **2003**, *89*, 92-102.

(39) Randriamahazaka, H.; Noel, V.; Chevrot, C. *Journal of Electroanalytical Chemistry* **1999**, *472*, 103-111.

(40) Hass, R.; García-Cañadas, J.; Garcia-Belmonte, G. *Journal of Electroanalytical Chemistry* **2005**, *577*, 99-105.

(41) Snook, G. A.; Peng, C.; Fray, D. J.; Chen, G. Z. *Electrochemistry communications* **2007**, *9*, 83-88.

(42) Kayinamura, Y. P.; Roberts, J. H.; Rubinson, J. F. *ACS applied materials & interfaces* **2012**, *4*, 1601-1607.

(43) Kayinamura, Y. P.; Ovadia, M.; Zavitz, D.; Rubinson, J. F. *ACS applied materials & interfaces* **2010**, *2*, 2653-2662.

(44) Rozlosnik, N. *Analytical and bioanalytical chemistry* **2009**, *395*, 637-645.

(45) Green, R. A.; Lovell, N. H.; Wallace, G. G.; Poole-Warren, L. A. *Biomaterials* **2008**, *29*, 3393-3399.

(46) Ludwig, K. A.; Uram, J. D.; Yang, J.; Martin, D. C.; Kipke, D. R. *Journal of neural engineering* **2006**, *3*, 59.

(47) Bello, A.; Giannetto, M.; Mori, G.; Seeber, R.; Terzi, F.; Zanardi, C. *Sensors and Actuators B: Chemical* **2007**, *121*, 430-435.

(48) Colleran, J. J.; Breslin, C. B. *Journal of Electroanalytical Chemistry* **2012**, *667*, 30-37.

(49) Xiao, Y. H.; Li, C. M.; Toh, M. L.; Xue, R. *Journal of applied electrochemistry* **2008**, *38*, 1735-1741.

(50) Vedrine, C.; Fabiano, S.; Tran-Minh, C. *Talanta* **2003**, *59*, 535-544.

(51) Fabiano, S.; Tran-Minh, C.; Piro, B. Ì. t.; Dang, L. A.; Pham, M. C.; Vittori, O. *Materials Science and Engineering: C* **2002**, *21*, 61-67.

(52) Istamboulie, G.; Sikora, T.; Jubete, E.; Ochoteco, E.; Marty, J.-L.; Noguer, T. *Talanta*, *82*, 957-961.

(53) Piro, B. Ì. t.; Dang, L. A.; Pham, M. C.; Fabiano, S.; Tran-Minh, C. *Journal of Electroanalytical Chemistry* **2001**, *512*, 101-109.

(54) Sahore, V.; Fritsch, I. *Analytical Chemistry* **2013**.

(55) Weston, M. C.; Fritsch, I. *Sensors and Actuators B: Chemical* **2012**, *173*, 935-944.

(56) Weston, M. C.; Nash, C. K.; Homesley, J. J.; Fritsch, I. *Analytical Chemistry* **2012**, *84*, 9402-9409.

(57) Yang, N.; Zoski, C. G. *Langmuir* **2006**, *22*, 10338-10347.

(58) Audebert, P.; Miomandre, F. *Handbook of conducting polymers* **2007**, *3*.

(59) Ping-Ping, S.; Zheng-Hao, W. *Chinese Journal of Chemistry* **2005**, *23*, 806-810.

(60) Abgrall, P.; Gue, A. M. *Journal of Micromechanics and Microengineering* **2007**, *17*, R15.

(61) Ottino, J. M.; Wiggins, S. *Philosophical Transactions of the Royal Society of London. Series A: Mathematical, Physical and Engineering Sciences* **2004**, *362*, 923-935.

(62) Nguyen, N.-T.; Wu, Z. *Journal of Micromechanics and Microengineering* **2005**, *15*, R1.

(63) Lee, C.-Y.; Chang, C.-L.; Wang, Y.-N.; Fu, L.-M. *International journal of molecular sciences*, *12*, 3263-3287.

(64) Hessel, V.; Löwe, H.; Schönfeld, F. *Chemical Engineering Science* **2005**, *60*, 2479-2501.

(65) Mansur, E. A.; Ye, M.; Wang, Y.; Dai, Y. *Chinese Journal of Chemical Engineering* **2008**, *16*, 503-516.

(66) Jang, J.; Lee, S. S. *Sensors and Actuators A: Physical* **2000**, *80*, 84-89.

(67) Homsy, A.; Koster, S.; Eijkel, J. C. T.; van den Berg, A.; Lucklum, F.; Verpoorte, E.; de Rooij, N. F. *Lab on a Chip* **2005**, *5*, 466-471.

(68) Zhong, J.; Yi, M.; Bau, H. H. *Sensors and Actuators A: Physical* **2002**, *96*, 59-66.
(69) Aref, H. *Journal of fluid mechanics* **1984**, *143*, 1-21.

(70) Yi, M.; Qian, S.; Bau, H. H. *Journal of Fluid Mechanics* **2002**, *468*, 153-177.

(71) West, J.; Karamata, B.; Lillis, B.; Gleeson, J. P.; Alderman, J.; Collins, J. K.; Lane, W.; Mathewson, A.; Berney, H. *Lab on a Chip* **2002**, *2*, 224-230.

(72) West, J.; Gleeson, J. P.; Alderman, J.; Collins, J. K.; Berney, H. *Sensors and Actuators B: Chemical* **2003**, *96*, 190-199.

(73) Gelb, A.; Gleeson, J. P.; West, J.; Roche, O. M. *SIAM Journal on Applied Mathematics* **2004**, *64*, 1294-1310.

(74) Lemoff, A. V.; Lee, A. P. *Sensors and Actuators B: chemical* **2000**, *63*, 178-185.

(75) Lemoff, A. V.; Lee, A. P. *Biomedical microdevices* **2003**, *5*, 55-60.

(76) Eijkel, J. C. T.; Dalton, C.; Hayden, C. J.; Burt, J. P. H.; Manz, A. *Sensors and Actuators B: Chemical* **2003**, *92*, 215-221.

(77) Ragsdale, S. R.; White, H. S. *Analytical Chemistry* **1999**, *71*, 1923-1927.

(78) Sekli-Belaidi, F.; Temple-Boyer, P.; Gros, P. *Journal of Electroanalytical Chemistry* **2010**, *647*, 159-168.

(79) Sahore, V., UNIVERSITY OF ARKANSAS, 2013.

Table 1: Comparison of fluid behavior for different applied currents, magnetic fields, and cell heights

Cell Height of 750 µm			
B / T	**0.37**	**0.37**	**0.50**
j / µA	**-2.5**	**-5.0**	**-2.5**
Flow Rate / $\mu m^3 \cdot s^{-1}$	4.04×10^6	8.01×10^6	5.32×10^6
Factor Increase	1	1.98	1.32
Max Velocity / $\mu m \cdot s^{-1}$	20.6	32.9	24.9
Factor Increase	1	1.59	1.21
Cell Height of 1050 µm			
Flow Rate / $\mu m^3 \cdot s^{-1}$	4.98×10^6	9.72×10^6	6.76×10^6
Factor Increase	1	1.95	1.36
Max Velocity / $\mu m \cdot s^{-1}$	18.9	34.1	26.8
Factor Increase	1	1.81	1.42

3.S Supporting Information: Redox-Magnetohydrodynamic (MHD) Microfluidics at Poly(3,4-ethylenedioxythiophene)-Modified Concentric Disk and Ring Electrodes

This document contains additional discussion on the electrochemical characterization of the microdisk electrode before and after deposition. It also includes a discussion on the lack of density gradients at PEDOT-modified electrodes as well as a video of bead movement during an applied potential experiment (+1 V) in the absence of a magnetic field. In addition, there is a video of bead movement during an applied current (-2.5 μA) experiment in the presence of a 0.37 T magnet.

3.S1 Characterization via CV. For the CV studies, the charging current for bare gold microelectrodes in 0.100 M NaCl was plotted versus the scan rate. Using the slope of this plot, the effective electrode capacitance was calculated to be 1.129 mF/cm^2. Figure 3.S1 shows an overlay of the current responses for bare electrodes in 0.1 M NaCl and in 5 mM $Ru(NH_3)_6^{2+/3+}$ in 0.1 M NaCl and for PEDOT-modified electrodes in 0.1 M NaCl. The experimental peak current for CV in 5 mM $Ru(NH_3)_6^{2+/3+}$ was 0.1944 μA, and the peak splitting for the CV response of was 0.089 V. The peak splitting was higher than what is expected for a kinetically reversible redox species. This is due to the high uncompensated resistance that is common to microelectrodes. After electrodeposition, the PEDOT-modified electrodes were characterized in 0.100 M NaCl. The CV showed a large capacitive current response of ±0.4 μA (current at 0 V), which are characteristic of PEDOT films.

3.S2 Search for Density Gradients at PEDOT-modified Electrodes. Natural convection due to density gradient effects has been reported at microelectrodes in a solution of 0.1 M $K_3Fe(CN)_6$ and $K_4Fe(CN)_6$ in a supporting electrolyte of 0.1 M KCl.[42] This convection occurs when the electrochemistry at the electrode surface causes a change in fluid density from the bulk solution due to the migration of counter ions. This causes buoyant forces that induce fluid convection. The possibility of density gradients at PEDOT-modified electrodes was investigated during these studies. The same video microscopy experimental setup was used, but with an aluminum block (**B** = 0) underneath the chip rather than a magnet. Bead movement was recorded during an applied potential experiment of +1 V for 30 s. There is a slight movement of beads to the left, which is most likely due to a tilt in the chip. However, there is no movement resembling the fluid convection caused by density gradients.

3.S3 Captions for Videos

3S_001.mpg. Video of fluid movement around PEDOT-modified concentric ring-disk microelectrodes during an applied current (-2.5 μA) experiment in the presence of a 0.37 T magnet.

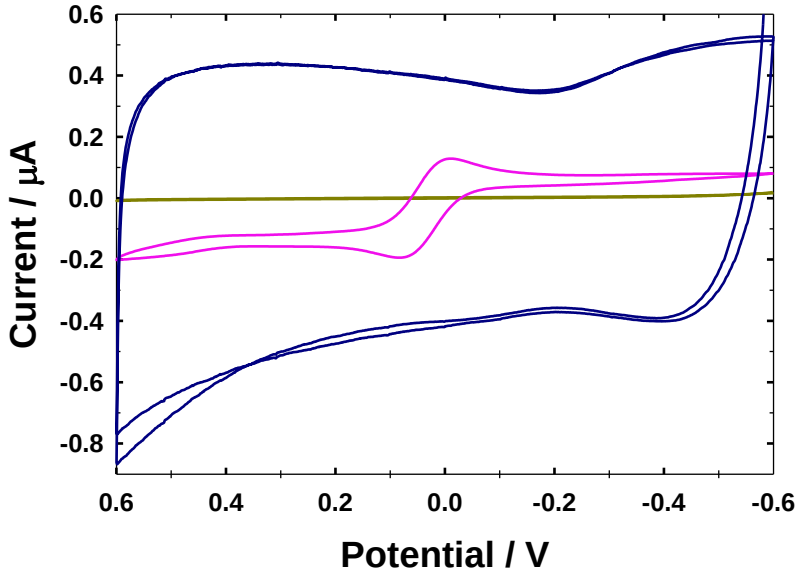

Figure 3.S1 Overlay of the current responses for bare electrodes in 0.1 M NaCl (gold) and in 5 mM $Ru(NH_3)_6^{2+/3+}$ in 0.1 M NaCl (pink) and for PEDOT-modified electrodes in 0.1 M NaCl (dark blue).

4. Fine-tuning Properties of Electrodeposited PEDOT films for Redox-Magnetohydrodynamic Microfluidic Applications Via Manipulation of Electrodeposition Conditions

4.1 Abstract

Redox-MHD is a relatively new microfluidic technique that takes advantages of the interaction between electric and magnetic fields. The MHD force is proportional to the ionic current density and magnetic field ($\mathbf{F_B} = \mathbf{j} \times \mathbf{B}$). Recently, conducting polymer poly(3,4-ethylenedioxythiophene), (PEDOT), has been deposited onto gold microelectrodes to generate the ionic current density needed for convection sufficient for microfluidic applications. This study focuses on increasing the MHD force by improving the current response and coulombic capacity of the PEDOT films. The films were deposited from aqueous solutions containing the monomer, 3,4-ethylenedioxythiophene, and anionic solubilizers. The solubilizer chosen has a profound effect on the film morphology and the electrochemical properties of the film. PEDOT films deposited in the presence of four different solubilizers (sodium dodecyl sulfate, bis(2-ethylhexyl) sulfosuccinate, 4-dodecylbenzene sulfonic acid, and polystyrene sulfonate) were investigated in this study using scanning electron microscopy, cyclic voltammetry, chronoamperometry, and electrochemical impedance spectroscopy. PEDOT films deposited in the presence of SDS produced the films with the best current response, coulombic capacity, and consistency. These electrodeposition conditions were used to modify gold microband electrodes and were used to generate redox-MHD microfluidic pumping.

4.2 Introduction

Magnetohydrodynamics is a fairly new microfluidic technique that takes advantage of the interaction between perpendicular electric and magnetic fields. When an ionic current density, **j**, is in the presence of a perpendicular magnetic field, **B**, a magnetic force, $\mathbf{F_B}$, is generated which induces fluid movement according to the equation $\mathbf{F_B} = \mathbf{j} \times \mathbf{B}$.[1-5] In order to maximize the magnetic force, and therefore, fluid flow velocity, ionic current density and magnetic field must be maximized. The magnetic field strength is limited by what permanent magnets are available commercially. Therefore, it is advantageous to optimize the magnitude of ionic current density that can be generated at the electrodes. This can be done through careful consideration of the redox species involved in the generation of **j**. Early on, MHD was generated by electrodes in saline solutions; this required the application of high voltages at the electrodes, which resulted in bubble generation from the electrolysis of water and electrode degradation.[2, 6-10] With the addition of redox species to solution, lower voltages can be applied, thus avoiding these problems while maintaining high currents. To maximize **j** in systems involving redox species in solution, the chosen species should be highly electrochemically reversible and high in concentration. These high concentrations can be problematic in sensor applications. High concentrations of redox species can swamp electrochemical signals at the detector, overshadowing analyte response. They can also decrease the activity of enzymes and other biological agents which play a crucial role in immunoassay applications.

Recently, a new twist to microfluidic technique magnetohydrodynamics (MHD) involving redox-polymer modified electrodes has been used to minimize the risk of interference of the redox species with analysis methods. Previous MHD experiments in our lab electrodeposited poly(3,4-ethylenedioxythiophene), PEDOT onto gold microelectrodes from an aqueous solution containing 0.01 M of the monomer, 0.01 M of sodium dodecyl sulfate (SDS) and 0.1 M potassium chloride as electrolyte via cyclic voltammetry. These PEDOT films were found to be capable of generating high currents, and therefore, high fluid flow velocity, but deposition conditions were not optimized and the PEDOT films were only characterized electrochemically using chronoamperometry and cyclic voltammetry.

PEDOT is a conducting polymer which has multiple oxidation states and is electrochemically reversible. It also has interesting electrochromic characteristics, which change from dark blue to transparent based on its oxidation state. These properties have made PEDOT a material of interest to a wide range of applications including biosensors, electrochemical displays, solar cells, and batteries.[11-14] Each application has its own set of requirements for these PEDOT films. These properties can be tailored by careful adjustment of the deposition conditions. Since redox-MHD force is proportional to current, the electropolymerized PEDOT films should be capable of high currents and high coulombic capacity. The current response is determined by two film properties: 1) the film should be ordered so that electrons move quickly through the film to the electrode and 2) the film must be porous enough to allow for easy movement of ions in and out of the film. These properties can be controlled by the electrodeposition conditions under which the films are formed. Thicker films contain more redox centers and, therefore, higher coulombic capacity; however, depending on the resistance of movement of ions in and out of the films increases, causing a decrease in current. Thicker films can also have stability problems, resulting in delamination of the PEDOT film from the electrode surface. The choice of the counter ion during deposition has a major impact on the mechanical properties of the film.

Studies involving the electrodeposition of PEDOT have utilized a wide range of deposition conditions that affect the electrochemical properties and morphologies of the film.[14-35] These conditions include monomer concentration, electrochemical deposition method, the number of deposition coulombs, potential window, solubilizer, solvent, supporting electrolyte composition, and substrate material. For electrodeposition in aqueous, the choice of solubilizer has a profound impact on the oxidation potential of the monomer and the film morphologies. It has been observed in multiple studies that SDS decreases the oxidation potential of EDOT by approximately 100 mV, an effect that has been attributed to the negative charge of SDS stabilizing the oxidized monomer units ($EDOT^{\bullet+}$).[36-39] Similar effects has also been observed with sodium dodecylbenzene sulfonate, another anionic surfactant.[39] These films were found to have improved ion-transport and conductivity than films deposited in the presence of SDS.[32]

In 2012, Nasybulin et. al performed a systematic study on the effect of solubilizers on the properties of PEDOT films deposited from aqueous solution and tested their efficiency in a solar cell application.[31] Several solubilizers were examined including anionic solubilizing agents (sodium dodecyl

sulfate and sodium bis(2-ethylhexyl)sulfosuccinate), cationic solubilizing agents (hexadecyltrimethylammonium p-toluenesulfonate and hexadecyl(2-hydroxyethyl)dimethylammonium dihydrogen phosphate), neutral (Tween 80 and Triton X-100) and polyelectrolytes (sodium polystyrene sulfonate and κ-carrageenan). It was found that the type of solubilizing agent has a dramatic effect on oxidation potential of EDOT and the kinetics of polymerization and can affect the properties of the electrodeposited films. Nasybulin determined that anionic solubilizing agents lower the oxidation potential of EDOT because the negative charge stabilizes the oxidized monomer units ($EDOT^{\bullet+}$). Conversely, cationic surfactants increased the oxidation potential and slowed polymerization kinetics while neutral solubilizing agents had an intermediate effect.

This study examines the effect of four different solubilizers on film morphology and the electrochemical properties: sodium dodecyl sulfate (SDS), bis(2-ethylhexyl) sulfosuccinate (BEHS), 4-dodecylbenzene sulfonic acid (DBSA), and polystyrene sulfonate (PSS). Scanning electron microscopy shows the differences in morphology between the solubilizers. The electrochemical properties were assessed using cyclic voltammetry, chronoamperometry, and electrochemical impedance spectroscopy. The films displaying the highest current response and coulombic capacity were used to demonstrate improvements in redox-MHD pumping at PEDOT-modified microband electrodes.

4.3 Experimental Section

4.3.1 Chemicals and Materials. Aqueous solutions were made with reagent grade, 18 MΩ, deionized water from Ricca Chemical Company (Arlington, TX). Potassium ferricyanide was obtained from EM Science (Gibbstown, NJ) and used as received to characterize the microelectrodes prior to electrodeposition. The monomer of PEDOT, 3,4-ethylenedioxythiophene, was obtained from Sigma-Aldrich (Milwaukee, MN) and used as received without further purification. Sodium dodecyl sulfate, sodium polystyrene sulfonate (MW = 70,000), 4-dodecylbenzenesulfonic acid, and sodium bis(2-ethylhexyl) sulfosuccinate were obtained from Sigma Aldrich (Milwaukee, MN). Sodium chloride was obtained from EMD Chemicals Inc. (Gibbstown, NJ). The silicon wafers (125-mm diameter and 600-650-μm thick with 2 μm of thermally grown SiO_2 on the surface) used as substrate materials for the electrode arrays were purchased from Silicon Quest International (Santa Clara, CA). To fabricate the features of

the electrode arrays, a chromium-plated tungsten rod (Kurt J. Lesker Company, Clairton, PA) and a gold coin (Canadian Maple Leaf, 99.99%) were placed on molybdenum boats (Kurt J. Leskar Company, Pittsburg, PA) and used for metal deposition onto silicon wafers. Wafers were cleaned using Radio Corporation of America (RCA) procedure. Positive photoresist (AZ 4330) was used for the gold electrode pattern transfer from photo plot masks (Advance Reproductions Corporation, North Andover, MA) to the silicon wafer. To remove excess photoresist in the photolithography process, tetramethyl ammonium hydroxide (TMAH) solution was used as a developer. Gold etchant (Transene, GE8148) and chromium etchant (HTA enterprise, CEP200) were used as received. Benzocyclobutene, BCB, (Cyclotene 4024-40) purchased from Dow Corning Company (Midland, MI) was used to insulate the electrode leads. Edge connector (solder contact, 20/40 position, 0.05 in. pitch) purchased from Sullins Electronics Corp. (San Marcos, CA) was used to make electrical contact from the chip to the potentiostat. A poly(dimethyl siloxane), PDMS, gasket was fabricated using Sylgard184 silicon elastomer base and Sylgard 184 silicon elastomer curing agent (Ellsworth Adhesives, Milwaukee, WI). A silicon wafer was cleaned with OS-30 solvent (Ellsworth Adhesives, Milwaukee, WI) and was used as a substrate for spin-coated PDMS films. Pre-cleaned microscope glass slides (1.5 × 1.0 × 0.1 $in.^3$) were obtained from VWR. Polystyrene latex microspheres, 10.0 µm diameter (2.5 wt% dispersion in water) were purchased from Alfa Aesar (Ward Hill, MA).

4.3.2 Microelectrode Chips for Deposition Studies. The chips used in this study were 1 × 1 in. containing an array with two sets of 9 parallel individually addressable electrodes separated by a gap of 250 µm for a total of 18 electrodes. The microelectrodes were 97 µm wide × 252.2 µm long and were separated from electrodes within the set by 23 µm. Contact pads at the top of the chip were used to make contact between electrodes in the array region and the potentiostat with the use of an edge connector (See Figure 4.1).

4.3.3 Electrodeposition Experimental Setup. Four anionic solubilizer, which have been shown to lower the oxidation potential of EDOT, were used in this study to examine the effect of solubilizers on the electrochemical properties and morphologies of the PEDOT films. Aqueous solutions of 0.01 M EDOT and 0.01 M solubilizer, where the solubilizer was sodium dodecyl sulfate (SDS), sodium polystyrene sulfonate (PSS), 4-dodecylbenzenesulfonic acid (DBSA), or sodium bis(2-ethylhexyl)sulfosuccinate

(BEHS), were sonicated for at least two hours until all of the EDOT was dissolved. The structures and molecular weights for each of these solubilizer is shown in Figure 4.2. In addition, a deposition solution containing 0.010 M EDOT, 0.010 M SDS and 0.100 M KCl, which has been used in our group in the past to make a comparison to previous studies. PEDOT was electrodeposited onto the gold microelectrodes by submerging the chip in the solution of EDOT and cycling the electrodes between -0.455 V and 1.125 V at 0.05 $V \cdot s^{-1}$ for **N** number of cycles, where **N** = 1, 3, 6, 9, or 12 (Figure 4.3a). In the array region, every other electrode in a set was used for deposition and only one electrode was active at any given time so that the diffusion layer for the electrodes would not overlap. Each number of deposition cycles had two electrodes on opposite sides of the array, and two chips were used for each solubilizer, resulting in four replicates for each deposition condition. The chips were stored in a solution of 0.1 M NaCl for at least 24 hours before any characterization chronoamperometry (CA), and electrochemical impedance spectroscopy (EIS). A third chip was polymerized, left in deionized water for 48 hours, and dried in a desiccator for 1 week for scanning electron microscopy (SEM). All three chips polymerized for a given solubilizer were done simultaneously using CHI 760B, 750A, and 650A potentiostats to minimize time as a variable.

4.3.4 Scanning Electron Microscopy and Energy Dispersive X-ray Spectroscopy. A Philips XL-30 ESEM was used in secondary electrons mode to characterize the morphology of the PEDOT films prepared with different solubilizers. A FEI Nova Nanolab 200 SEM was used to perform energy dispersive x-ray spectroscopy (EDX) to determine the elemental composition of different morphology features. The gold microelectrodes were grounded to the sample holder to reduce charging current by placing conductive copper tape over the contact pads and over the bottom of the sample holder.

4.3.5 Electrochemical Characterization. Electrochemical characterization of PEDOT-modified electrodes were performed in 0.100 M NaCl. CV and CA were done using CHI 760B potentiostat. CV was performed on each modified electrode by cycling between -0.800 V to +0.800 V at 0.05 $V \cdot s^{-1}$ for 3 cycles. The counter electrode was a platinum flag electrode, and a Ag/AgCl in saturated KCl electrode was used as the reference electrode. For each solubilizer, the current at 0 V for a given number of deposition cycles was averaged and plotted versus the number of deposition cycles. The error bars shown represent the standard deviation in current for each point. A linear best fit line was also calculated.

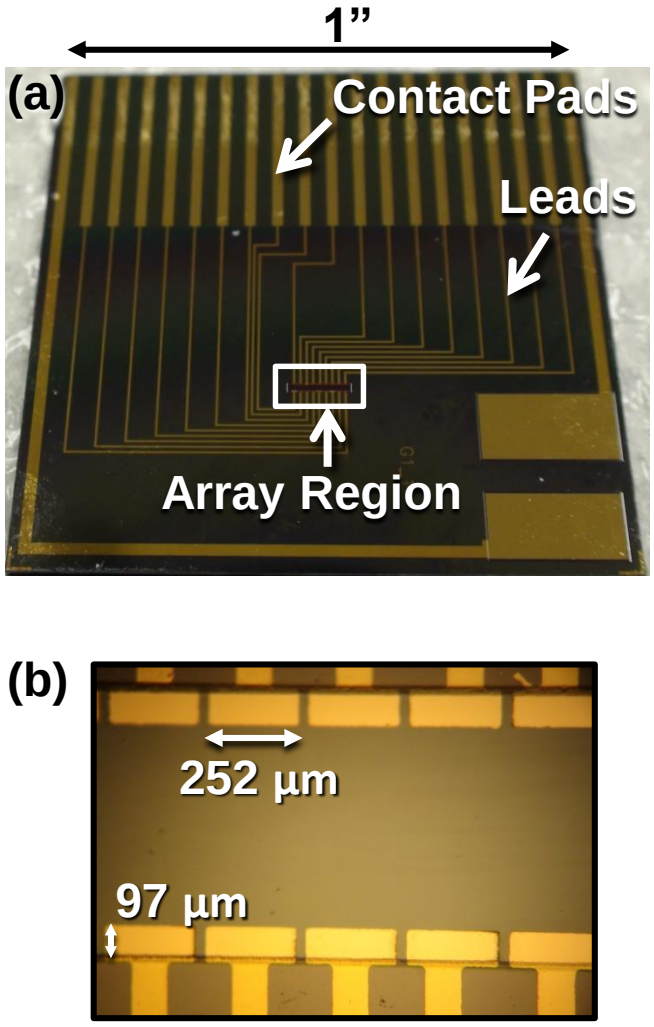

Figure 4.1 Electrode array chip used in deposition study. (a) Picture of electrode array chip containing 18 microelectrodes (97 × 252 µm) and two larger electrodes designed for on-chip auxiliary and references electrodes. (b) Enlarged picture taken with microscope of microelectrode array region.

(a)

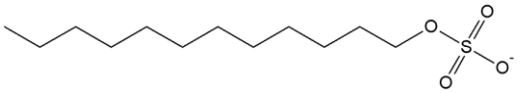

Dodecyl sulfate
MW = 288.38

(b)

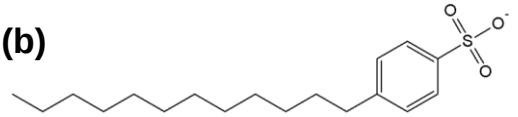

4-Dodecylbenzenesulphonic acid
MW = 326.49

(c)

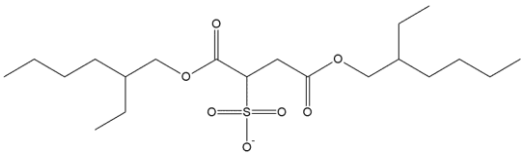

Bis(2-ethylhexyl)sulfosuccinate
MW = 444.56

(d)

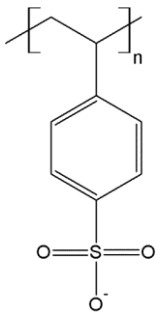

Polystyrene sulfonate
MW = 70,000

Figure 4.2 Structures and molecular weights of the different solubilizers investigated: (a) SDS (b) DBSA (c) BEHS (d) PSS.

CA was used to determine the number of coulombs available on the PEDOT-modified electrodes. The potential was stepped from -0.800 V (quiet time was 10 s) to +0.800 V and held for 20 s and the current over time was integrated to determine the number of coulombs available on the electrode. The number of coulombs was averaged for electrodes with the same solubilizer and number of deposition cycles and the standard deviation was calculated. The average number of coulombs versus the number of deposition cycles was plotted and a linear best fit line was calculated for each solubilizer.

Endurance studies were performed for one electrode modified with 12 deposition cycles for each deposition solution. The electrodes were cycled between -0.800 V and +0.800 V at 0.1 $V \cdot s^{-1}$ for 400 cycles in a solution of 0.100 M NaCl. The percentage of current lost was calculated by comparing the current at 0.00 V during the 1st cycle to the 400th cycle, according to the following equation:

$$Percent\ current\ lost\ = \frac{i_{3rd\ cycle} - i_{400th\ cycle}}{i_{3rd\ cycle}} * 100$$

This study was done for films deposited from each of the different deposition solutions and the results were compared.

EIS studies were performed using a PARSTAT MC (from AMETEK in Oak Ridge, TN) applying an excitation perturbation amplitude of 10 mV root mean square (RMS). Measurements were carried out over a frequency range of 1 Hz to 10^5 Hz with 10 points per decade. A measurement delay of 30 s was used before each point was taken. VersaStudio V2.40.4 (© 2013) software was used to record and ZSimpWin™ version 3.50 was used to model the impedance data.

4.3.6 Redox-MHD at PEDOT-modified Electrodes. In order to assess the effectiveness of the PEDOT films deposited under these deposition conditions, redox-MHD experiments at PEDOT-modified microband electrodes were performed. The silicon chip design chosen for this work has been used extensively in our lab for MHD experiments and contains three sets of four microband electrodes measuring 100 µm wide by 2.5 cm long (Figure 4.S1a). The films deposited in 0.01 M EDOT and 0.01 M SDS with 12 deposition cycles were chosen because those films were the most reproducible and capable of the highest number of coulombs (BEHS had the highest number of coulombs, but had the highest error between films). For redox-MHD pumping, four PEDOT-modified microband electrodes (shorted together using the edge connector) served as the working electrode and the remaining eight microband electrodes

served as the counter and quasi-reference electrodes. A 0.37 T NdBFe magnet (diameter of 1.5 in. and height of 0.5 in., Amazing Magnets LLC, Irvine, CA) was placed under the chip to generate a magnetic field perpendicular to the chip surface. A 620 µm PDMS gasket (measured when dry) with an opening of 1.5 cm × 3.2 cm was placed on top of the chip to hold 325 µL of solution of 0.095 M NaCl containing 10 µm polystyrene beads (Figure 4.S1b).

Fluid flow was visualized using a Nikon microscope interfaced with a Sony Handycam video camera (30 frames per second). The focal plane was adjusted using the height of the microscope stage and beads within ±75 µm of 300 µm above the chip were analyzed. The bead movement during applied potential experiments was quantified using particle tracking software (World-In-Motion Physics Toolkit software (WIM, www.physicstoolkit.com)). WIM tracks the displacement of individual beads through subsequent frames captured from the video and divides by the time (from the time stamp of the video) to calculate the instantaneous bead speed. WIM can, therefore, have time resolution as high as the video recorded which is needed to assess the highly transient velocities during an applied potential experiment. For the applied potential experiments, a quiet time where the potential was held at -0.3 V for 10 s was applied to reduce the PEDOT film, followed by an applied potential of +1.00 V for 5 s. The instantaneous speeds of four individual beads were averaged and standard deviation was calculated.

For applied current experiments, bead movement was quantified using particle imaging velocimetry (PIV) analysis software (Dynamic Studios). PIV breaks the video into interrogation regions and tracks the movement of bead patterns through subsequent frames. The displacement of the beads over time is used to calculate an average velocity vector for each interrogation region. The scale for both WIM and PIV analyses was measured manually using the dimensions of known features on the chip. Fluid flow was examined at applied anodic currents of -100 µA and -500 µA.

4.4 Results and Discussion

4.4.1 Effect of Anionic Surfactants on Oxidation Potential of EDOT. As discussed earlier, the nature of the solubilizer has a profound effect on the polymerization of EDOT. It is known that the presence of anionic surfactants decreases the oxidation potential of the monomer by stabilizing the oxidized monomer units ($EDOT^{\bullet+}$) and the growing macromolecular chain until it deposits on the

electrode surface. It was also observed by Nasybulin et al that the oxidation potential of EDOT increases with the size of the solubilizer and that the polymerization kinetics slow with increasing bulkiness of the anionic solubilizer.[31] Figure 4.3b shows the first cyclic voltammogram from electropolymerization of EDOT in the presence of different anionic surfactants. The oxidation potential of EDOT increases with the size of the anionic surfactant (SDS<DBSA<BEHS<PSS), which is in agreement with results published by Nasybulin et al. Figure 4.3c shows a cyclic voltammogram during deposition of PEDOT in the presence of SDS for 12 deposition cycles. For each subsequent cycle, the peak for the oxidation of the monomer increases, indicating an increase in surface area of the electrode resulting from deposition of PEDOT.

4.4.2 PEDOT Film Morphology by SEM. SEM was used to capture the morphology of PEDOT films polymerized in the presence of different solubilizers and for different number of deposition cycles. The choice of solubilizer has a large impact on the morphology of the film. As PEDOT is being deposited on the electrode surface, counter-ions must come into the film to compensate for the change in charge. The positive charge of the oxidized PEDOT film means that the bulky anions of the solubilizer get incorporated into the film during deposition. Figure 4.4 shows SEM images of PEDOT films deposited using 12 deposition cycles in the presence of 4 different solubilizers. The SEM image of PEDOT deposited in the presence of SDS reveals long mounds of PEDOT measuring approximately 5 µm in width and ranging from 10 to 20 µm in length and needle-like structures measuring 1 µm in width and 30 to 40 µm in length (Figure 4.4a). EDX confirmed that both the mounds and the fibers were composed of PEDOT (Figure 4.S2 and 4.S3). Between the mounds are deep crevices down to the more compact portion of the film that was described above, which could help in more facile incorporation of counter-ions into the film during oxidation. Films deposited in a solution of SDS and 0.1 M KCl were denser than those without KCl (Figure 4.4e). The image of PEDOT film deposited in the presence of DBSA (Figure 4.4b) show clumps ranging from 5 to 10 µm in diameter and is the most compact out of the surfactants (SDS, DBSA, and BEHS). The SEM image of PEDOT films deposited in the presence of BEHS show clumps between 5 to 10 µm in diameter with a cauliflower-like structure (Figure 4.4c). The PEDOT deposited in the presence of PSS has the most unique morphology of the solubilizers examined in this study (Figure 4.4d). These films were significantly thinner than the others and featured smooth, compact films with

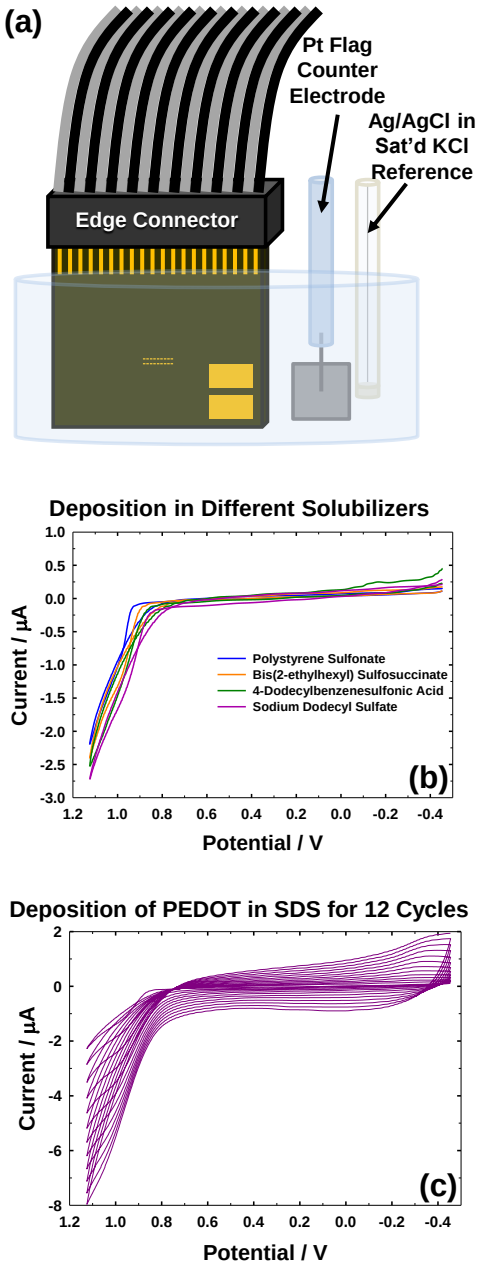

Figure 4.3 Electrodeposition of PEDOT. (a) Illustration of experimental setup of electrodeposition of PEDOT onto gold microelectrodes. (b) Overlay of first deposition cycles for each of the different solubilizers. (c) CV of electrodeposition of PEDOT in a solution of 0.01 M EDOT and 0.01 M SDS using 12 deposition cycles.

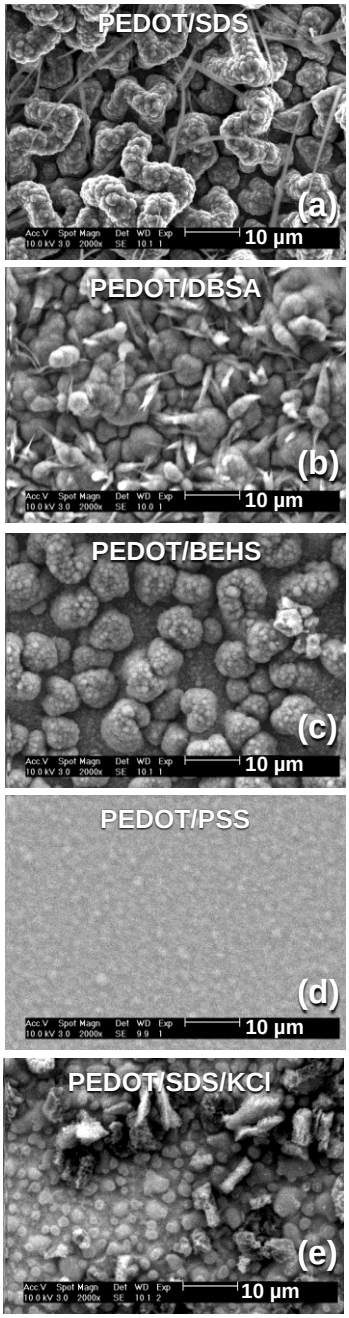

Figure 4.4 SEM images at 2000× magnification for each of the electrodeposition solutions: (a) PEDOT/SDS (b) PEDOT/DBSA (c) PEDOT/BEHS (d) PEDOT/PSS (e) PEDOT/SDS/ KCl

small bumps measuring between 2 and 3 μm in diameter. This film was much more uniform than those produced with the other solubilizers.

It should be noted that these SEM images were taken in the center of the electrode where the morphology was the most uniform. Edge-effects were observed where the film on the edge of the electrode was much thicker than in the center of the electrode for all of the deposition conditions. This is due to radial diffusion which contributes only occurs at the edge of the electrode in addition to the planar diffusion which occurs over the entire electrode area.

4.4.3 Relationship between number of deposition cycles and the number of active coulombs in PEDOT film. Ideally, for PEDOT-modified electrodes to be useful in redox-MHD microfluidic settings, the film should have as many active redox centers as possible in order to pump in a single direction for the greatest amount of time. These studies show a linear dependence on active coulombs in the PEDOT film with the number of deposition cycles as expected. Plots of active coulombs versus the number of deposition cycles for each of the different solubilizers and their R^2 value of each curve are included in the supplemental section (Figure 4.S4). The best fit equations can be seen in Table 1. Of these plots, SDS and BEHS have the highest slopes (and are within error of each other) indicating that the most active redox centers are deposited per deposition cycle. BEHS, however, has the largest error bars and therefore, the greatest variability between replicates. Films deposited in the presence of DBSA or PSS had a lower deposition rate per cycle. These results are summarized in Table 1. The PEDOT films polymerized in SDS and KCl grew at a slower rate, generating films with much lower currents and coulombic capacity.

4.4.4 EIS Characterization of PEDOT-modified Electrodes. EIS is widely used to assess the electrochemical characteristics of conducting polymer films, allowing the investigation of mass and charge transport kinetics and charging processes involved in the films. These kinetics can be modelled with the use of circuit elements such as resistors and capacitors. A number of studies has indicated that charge transport within conducting polymer films is depend greatly on the morphology and surface roughness of the film. Circuit models developed to describe charge transport in conducting polymer are based on the influential electrochemical processes: charge transfer at the metal-polymer interface, charge transfer with the conducting polymer film, and charge transfer at the polymer-solution interface.[40-42] Each of these

processes is described by a type of circuit element where the contribution of each can be separately determined. However, it should be noted that most equivalent circuit models for impedance provide little or no direct information about the physical processes taking place.

From the SEM images of the PEDOT films deposited with an increasing number of cycles it is evident that these films are inhomogeneous where the first layer deposited is smooth and compact and the outer layers are increasing rough, creating pores filled with electrolyte. Films like this have been shown to have non-linear diffusional behavior due to ionic charge adsorption within the film, charge trapping, and non-uniform thickness.[43-46] Typically, constant phase elements (CPEs) are used as shortcuts to explain inconsistent behavior and deviations from theoretical predictions. The addition of CPEs, however, can make it more difficult to tease out the microscopic physical meaning from the model.

4.4.5 Circuit Modeling of EIS Data. Figure 4.5a shows an overlay of nyquist plots for PEDOT films deposited in 12 cycles from each of the different monomer solutions. Figure 4.5b shows an enlarged graph of the data taken at higher frequencies. Each of these Nyquist plots has a small kinetics-governed region at high frequencies where a piece of a semi-circle is evident, a diffusion-governed Warburg element at intermediate frequencies, and a dominant capacitive region at low frequencies. A new collaboration with Dr. Faye Rubinson at Georgetown University will hopefully result in a unified circuit model that is able to fit all of the films with simple adjustments of element values. Their group has been able to model PEDOT films using a hybrid between an intercalation model to represent the compact layers and a transmission line model to represent the porous region.[40, 47] This should be a sufficient model for our PEDOT films to explain the charge transport in the porous regions of the film.

4.4.6 Information from the Bode Plot. At low frequencies, the total impedance is lowest for the PEDOT/SDS film, indicating a combination of higher conductivity and greater surface area (this is also supported by the SEM images), which would be advantageous for redox-MHD applications. The Bode plot also shows similar ohmic resistance (as evident through the z-values) for PEDOT/SDS, PEDOT/BEHS, and PEDOT/PSS from 10^2 to 10^5 Hz (Figure 4.5c). The EIS data for PEDOT/DBSA is significantly different from the rest of the PEDOT films, indicating a different charge and mass transfer process. From the SEM images of PEDOT/DBSA, it makes sense that the mass and charge transport would be different compared to the other anionic surfactant. The SEM images of PEDOT/DBSA of

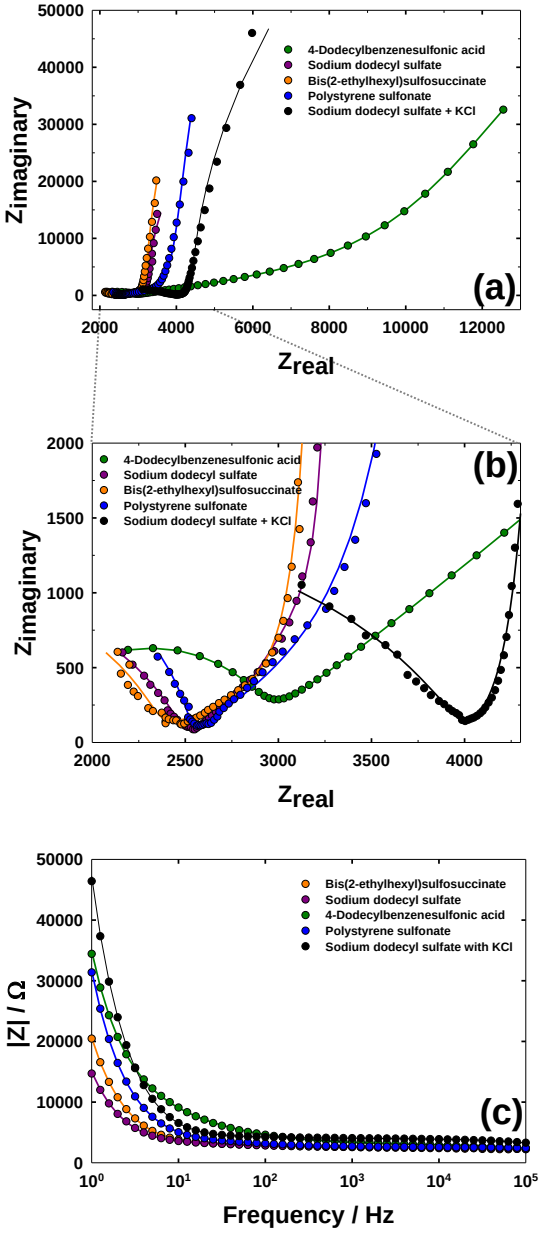

Figure 4.5 EIS data for films generated with 12 deposition cycles for each of the electrodeposition solutions. (a) Nyquist plot. (b) Enlarged Nyquist plot showing the kinetically controlled portion of the graph. (c) Bode plot.

different thicknesses (Figure 4.S8) reveal a more compact film with large clumps separated by small crevices which would increase the ionic resistance of the film. For all of these films, the phase angle at 10^5 Hz is close to 15°, which indicates that at these frequencies, the impedance is predominately resistive rather than capacitive.

4.4.7 Thickness Study. Panels a-e of Figure 4.6 show PEDOT modified electrodes which were electrodeposited in the presence of SDS under an increasing number of deposition cycles. For only a single deposition cycle, the film is very compact and smooth, following the any scratches in the bare gold surface. After 3 deposition cycles, small bumps between 2 and 5 μm in diameter begin to form on top of the compact film formed in the first two deposition cycles. As the number of deposition cycles increases, the surface roughness and porosity increases. This observation is in agreement with the growth model proposed by Randriamahazaka et al. which proposes a combination of instantaneous 2-D and 3-D growth mechanism where 2-D growth initially dominates followed by a layer-by-layer growth mechanism as the deposition time increases.[17] Figures 4.S5 and 4.S6 shows the SEM images for all of the monomer-containing deposition solutions explored in this study at different numbers of deposition cycles. All of the anionic surfactants (SDS, BEHS, and DBSA) begin with compact films that explode into 3-dimensional clumps and pores. As expected, EIS analysis show that the total impedance for PEDOT/SDS films decreases with increasing number of cycles, indicating an increase in surface area and conductivity (Figure 4.7). Also, the films exhibit kinetic and diffusion-controlled behavior at lower frequencies with increasing thickness. The thinner films exhibit capacitive behavior at most frequencies.

4.4.8 Electrochemical Endurance Studies. In order to function well in a microfluidic device, PEDOT films should be capable of enduring several charging and discharging processes. This greatly depends on the mechanical properties of the film. To assess the stability of these films, endurance studies were performed on electrodes modified with 12 deposition cycles by cycling between -0.8 V and 0.8 V 400 times. The percent loss of current between the 1^{st} cycle and the 400^{th} cycle was calculated. Interestingly, PEDOT/BEHS films exhibited the best electrochemical stability with only a 24% loss of current over 400 cycles, despite its increased variability between films (as compared to other solubilizers). The choice of solubilizer has an effect on the electrochemical endurance of the electrodeposited film.

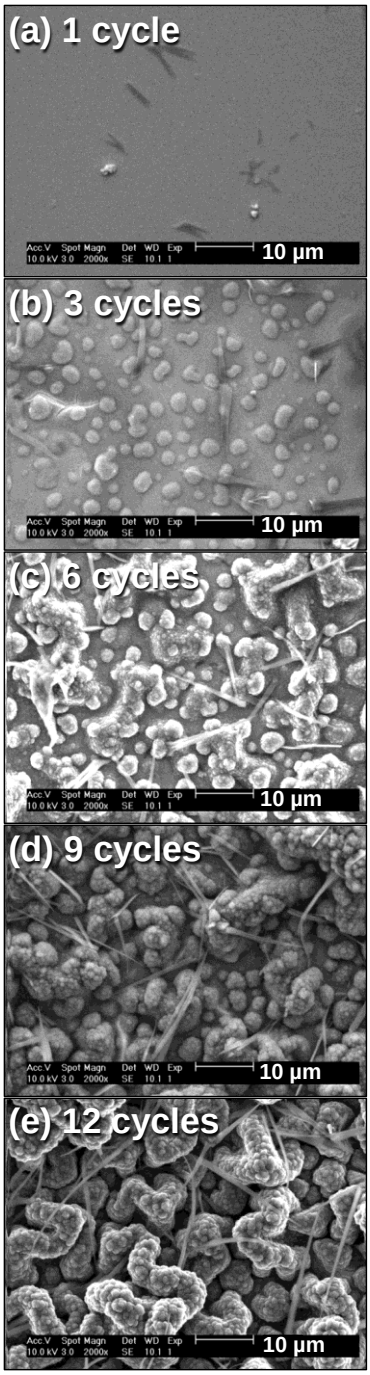

Figure 4.6. SEM images of PEDOT/SDS films of increasing film thickness: (a) 1 deposition cycle (b) 3 deposition cycles (c) 6 deposition cycles (d) 9 deposition cycles (e) 12 deposition cycles.

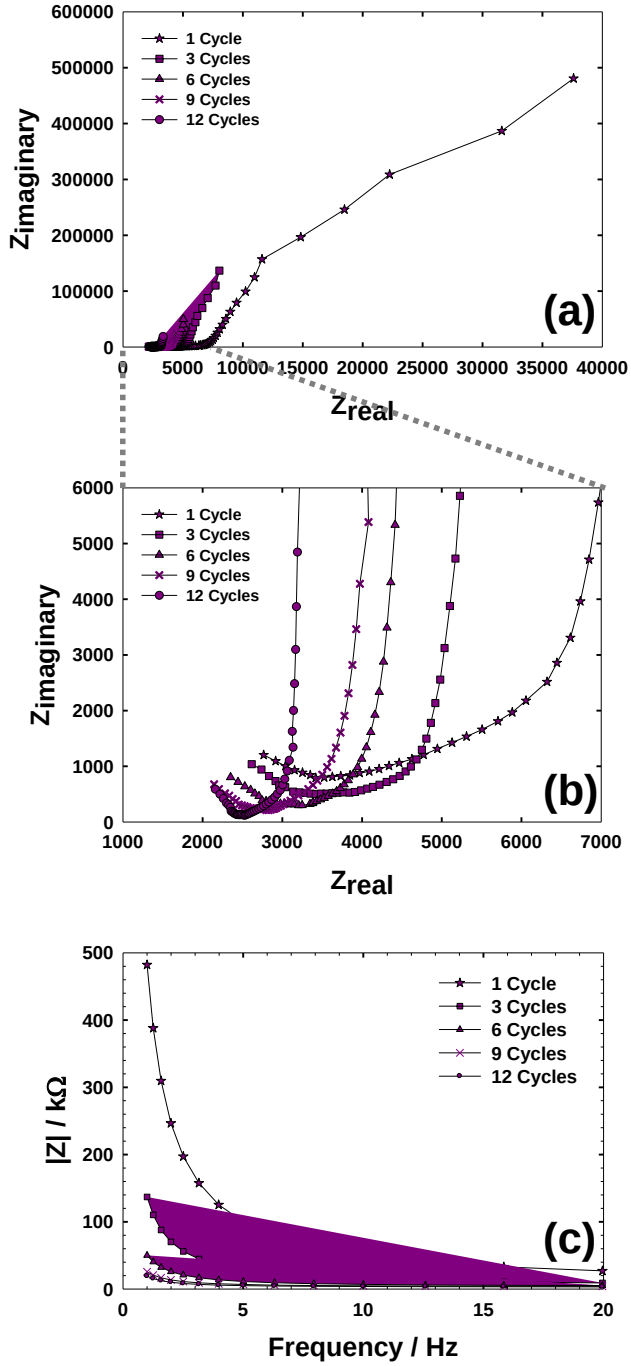

Figure 4.7 EIS data for PEDOT/SDS films generated with a varying number of deposition cycles (1, 3, 6, 9, 12 cycles). (a) Nyquist plot. (b) Enlarged Nyquist plot showing the kinetically controlled portion of the graph. (c) Bode plot.

PEDOT/SDS and PEDOT/DBSA had a 34% loss in current and PEDOT/PSS had a 41% loss in current after 400 cycles. PEDOT films polymerized in SDS and KCl suffered a 33 % loss of current. Figure 4.S7 shows cyclic voltammetry of PEDOT-modified electrodes in 0.1 M NaCl during the 1st cycle and the 400th cycle. These results are summarized in Table 1.

4.4.9 DC-MHD at PEDOT-modified Electrodes. The inspiration for this work was to improve the coulombic capacity and current time response of PEDOT-modified electrodes to improve their performance in redox-MHD applications (Figure 4.8a). Figure 4.S1 shows the silicon chip and the experimental setup for the video microscopy used for redox-MHD experiments. For these experiments, the electrodes were modified using SDS as the surfactant because these films exhibited the best overall coulombs, time response, and consistency between electrodes. The flow velocity during applied potential experiments tracked the current response, where the velocity was initially as high as 1020 $\mu m \cdot s^{-1}$, and decreased drastically with time (Figure 4.8b). This maximum velocity is higher than PEDOT-modified electrodes in identical chip designs that have been previously reported, which were deposited in a solution containing 0.01 M EDOT, 0.01 M SDS and 0.1 M KCl at slower deposition scan rates (5 $mV \cdot s^{-1}$). This is due to the increase in maximum current and in the number of active coulombs available within the PEDOT film. Figure 4.S8 in the supplemental section shows an overlay of the current responses during CV and CA experiments of films deposited in the presence and absence of KCl, which shows the electrochemical improvement.

Using applied current, the fluid velocity can be fine-tuned for the specific needs of an application, and redox-MHD convection can be sustained for longer times depending on the magnitude of the current applied and on the coulombic capacity of the film. These films exhibit a similar linear relationship between applied current and fluid velocity, which matches with the relationship established previously in our group. Impressively, these films can handle higher applied currents and can sustain pumping for longer times due to the improved coulombic capacity. An applied anodic current of 100 µA generated velocities of 49.55 ± 1.64 µm·s-1 in the middle of the 5600 µm gap between the working and auxiliary/quasi-reference microband electrodes (Figure 4.8c). Applying an anodic current of 500 µA achieved velocities of 268 ± 3.31 µm·s-1 (Figure 4.8d).

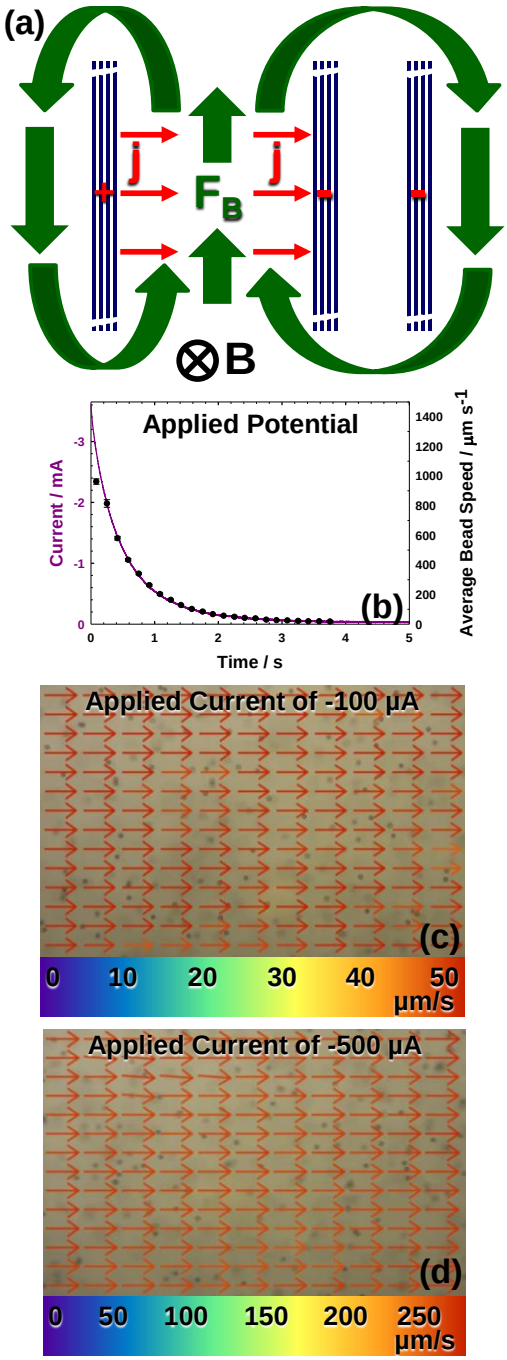

Figure 4.8 (a) Illustration of Redox-MHD fluid flow around PEDOT-modified microband electrodes. (b) Overlay of current response and average bead speed during a potential step MHD experiment. (c) PIV analysis of bead movement in the middle of the 5600 µm gap between the working and auxiliary/quasi-reference electrodes during an applied anodic current experiment of 100 µA. (d) PIV analysis of bead movement in the middle of the 5600 µm gap between the working and auxiliary/quasi-reference electrodes during an applied anodic current experiment of 500 µA.

4.5 Conclusions

By focusing on the electrochemistry at the electrodes, the performance of PEDOT-modified electrodes for redox-MHD pumping was improved. Thick films were successfully deposited using four different solubilizers, which produced unique morpholgies and electrochemical properties. Film morphology plays a crucial role in the performance of these films and should be considered against the requirements for the application. The films were characterized and modeled using EIS. This should improve future models to predict the charge transfer within the film and the ionic current density distribution throughout the cell. Future work will focus on electronic methods of sustaining microfluidic pumping utilizing the improved deposition conditions explored in this work.

4.6 Acknowledgements

Research was supported through the National Science Foundation (NSF) (CHE-0719097) and the Arkansas Biosciences Institute, the major research component of the Arkansas Tobacco Settlement Proceeds Act of 2000. The authors greatly appreciate the use of the Arkansas Nano & Bio Materials Characterization Facility for the SEM studies.

4.7 Abbreviations

MHD, magnetohydrodynamics; PEDOT, poly(3,4-ethylenedioxythiophene); SDS, sodium dodecyl sulfate; BEHS, bis(2-ethylhexyl)sulfosuccinate; DBSA, 4-dodecylbenzene sulfonic acid; PSS, polystyrene sulfonate; CV, cyclic voltammetry; CA, chronoamperometry; CP, chronopotentiometry.

Notes

The authors declare the following competing financial interest(s): The author has declared a potential conflict of interest due to her equity stake of >5% in SFC Fluidics, LLC. Dr. Fritsch created intellectual property on redox-MHD which is licensed to SFC Fluidics

4.8 References

(1) Weston, M. C.; Gerner, M. D.; Fritsch, I. *Analytical Chemistry* **2010**, *82*, 3411-3418.

(2) Qian, S.; Bau, H. H. *Mechanics Research Communications* **2009**, *36*, 10-21.

(3) Leventis, N.; Gao, X. *The Journal of Physical Chemistry B* **1999**, *103*, 5832-5840.

(4) Leventis, N. *J. Phys. Chem. B* **1998**, *102*, 3512-3522.

(5) Ragsdale, S. R.; Lee, J.; White, H. S. *Analytical chemistry* **1997**, *69*, 2070-2076.

(6) Bau, H. H.; Zhu, J.; Qian, S.; Xiang, Y. *Sensors and Actuators B: Chemical* **2003**, *88*, 205-216.

(7) Zhong, J.; Yi, M.; Bau, H. H. *Sensors and Actuators A: Physical* **2002**, *96*, 59-66.

(8) Pamme, N. *Lab on a Chip* **2006**, *6*, 24-38.

(9) Jang, J.; Lee, S. 1998; 15-20.

(10) Jang, J.; Lee, S. S. *Sensors and Actuators A: Physical* **2000**, *80*, 84-89.

(11) Groenendaal, L.; Zotti, G.; Aubert, P. H.; Waybright, S. M.; Reynolds, J. R. *Advanced Materials* **2003**, *15*, 855-879.

(12) Groenendaal, L.; Jonas, F.; Freitag, D.; Pielartzik, H.; Reynolds, J. R. *Advanced Materials* **2000**, *12*, 481-494.

(13) Fabiano, S.; Tran-Minh, C.; Piro, B. Ì. t.; Dang, L. A.; Pham, M. C.; Vittori, O. *Materials Science and Engineering: C* **2002**, *21*, 61-67.

(14) Wang, X.; Sjoberg-Eerola, P.; Eriksson, J.-E.; Bobacka, J.; Bergelin, M. *Synthetic Metals* **2010**, *160*, 1373-1381.

(15) Sakmeche, N.; Aeiyach, S.; Aaron, J.-J.; Jouini, M.; Lacroix, J. C.; Lacaze, P.-C. *Langmuir* **1999**, *15*, 2566-2574.

(16) Poverenov, E.; Li, M.; Bitler, A.; Bendikov, M. *Chemistry of Materials* **2010**, *22*, 4019-4025.

(17) Randriamahazaka, H.; Noel, V.; Chevrot, C. *Journal of Electroanalytical Chemistry* **1999**, *472*, 103-111.

(18) Wen, Y.; Xu, J.; He, H.; Lu, B.; Li, Y.; Dong, B. *Journal of Electroanalytical Chemistry* **2009**, *634*, 49-58.

(19) Bobacka, J.; Lewenstam, A.; Ivaska, A. *Journal of Electroanalytical Chemistry* **2001**, *509*, 27-30.

(20) Colleran, J. J.; Breslin, C. B. *Journal of Electroanalytical Chemistry* **2012**, *667*, 30-37.

(21) Kayinamura, Y. P.; Roberts, J. H.; Rubinson, J. F. *ACS applied materials & interfaces* **2012**, *4*, 1601-1607.

(22) Bello, A.; Giannetto, M.; Mori, G.; Seeber, R.; Terzi, F.; Zanardi, C. *Sensors and Actuators B: Chemical* **2007**, *121*, 430-435.

(23) Richardson-Burns, S. M.; Hendricks, J. L.; Foster, B.; Povlich, L. K.; Kim, D.-H.; Martin, D. C. *Biomaterials* **2007**, *28*, 1539-1552.

(24) Ludwig, K. A.; Uram, J. D.; Yang, J.; Martin, D. C.; Kipke, D. R. *Journal of neural engineering* **2006**, *3*, 59.

(25) Xiao, Y.; Cui, X.; Martin, D. C. *Journal of Electroanalytical Chemistry* **2004**, *573*, 43-48.

(26) Cui, X.; Martin, D. C. *Sensors and Actuators B: Chemical* **2003**, *89*, 92-102.

(27) Piro, B. Ì. t.; Dang, L. A.; Pham, M. C.; Fabiano, S.; Tran-Minh, C. *Journal of Electroanalytical Chemistry* **2001**, *512*, 101-109.

(28) Xiao, Y. H.; Li, C. M.; Toh, M. L.; Xue, R. *Journal of applied electrochemistry* **2008**, *38*, 1735-1741.

(29) Sekli-Belaidi, F.; Temple-Boyer, P.; Gros, P. *Journal of Electroanalytical Chemistry* **2010**, *647*, 159-168.

(30) Kumar, S.; Mathiyarasu, J.; Phani, K.; Yegnaraman, V. *Journal of Solid State Electrochemistry* **2006**, *10*, 905-913.

(31) Nasybulin, E.; Wei, S.; Kymissis, I.; Levon, K. *Electrochimica Acta* **2012**, *78*, 638-643.

(32) Cho, S. H.; Lee, H. J.; Ko, Y.; Park, S.-M. *The Journal of Physical Chemistry C* **2011**, *115*, 6545-6553.

(33) Hass, R.; García-Cañadas, J.; Garcia-Belmonte, G. *Journal of Electroanalytical Chemistry* **2005**, *577*, 99-105.

(34) Bobacka, J.; Lewenstam, A.; Ivaska, A. *Journal of Electroanalytical Chemistry* **2000**, *489*, 17-27.

(35) Snook, G. A.; Peng, C.; Fray, D. J.; Chen, G. Z. *Electrochemistry communications* **2007**, *9*, 83-88.

(36) Sakmeche, N.; Aeiyach, S.; Aaron, J.-J.; Jouini, M.; Lacroix, J. C.; Lacaze, P.-C. *Langmuir* **1999**, *15*, 2566-2574.

(37) Sakmeche, N.; Bazzaoui, E. A.; Fall, M.; Aeiyach, S.; Jouini, M.; Lacroix, J. C.; Aaron, J. J.; Lacaze, P. C. *Synthetic Metals* **1997**, *84*, 191-192.

(38) El Moustafid, T.; Gregory, R. V.; Brenneman, K. R.; Lessner, P. M. *Synthetic metals* **2003**, *135*, 435-436.

(39) Zhang, S.; Hou, J.; Zhang, R.; Xu, J.; Nie, G.; Pu, S. *European polymer journal* **2006**, *42*, 149-160.

(40) Rubinson, J. F.; Kayinamura, Y. P. *Chemical Society Reviews* **2009**, *38*, 3339-3347.

(41) Cui, X.; Hetke, J. F.; Wiler, J. A.; Anderson, D. J.; Martin, D. C. *Sensors and Actuators A: Physical* **2001**, *93*, 8-18.

(42) Nguyen, T.-Q.; Kwong, R. C.; Thompson, M. E.; Schwartz, B. J. *Applied Physics Letters* **2000**, *76*, 2454-2456.

(43) Tanguy, J.; Mermilliod, N.; Hoclet, M. *Journal of the Electrochemical Society* **1987**, *134*, 795-802.

(44) Chapman, B.; Buckley, R. G.; Kemp, N. T.; Kaiser, A. B.; Beaglehole, D.; Trodahl, H. J. *Physical Review B* **1999**, *60*, 13479.

(45) Lang, G.; Inzelt, G. *Electrochimica acta* **1991**, *36*, 847-854.

(46) Bobacka, J.; Grzeszczuk, M.; Ivaska, A. *Electrochimica acta* **1992**, *37*, 1759-1765.

(47) Kayinamura, Y. P.; Ovadia, M.; Zavitz, D.; Rubinson, J. F. *ACS applied materials & interfaces* **2010**, *2*, 2653-2662.

Table 4.1

Solubilizer	E_{ox} of EDOT (V)	Best Fit Line for Coulombs in Film vs Deposition Cycle	Coulombs/ area (mC/cm^2)	Current Density (mA/cm^2)	Time Constant (s)	% Current Lost
SDS	0.74	$C = (2.63 \pm 0.285\ \mu C \cdot n^{-1})N - 3.53 \pm 2.10\ \mu C$	119.88	1228	7.600×10^{-2}	34
PSS	0.85	$C = (1.16 \pm 0.0769\ \mu C \cdot n^{-1})N - 0.572 \pm 0.566\ \mu C$	55.38	1380	3.500×10^{-2}	41
BEHS	0.8	$C = (2.65 \pm 0.119\ \mu C \cdot n^{-1})N + 0.500 \pm 0.877\ \mu C$	132.70	1140	6.700×10^{-2}	24
DBSA	0.76	$C = (1.32 \pm 0.0494\ \mu C \cdot n^{-1})N - 0.232 \pm 0.364\ \mu C$	63.40	1148	4.200×10^{-2}	34
SDS + KCl	0.87	$C = (0.735 \pm 0.0149\ \mu C \cdot n^{-1})N - 0.492 \pm 0.110\ \mu C$	24.34	648	5.300×10^{-2}	33

4.S Fine-tuning Properties of Electrodeposited PEDOT films for Redox-Magnetohydrodynamic Microfluidic Applications Via Manipulation of Electrodeposition Conditions

4.S1 Supporting Information

A picture of the microfluidic chip used for redox-MHD is included, and the video microscopy experimental setup is illustrated. SEM images for all of the deposition conditions including different solubilizers and number of deposition cycles are available in the supplemental section, which show how the film morphology changes with increasing thickness. EDX analysis for the cauliflower structure and needle-like structure of the PEDOT/SDS produced after 12 deposition cycles. Overlay of current response during CV and CA for PEDOT/SDS films deposited in the presence and absence of KCl is shown to compare the new films to films produced in our lab in the past. Plots of average coulombs in the film vs deposition cycles as well as endurance studies for each of the different deposition solutions is included here.

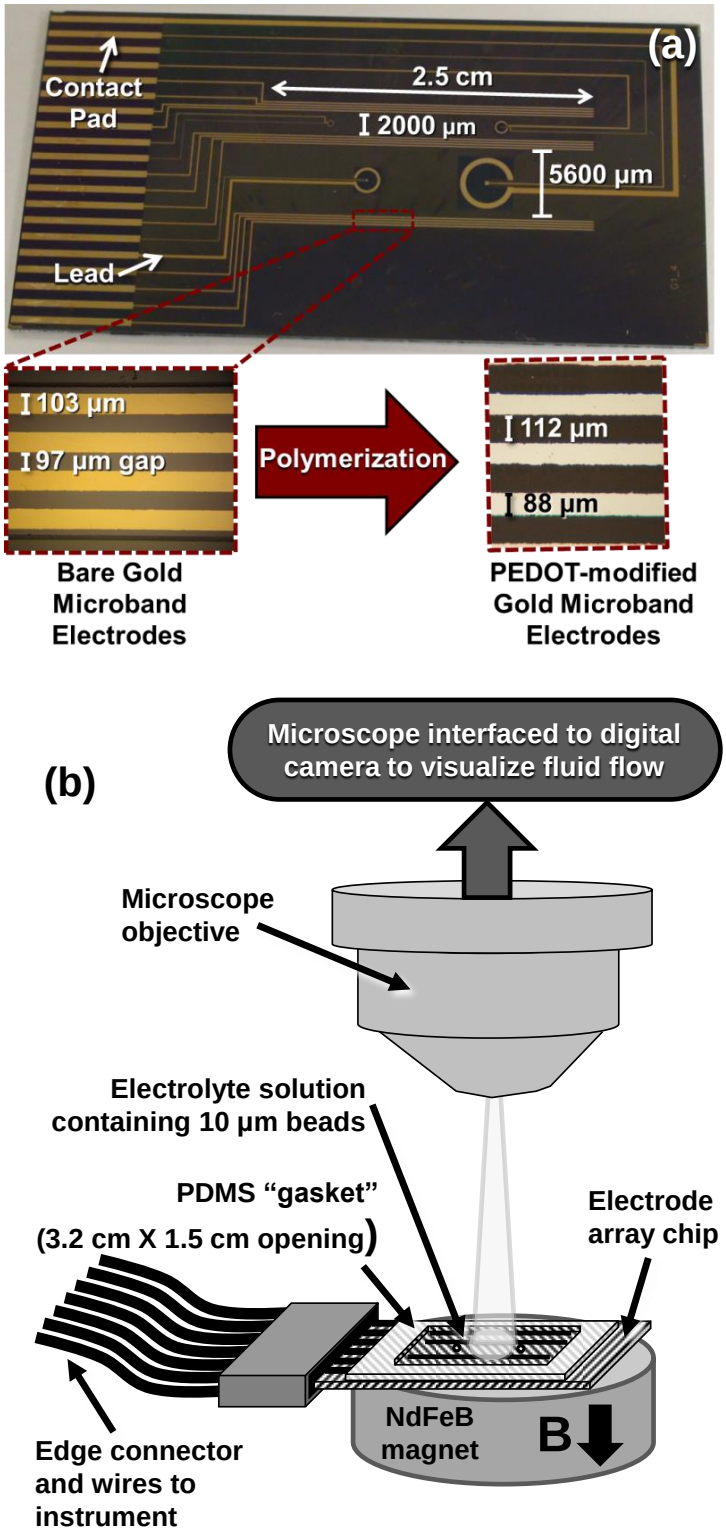

Figure 4.S1. (a) Photograph of chip used in the redox-MHD experiments. The enlarged portion shows bare microband electrodes and PEDOT-modified microband electrodes under a microscope. (b) Experimental setup for visualizing fluid flow.

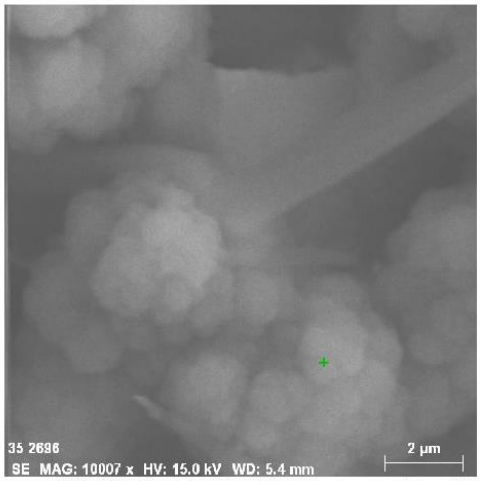

35 2696Date:6/9/2014 10:22:16 AMImage size:512 x 512Mag:10007.3435032439xHV:15.0kV

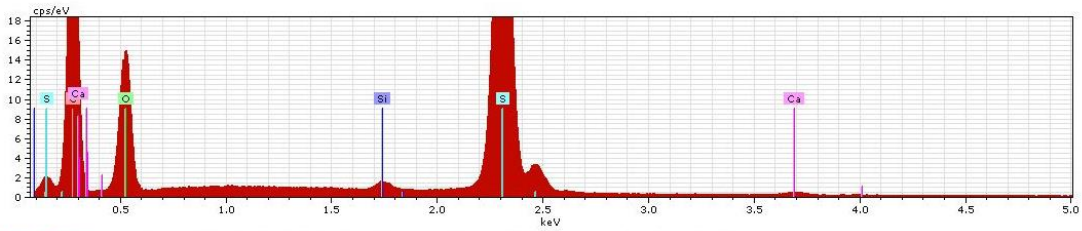

Acquisition Date:6/9/2014 10:22:21 AM HV:15.0kV Puls th.:10.41kcps

El	AN	Series	unn. C [wt.%]	norm. C [wt.%]	Atom. C [at.%]	Error [wt.%]
C	6	K-series	66.79	59.28	71.00	7.4
O	8	K-series	26.85	23.83	21.43	3.1
Si	14	K-series	0.39	0.34	0.18	0.0
S	16	K-series	18.25	16.20	7.27	0.7
Ca	20	K-series	0.39	0.34	0.12	0.0
		Total:	112.67	100.00	100.00	

Figure 4.S2. SEM of PEDOT/SDS at 10007× magnification and EDX spectrum of the cauliflower structure of PEDOT/SDS.

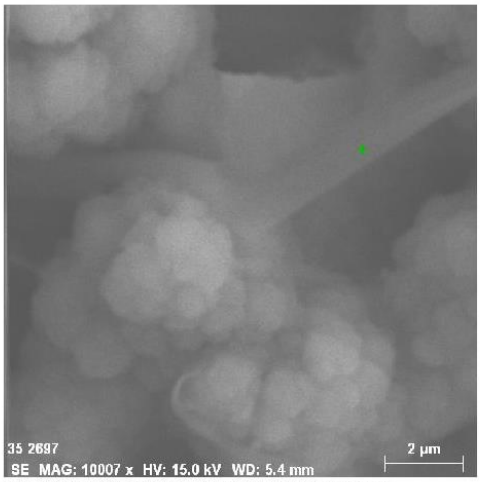

35 2697Date:6/9/2014 10:23:46 AMImage size:512 x 512Mag:10007.3435032439xHV:15.0kV

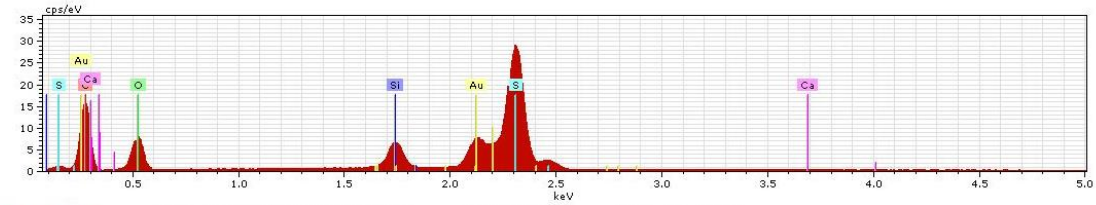

Acquisition Date:6/9/2014 10:24:00 AM HV:15.0kV Puls th.:9.32kcps

El	AN	Series	unn. C [wt.%]	norm. C [wt.%]	Atom. C [at.%]	Error [wt.%]
C	6	K-series	58.96	46.79	67.01	7.2
O	8	K-series	23.48	18.63	20.03	3.0
Si	14	K-series	4.02	3.19	1.95	0.2
S	16	K-series	23.19	18.40	9.87	0.8
Ca	20	K-series	0.02	0.01	0.01	0.0
Au	79	M-series	16.34	12.97	1.13	0.6
		Total:	126.01	100.00	100.00	

Figure 4.S3. SEM of PEDOT/SDS at 10007× magnification and EDX spectrum of the needle-like structure of PEDOT/SDS.

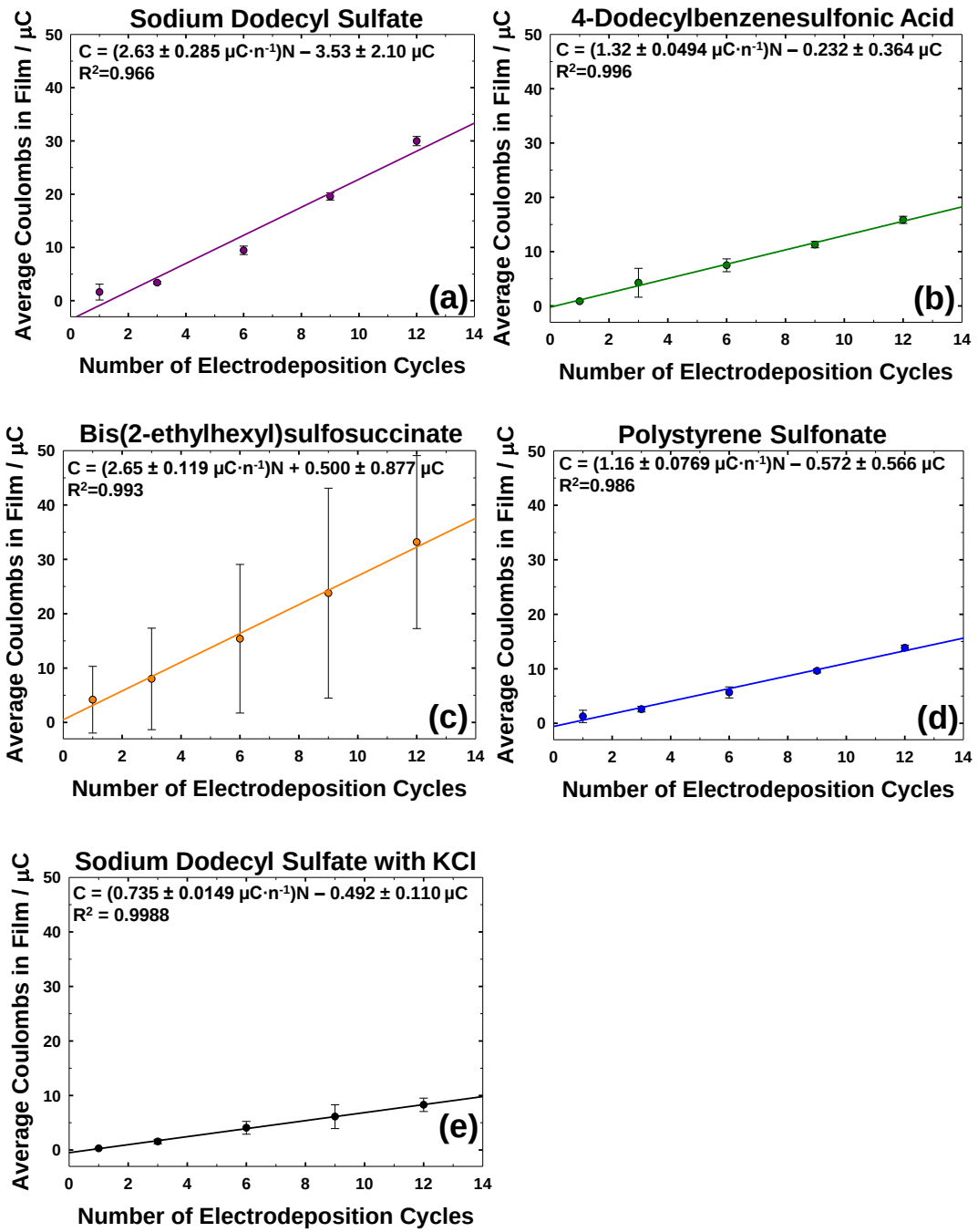

Figure 4.S4. Average coulombs in films vs the number of electrodeposition cycles for each of the deposition conditions (a) SDS (b) DBSA (c) BEHS (d) PSS (e) SDS and KCl. These graphs demonstrate the growth of film over time.

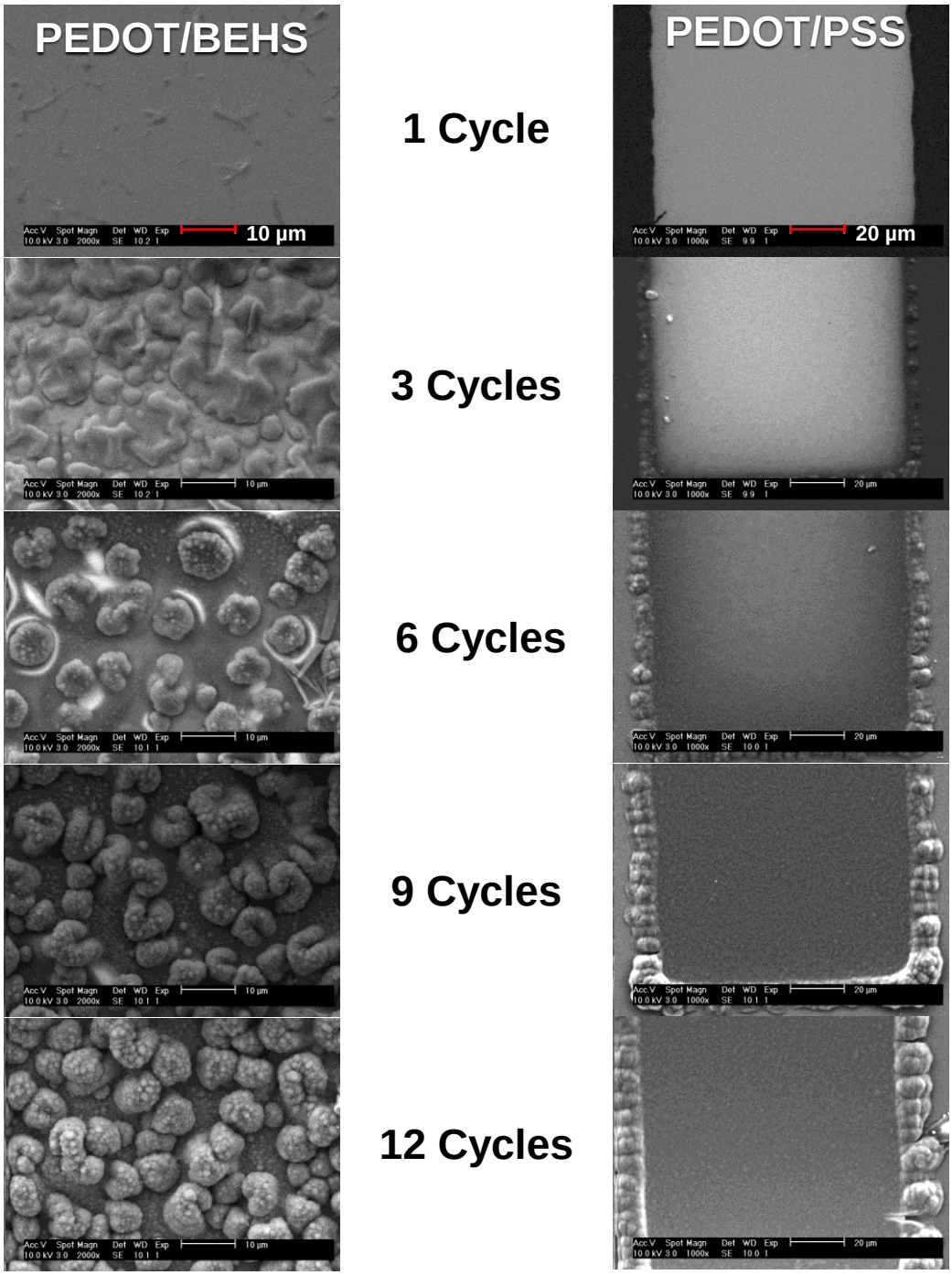

Figure 4.S5. SEM images of PEDOT polymerized in BEHS and in PSS using an increasing number of deposition cycles. The pictures of the PEDOT/BEHS films were taken at 2000x magnification and the pictures of the PEDOT/PSS films were taken at 1000x.

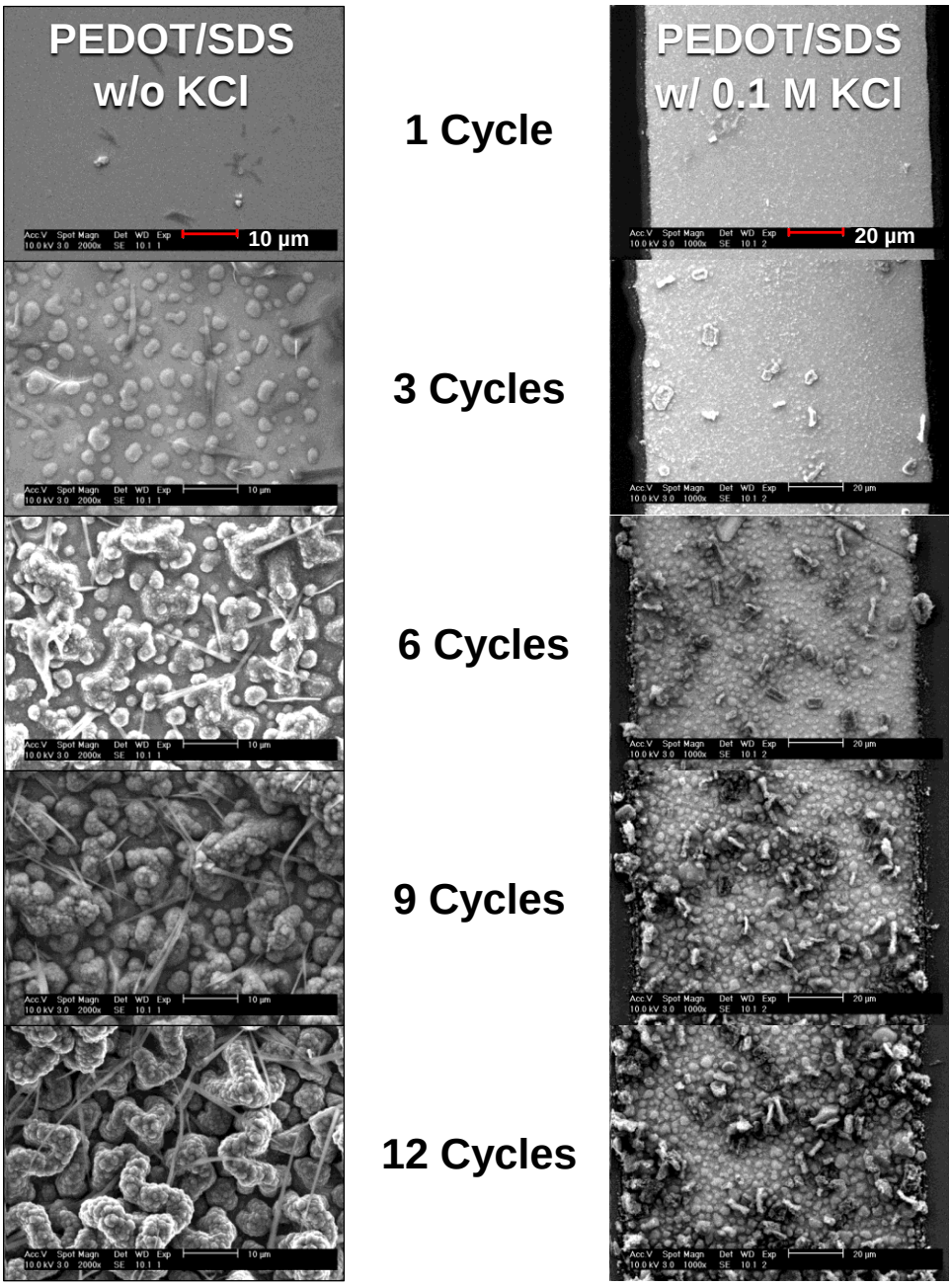

Figure 4.S6. SEM images of PEDOT polymerized in SDS only and SDS in KCl using an increasing number of deposition cycles. The pictures of the PEDOT/SDS films were taken at 2000x magnification and the pictures of the PEDOT/SDS/KCl films were taken at 1000x.

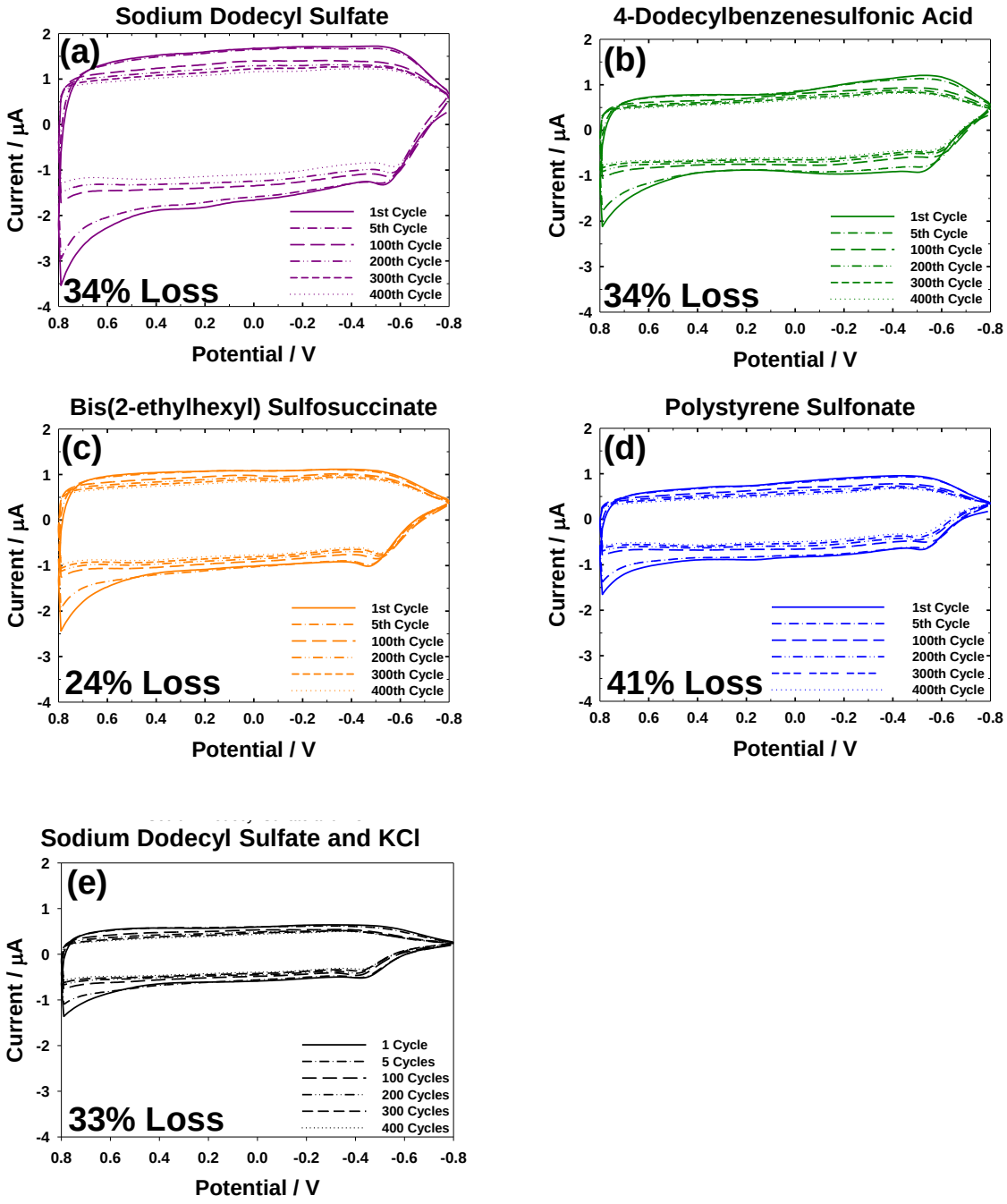

Figure 4.S7. Endurance study of PEDOT films of different deposition solutions (a) SDS (b) DBSA (c) BEHS (d) PSS (e) SDS and KCl. The potential was cycled between -0.8 V and 0.8 V at 0.100 $V \cdot s^{-1}$ for 400 cycles to investigate the electrochemical stability of the films.

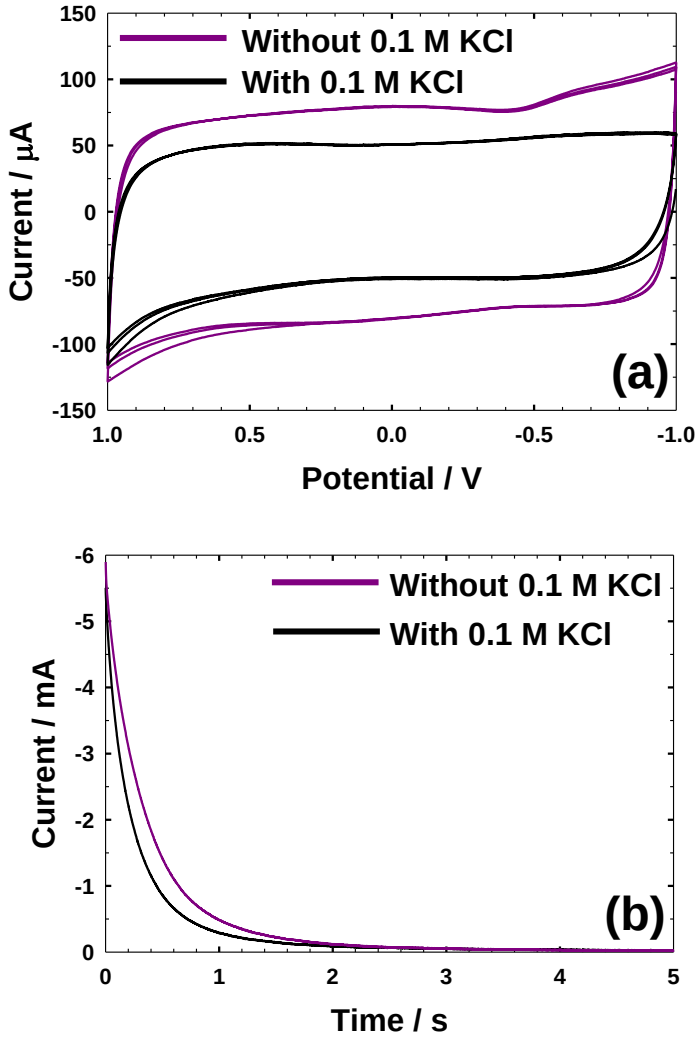

Figure 4.S8. Current responses during CV and CA experiments for PEDOT films deposited in SDS with and without KCl.

5. Poly(3,4-ethylenedioxythiophene)-Modified Electrodes for AC-Magnetohydrodynamic (AC-MHD) Microfluidic Pumping

5.1 Abstract

A paradigm shift in redox-MHD microfluidics is demonstrated that preserves its advantages and resolves problems that have previously slowed the application in analytical chemistry of MHD for pumping small volumes of fluids and sustaining fluid flow. This study uses an array chip with patterned microband and microring-disk electrodes with solution confined with a gasket and a lid. The chip was placed on an electromagnet (0.0161 T RMS) which generated a magnetic field with a direction perpendicular to the chip. The electrodes were modified with a conducting polymer, poly(3,4-ethylene dioxythiophene) (PEDOT) to generate ionic current density, instead of adding redox species in solution which had been done previously to avoid bubble formation and electrode corrosion. Synchronized sinusoidal potential waveforms were applied to PEDOT-modified electrodes and the electromagnet (to generate an AC magnetic field). This allows for continuous pumping in a single direction while charging and discharging the PEDOT films. The bias of the electrodes was switched with a frequency of only 10 Hz so that heating was minimal compared to prior AC MHD studies, generating high currents, and therefore, fluid velocities that are comparable to those previously achieved with similar cell geometries when redox species were present in solution. A flat flow profile with an average velocity of 115 $\mu m \cdot s^{-1}$ was observed at PEDOT-modified microband electrodes, which would be of use for microfluidic pumping. A spiraling fluid flow profile was demonstrated at PEDOT-modified concentric disk-ring electrodes with fluid flow as high as 350 $\mu m \cdot s^{-1}$ adjacent to the disk electrode and 10 times the velocities achieved with redox species in solution previously that could be valuable for lab-on-a-chip mixing applications.

5.2 Introduction

This paper focuses on AC redox-MHD, which takes advantage of alternating the current of PEDOT-modified electrodes with an alternating magnetic field for continuous microfluidic pumping. In previous studies, we described that PEDOT-modified electrodes are capable of high currents while limiting the interaction with the sample, thus improving compatibility. In spite of its many advantages, the PEDOT-modified redox-MHD limits experiments to short time frames because it cannot sustain the current once the coulombs in the film are exhausted, unlike diffusion-limited redox species in solution. Nonetheless, PEDOT is highly reversible. The device used in this study takes advantage of this feature to allow redox-MHD at PEDOT-modified electrodes to be sustainable over indefinitely long times by recycling PEDOT in real time. In order to pump continuously in one direction, the bias of the electrodes was sinusoidally varied to cycle PEDOT and simultaneously synchronized with an alternating magnetic field direction. AC redox-MHD solves many previously encountered problems, and thus should greatly expand MHD for LOAC applications.

The miniaturization of analytical techniques that are normally performed in a full lab setting to a lab-on-a-chip (LOAC) device promises to improve portability, power consumption, reagent and waste volumes, automation, and analysis time. LOAC devices show promise for revolutionizing analysis done in medical diagnosis, environmental impact field studies, genomic studies, and synthetic reactions.[1-3] A crucial aspect of LOAC applications is the microfluidics, or the manipulation of small amounts of fluid within the device. Ideally, the microfluidic technique should be able to pump fluid between two locations, easily reverse fluid flow direction, adjust fluid flow velocity, trap species within a certain volume, mix solutions of different composition, and split off a fluid volume for further handling.[4] Magnetohydrodynamics (MHD) has these capabilities through the careful programming of electrodes in the presence of a magnetic field.

MHD takes advantage of the interaction between electric and magnetic fields. In MHD, the magnetohydrodynamic force, $\mathbf{F_B}$ ($N \cdot m^{-3}$), and therefore fluid flow, is generated by ionic current density, $\mathbf{j}$ ($C \cdot s^{-1} \cdot m^{-2}$), that is perpendicular to a magnetic field, $\mathbf{B}$ (T). The magnitude and direction of $\mathbf{F_B}$ follow the right-hand rule according to the cross-product relationship, $\mathbf{F_B} = \mathbf{j} \times \mathbf{B}$.[5-8] The use of MHD in microfluidic devices can provide continuous pumping without channels or moving parts and can stop or reverse fluid

flow by switching off the current or changing the sign of the ionic current density respectively without the need of valves.[9] One of the first approaches that used MHD to pump solutions directly for microfluidics used direct current (DC) applied to electrodes on either side of a channel filled with electrolyte only in the presence of a uniform magnetic field generated from a permanent magnet.[10-14] This method when applied to aqueous solutions corroded electrodes and produced bubbles from the electrolysis of water, interrupting fluid flow. It is possible to place the electrodes outside of the channel (but where ionic conductivity passes through frits) to avoid the interference of the bubbles, but the bubbles still need to be released and channel construction is complicated.[15, 16]

One method used to prevent bubble generation and electrode degradation is the addition of redox species to the pumping fluid, thus lowering the potential needed to generate sufficient currents for pumping.[9, 17-22] Low concentrations of redox species have been shown to be compatible with heart tissue and with alkaline phosphatase, an enzyme commonly used in immunoassay applications.[20, 23] However, the introduction of redox species raises concern about risk of contamination and interference with analyte detection and with the biocompatibility of the pumping system. Previous work in our research group addressed these concerns by immobilizing the redox species to the electrode surface, thus limiting the interaction between redox species and the sample.

The conducting polymer, poly(3,4-ethylenedioxythiophene), (PEDOT) electropolymerized on the electrode surface can function as a source of coulombs, to generate current at the electrodes and to effect ionic current density throughout the electrolyte between the active electrodes. PEDOT-modified electrodes are capable of generating high currents, and therefore high fluid velocities. This is because the redox species are highly concentrated and located directly on the electrode surface, do not have the dilution effect caused by passing through a depleted diffusion layer to the electrode surface, and do not require the extra time needed to do that. Previously, we demonstrated the fluid flow between oppositely biased, long microband electrodes[24] useful for microfluidic pumping applications and fluid flow between concentric ring-disk microelectrodes[25]useful for stirring applications.

Despite its advantages, PEDOT-modified electrodes limit redox-MHD microfluidic pumping to short time frames because they cannot sustain the current once the coulombs are exhausted, unlike diffusion-limited redox species that can continue to produce current over longer times in solution.

Nonetheless, PEDOT is highly electrochemically reversible.[26] Consequently, before further pumping can take place the films have to be electrochemically regenerated. The study herein takes advantage of this feature to allow redox-MHD at PEDOT-modified electrodes to be sustainable over indefinitely long times by recycling the PEDOT in real time.

Previous work in our laboratory utilized a "replenishing" approach that involves the alternate activation of two sets of oppositely biased microelectrodes with an electronic switch between the potentiostat and the electrochemical cell filled with redox species (0.1 M $K_3Fe(CN)_6$ and 0.1 M $K_4Fe(CN)_6$ in supporting electrolyte 0.1 M KCl).[21] Mass transport replenishes the redox species that are depleted in the diffusion layer from the surrounding solution at the inactivated electrodes, to supply a new source of coulombs upon activation in the next cycle. This approach also harnesses the transient faradaic current response associated with stepping the potential past the standard electrode potential of the redox species in solution, which could be viewed as analogous to the large transient current observed at the PEDOT-modified electrodes during chronoamperometry, (CA). However, in the PEDOT case, there are no redox species in the surrounding solution to "recharge" the electrodes.

In order to pump continuously in one direction while cycling PEDOT, the direction of the current at the electrodes (as a result of changing the bias) must be simultaneously altered with the variation of the magnetic field direction. In the studies described here, a single electromagnet was placed beneath the electrode chip to generate an AC-magnetic field by running a sinusoidal potential function through a power amplifier to increase the current to drive the electromagnet. A second function generator, synced with the first function generator, was used to apply a sinusoidal or step potential function with amplitude of ±0.8 V of the same frequency between two PEDOT-modified electrodes in a supporting electrolyte.

Electromagnets have been used in the past for AC-MHD pumping for microfluidic systems with channels, without added redox species, and at bare electrodes. In the early work by Lemoff and Lee, a sinusoidal electric current of sufficiently high frequency (> 1 kHz) was passed through an electrolytic solution to prevent bubble generation and electrode degradation because it was anticipated that the chemical reactions are reversed rapidly.[27] Higher currents, and therefore higher velocities, were possible at the higher frequencies before bubble formation became a problem, but the magnetic field dropped significantly above 1 kHz, and therefore higher frequencies were not investigated.

In a variety of microfluidic systems, low Reynolds numbers are observed (<1), meaning that the flows are considered laminar. Because these flows usually have little turbulence, mixing is often difficult and relies on diffusive species mixing, which is inherently slow.[4, 28] West et al. used AC-MHD in an annular device design where a concentric disk (radius of 4 mm) and ring (internal radius of 5 mm) electrodes with a 500 µm deep and 2 mm wide channel separating them. A 1 kHz AC potential waveform was used to generate a non-uniform flow profile to enhance mixing of two fluids being pumped in a loop.[29, 30] Eijkel and coworkers fabricated an annular device design with 200 µm wide and 30 µm high channel structure with gold walls for chromatographic applications.[31] It should be noted that for AC-MHD micropumps using electrolyte alone, a compromise in frequency must occur. Higher frequencies allow for higher currents before bubble generation from electrolysis is a problem. However, at high frequencies, heating due to eddy currents caused by rapidly changing magnetic field can be an issue and is proportional to the square of the frequency.[31, 32] For example, Eijkel and coworkers lowered the frequency of their AC MHD micropump from 22 kHz to 2.44 kHz, lowering the device temperature from 45˚C above room temperature to only 15˚ C above, but this also decreased the current (and therefore fluid velocity). In addition, the magnetic field suffers at higher frequencies and, is weak (10 to 100 mT) compared to magnetic fields produced by permanent magnets and DC electromagnets.[27, 29, 33, 34]

PEDOT-modified electrodes enhances current amplitude compared to bare electrodes while avoiding addition of redox species to the solution as well as avoiding bubble formation and electrode degradation. At the same time, lower frequencies can be used so that the electromagnet can be at a higher magnetic flux density, while eddy currents and inductive heating can be avoided, PEDOT-modified electrodes have >1100× the coulombic capacity of a bare electrode of the same geometry and a much slower response time due to its redox properties, which allows slower frequencies. In addition, the high currents achievable at PEDOT-modified electrodes offset the loss in velocity due to weaker fields of the AC electromagnet, producing fluid speeds which are comparable to DC redox-MHD. Conversely, AC-MHD addresses the limited time-scale problem of PEDOT-modified electrodes for redox-MHD in microfluidic applications. In this work, AC redox-MHD pumping is generated at oppositely biased PEDOT-modified microband electrodes and concentric ring-disk microelectrodes, demonstrating sustainable microfluidic pumping without the need for added redox species to produce straight flow and

mixing through spiraling flow, respectively. The approach and results provide a great advance in the MHD microfluidic field.

5.3 Experimental Section

5.3.1 Chemicals and materials. The substrate materials for the electrode arrays were silicon wafers (125-mm diameter and 600-650-µm thick with 2 µm of thermally grown SiO_2 on the surface) purchased from Silicon Quest International (Santa Clara, CA). A chromium-plated tungsten rod (Kurt J. Lesker Company, Clairton, PA), gold coin (Canadian Maple Leaf, 99.99%), and a molybdenum boat (Kurt J. Leskar Company, Pittsburg, PA) were used for metal deposition. Benzocyclobutene, BCB, (Cyclotene 4024-40) purchased from Dow Corning Company (Midland, MI) was used to insulate the electrode leads. Positive photoresist (AZ 4330) was purchased from (Advance Reproductions Corporation, North Andover, MA. Gold etchant (Transene, GE8148) and chromium etchant (HTA enterprise, CEP200) were used as received. Connection from the chip to the potentiostat was made via an edge connector (solder contact, 20/40 position, 0.05 in. pitch) purchased from Sullins Electronics Corp. (San Marcos, CA). Aqueous solutions were made with reagent grade, 18 MΩ, deionized water from Ricca Chemical Company (Arlington, TX). Sodium dodecyl sulfate was bought from aMResco (Solon, OH). The monomer of PEDOT, 3,4-ethylenedioxythiophene, was obtained from Sigma-Aldrich (St. Louis, MO). Sodium chloride was obtained from EMD Chemicals Inc. (Gibbstown, NJ). Polystyrene latex microspheres, 10.0 micron diameter (2.5 wt% dispersion in water) and ruthenium(II) hexaammine chloride were purchased from Alfa Aesar (Ward Hill, MA). The as-received ruthenium(II) hexaammine chloride contained the oxidized form, as well, resulting in near 1:1 mixture of each species. A poly(dimethyl siloxane), PDMS, gasket was fabricated using OS-30 solvent, Sylgard184 silicon elastomer base, and Sylgard 184 silicon elastomer curing agent (Ellsworth Adhesives, Milwaukee, WI). Pre-cleaned microscope glass slides (1.5 × 1.0 × 0.1 $in.^3$) were obtained from VWR. ColdShield Paste was obtained from Greer, SC.

5.3.2 Microelectrode Chips. An in-depth description of the fabrication procedure of these chips can be found in previously published work.[9] A chromium-plated tungsten rod and a gold coin (Canadian Maple Leaf, 99.99%) were placed in a molybdenum boat and used for metal deposition onto silicon wafer, forming the layer that would become the electrode arrays. Wafers were cleaned using Radio

Corporation of America (RCA) procedure. Positive photoresist (AZ 4330) was used for the electrode feature transfer from photo plot masks (Advance Reproductions Corporation, North Andover, MA) to the silicon wafer. To remove excess photoresist in the photolithography process, tetramethyl ammonium hydroxide (TMAH) solution was used as a developer. The chips are diced to 1 in. × 2 in. The design on each chip includes 12 gold microband electrodes which are in three sets of four (each electrode is 100 µm wide and 2.5 cm long with a 100 µm gap between electrodes within the set) and four sets of gold concentric ring and disk electrodes varying in size (Figure 1a). The first and second set of band electrodes are separated by a 5600 µm gap and the second and third sets are separated by a 2000 µm gap. The microband electrodes were used to demonstrate the microfluidic pumping capabilities. The largest of the concentric ring-disk sets (disk radius = 160 µm, inner ring radius = 1600 µm, outer ring radius = 2000 µm) was used to demonstrated rotational flow for mixing applications.

5.3.3 Characterization of Electrodes Prior to and After Modification. A CHI 760B bipotentiostat (CH Instruments, Austin, TX) was used to perform all electrochemical manipulations. Bare electrodes were characterized prior to electropolymerization in a beaker of solution containing 5.0 mM $Ru(NH_3)_6^{2+/3+}$ and 0.100 M NaCl and in a solution of 0.100 M NaCl alone using CV and CA. For the characterization of the microband electrodes, the working electrodes consisted of the four microband electrodes in set 1 shorted together while the electrodes in sets 2 and 3 served as the counter electrodes. When characterizing by CV, the potential was cycled from -0.600 V to 0.600 V versus a Ag/AgCl (saturated KCl) reference electrode at 0.05 $V \cdot s^{-1}$. For CA experiments, the potential was stepped to 0.300 V and held for 20 s. After the electrodes were modified with PEDOT, the electrodes were characterized in a beaker of solution containing 0.100 M NaCl. For CV characterization, the PEDOT-modified electrodes were cycled from -1.00 V to 1.00 V at 0.05 $V \cdot s^{-1}$. During CA, the PEDOT-modified electrodes were held at -0.300 V for 10 s and then stepped to +1.00 V and held for 20 s (Figure 1c). Electrochemical impedance spectroscopy (EIS) was used to characterize PEDOT film deposited with the same procedure on 250 µm × 100 µm microelectrodes to assess the phase shift at 10 Hz. EIS studies were performed using a PARSTAT MC (from AMETEK in Oak Ridge, TN) applying an excitation perturbation amplitude of 800 mV

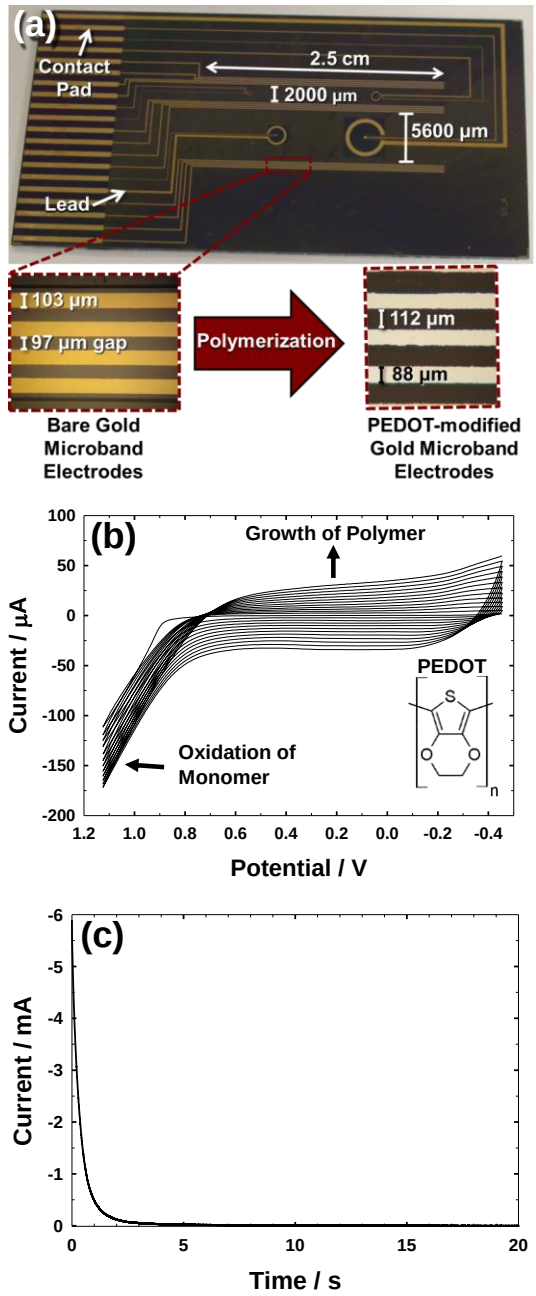

Figure 5.1. (a) Photograph of the microelectrode array chip showing electrode features and dimensions. Expanded images show unmodified gold and PEDOT-modified gold band electrodes as viewed under a microscope. (b) Cyclic voltammogram during electrodeposition of PEDOT onto one microband electrode. Inset picture of chip shows chemical structure of PEDOT. (c) Electrochemical response during an applied potential experiment of +1.0 V at microband electrode set 1 shorted together vs microband electrode sets 2 and 3 shorted together as combined auxiliary/quasi-reference electrodes.

root mean square (RMS). Measurements were carried out over a frequency range of 1 Hz to 10^5 Hz with 10 points per decade. A measurement delay of 30 s was used before each point was taken. VersaStudio V2.40.4 (© 2013) software was used to record.

5.3.4 Electrodeposition of PEDOT onto microelectrodes. Prior to characterization and modification, the chips were cleaned with an oxygen plasma cleaner for 15 min. A solution of 0.010 M 3,4-ethylene dioxythiophene (EDOT) and 0.010 M sodium dodecyl sulfate (SDS) was sonicated for over two hours until the EDOT was completely dissolved. To electrodeposit PEDOT onto the electrodes, the chip was immersed in a beaker containing monomer solution and the electrodes were cycled between -0.455 V and 1.125 V vs Ag/AgCl, (saturated KCl) at 0.05 $V \cdot s^{-1}$ for 12 cycles (Figure 1b). A platinum flag electrode served as the counter electrode. These conditions were chosen because we have demonstrated the effectiveness of these electrodes for MHD applications in the past. The films produced were dark blue and thick, capable of high coulombic capacity and fast electrochemical response, which is ideal for MHD applications.

5.3.5 Electronics for AC-MHD. Two function generators were used to produce the potential waveforms to drive the electrodes and the electromagnet: Tektronix AFG310 and Hewlett Packard 33120A respectively (Figure 5.3). Both sinusoidal and squarewave wave functions were examined. The phasing of the two potential waveforms was monitored using a dual channel oscillope (Tektronix, Beaverton, OR) and was changed using the phasing capabilities of the tektronix function generator. A 200 W discrete power amplifier kit (K8060) was purchased from Velleman (Gavere, Belgium) and was assembled according to the assembly manual. A power transformer was bought separately from TRIAD Magnetics (Perris, CA) to complete the power amplifier circuit. The power amplifier circuit was heat sinked to a large piece of aluminum (0.5 in. thick, 6.25 in. wide, and 18 in. long) to dissipate heat. A switch and a fuse were added to the circuit design to easily turn off the electromagnet and to protect with power amplifier circuit from excess current.

The electromagnet was purchased from APW Company (Rockaway, NJ). The electromagnet (EM400-6-212) was 4 in. diameter × 1.65 in. with a hole measuring 3/8-16 x 1 3/4" to accommodate mounting hardware (Figure 2a). In order to extend the magnetic field through the hole, a soft iron bolt was placed through the hole in the electromagnet and through the hole in the microscope stage. An

aluminum nut was machined so that the electromagnet was immobilized on the microscope stage. Thechip was placed on top of the center cylinder of the electromagnet. The magnitude of the AC driving the electromagnet was 5.41 A. The AC-magnetic field was measured using a Tri-Alpha DC/AC-magnetometer (Salt Lake City, UT). Because of the high currents that are needed to drive the electromagnet and because of the direction of the magnetic field is switching frequently, it was realized that the electromagnet would generated heat over the time it was used. Heat transfer from the electromagnet to the fluid in the cell would likely cause fluid movement due to natural convection. In order to slow the heat transfer between the electromagnet and the chip, a thin layer (< 1 mm) of heat shielding paste was added to the bottom of the chip. The heat of the electromagnet and of the solution in the electrochemical cell was measured using a Noncontact Infrared Temperature Measurement (Raytek MiniTemp MT6, Santa Cruz, CA).

Connection was made to the contact pads of the electrodes by using an edge connector which was sawed in half. This allowed the chip to be flush with the electromagnet surface where the electrochemical cell would experience the highest possible magnetic field. The edge connector was placed on top of the contact pads on the chip and was carefully aligned. The edge connector needed an appropriate amount of downward force to form a good connection with the contact pads of the chip. A bar of plexiglass (1 in. wide × 3.5 in. long × 0.25 in. thick) was machined and holes on both ends of the bar were drilled. Holes were also drilled into the side wall of the electromagnet and were threaded to accommodate screws which were used to tighten the plexiglass bar on top of the edge connector to improve the connection to the chip and to hold everything in place (Figure 5.2a). Plexiglass was chosen for its transparency, which made the process of lining the edge connector with the chip easier.

5.3.6 AC-MHD Experimental Setup. In the MHD experiments described below a PDMS gasket (750 μm thick with a rectangular opening cut out of 3.2 cm $\times$ 1.5 cm) placed on top of the chip defined the dimensions of the cell (Figure 5.3). The opening in the PDMS gasket was wide enough that the pumping electrodes were more than 1 mm away from the walls to contain the solution while not defining any sort of channel. A glass slide was placed on top of the PDMS gasket to serve as a ceiling of the cell and limit movement in the vertical direction. To visualize the flow of solution around the PEDOT-modified electrodes, polystyrene latex microbeads (10 μm diameter) were added to the solution and their

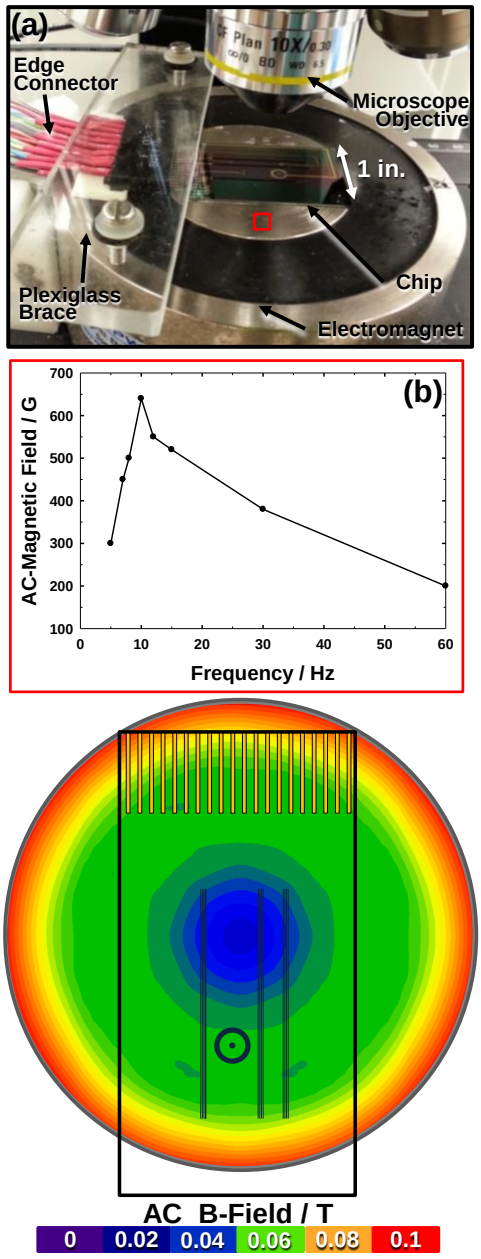

Figure 5.2 (a) Photograph of the AC-MHD experimental setup showing the electromagnet, edge connector, plexi-glass bar for holding edge connector, and chip. (b) Graph showing the AC-magnetic field (T) versus the frequency of the potential waveform (Hz) applied to the electromagnet. (c) Illustration of the AC-magnetic field (T) over the core of the electromagnet and the position of the chip.

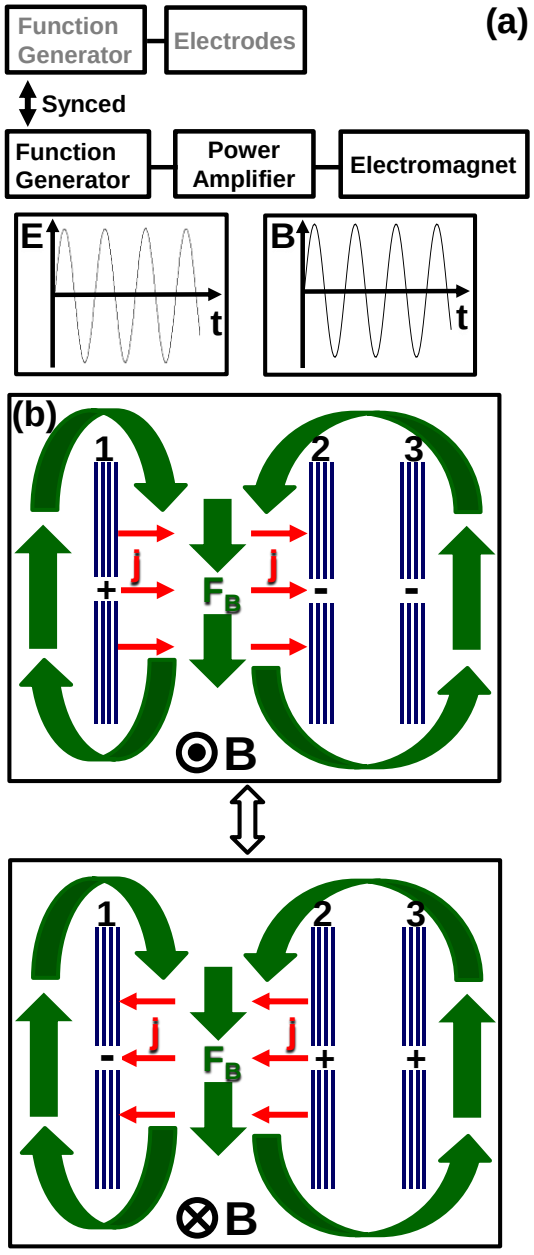

Figure 5.3 (a) Block diagram for the electronics of the experimental setup. (b) Vectors involved in AC-MHD for synchronized electrical and magnetic fields to maintain flow in a single direction.

movement was recorded over time using a microscope interfaced with a Sony Handycam camera. The x- and y-position of the recorded video were adjusted using the microscope stage. The height above the chip surface was adjusted for the video recording by raising and lowering the microscope stage in the z-direction. The movement of the beads in solution within ±75 μm of the microscope's focal plane were analyzed using particle imaging velocimetry (PIV) analysis with Dynamic Studios.[18] The PIV software measures the displacement of the beads in solution to determine the 2D velocity field by breaking the video frames into interrogation regions, and then following bead patterns in subsequent frames. The bead velocities in each interrogation region are averaged together.

The horizontal flow profile in the 5600 μm gap between PEDOT-modified microband electrodes was examined during two AC redox-MHD experiments. For these experiments, on of the function generator leads was connected to microband electrode set 1 while the other lead was connected to sets 2 and 3. The video was taken 300 μm above the chip. The microscope was initially focused on the PEDOT-modified electrodes on one side of the gap and was gently moved by 1 mm every 10 s across the 5600-μm gap until the microband electrode set 2 came into view. One experiment began with the camera focused on the microband electrode set 1 and one experiments focused on the set 2 electrodes. The PIV software calculates columns of velocity vectors across the video screen (see Figure 5.5a). The distance from microband electrodes set 1 was calculated for each column of velocity vectors. The data for the two experiments was compiled and organized into bins (to the nearest 0.1 mm). The average and standard deviation of each bin were calculated. Because the video recorded a location that was 1.34 mm wide at each position and the stage was moved in 1 mm increments across the gap for each position, areas of overlap exist; these data points were averaged together and the pooled standard deviation was calculated accordingly.

Experiments were also done at PEDOT-modified ring-disk electrodes. For these experiments on function generator lead went to the disk electrode, while the other went to the ring electrode to complete the circuit. The camera was not able to capture bead movement over the entire ring-disk electrode area, so video microscopy was focused on the disk electrode to observe the highest fluid flows. In addition, the fluid flow was examined at 3 different heights throughout the cell during two separate experiments: 150,

300, and 450 μm above the chip. Velocity vectors from the PIV analysis along the diameter of the ring were used to make contour plots to illustrate the flow profile between the ring and disk electrodes.

5.4 Results and Discussion

5.4.1 Distribution of Magnetic Flux Density Across Chip. The magnetic field was measured as a function of frequency of the potential waveform applied to the coil between 5 and 60 Hz (Figure 5.2b). The magnetic field strength increased from 0.03 T at 5 Hz to 0.065 T at 10 Hz. Once greater than 10 Hz, the magnetic field strength decreased (at 60 Hz, $\mathbf{B}_{AC}$ = 0.02 T). Frequencies above 60 Hz were not examined due to inductive heating problems that occur with higher frequencies, but it is predicted that the magnetic field strength would continue to decrease as frequency increased. For the MHD experiments described, 10 Hz was used to power the AC-MHD device at the highest magnetic field possible for our setup, thus enabling the greatest fluid velocity. Even at this low frequency, the temperature of the electromagnet increased over time due to the high currents used to drive the electromagnet. Heat shielding paste was added to the bottom of the chip to slow the transfer between the electromagnet and the chip. Figure 5.S1 in the supplemental section shows the change in temperature over time of the electromagnet and the solution in the cell. Within the time frame of the experiments done in this study, the temperature of the electromagnet increased from 23.1 to 30.3 ˚C while the temperature of the solution only increased from 23.1 to 25.8 ˚C. At this temperature change, MHD would be the dominant microfluidic force rather than natural convection from the temperature change in solution. However, for longer time frames, a better insulator would be necessary to prevent fluid movement from natural convection.

The magnetic field strength changed radially from the center of the electromagnet. Figure 5.2c shows magnetic field strength over the core of electromagnet. The soft iron bolt extends the magnetic field over the hole in the center which is used for mounting the electromagnet. However, the magnetic field strength over the center is lower (~0.025 G) because the bolt is 3 mm lower than the surface of the electromagnet. The magnetic field increases over the cylindrical core to 0.065 T at 2 cm from the center and finally is at its highest at the outside edge of the core (0.0975 T). Figure 5.2c also shows the placement of the chip and the position of the electrodes over the core. The magnetic field changes quite

drastically along the 2.5 cm length of the 5600 µm gap between the working and counter microband electrodes from 0.0260 T to 0.059 T. The AC magnetic field at the concentric ring-disk electrodes used for inducing rotation flow was 0.059 T.

5.4.2 Effect of Relative Phasing of Potential Waveforms of Electrodes and Electromagnet on Fluid Flow. The relative phasing of the potential waveforms from both function generators were monitored using a dual channel oscilloscope. The two waveforms were initially synced manually by adjusting the phasing on one of the function generators. The phasing was adjusted by 45° every 10 s and the fluid flow was recorded throughout the experiment. Later, the bead movement was quantified via video microscopy using 3 to 5 s of video. Figure 5.4 shows the effect of relative phasing of the potential waveforms for both sinusoidal (a) and square-wave potential waveforms (b). Both waveforms exhibit sinusoidal fluid velocity vs the relative phasing of the potential waveforms where fluid flows are greatest (but in opposite direction) when the waveforms are completely in phase or are 180° out of phase. Therefore, both the direction and the magnitude of the fluid flow can be carefully adjusted by changing the relative phasing of the potential waveforms. These results match well with observations made by Lemoff and Lee during AC-MHD experiments in electrolyte alone.[27] Interestingly, EIS analysis showed a 27° phase shift at 10 Hz, which is much lower than for bare gold electrodes (Figure S-3). This would be beneficial for lab-on-a-chip applications where fluid flow needs to be carefully adjusted for different functions within the device, i.e. reversal of fluid flow or pumping and incubation periods. By simply adjusting the phase shift by 180°, one can reverse the fluid direction. It should be noted that slightly higher maximum fluid velocities were observed using square-wave potential waveforms; however, square-wave potentials waveforms suffer from worse heating effects due to the large step in potential as compared to sinusoidal (see Supplemental Section). Therefore, the following experiments use sinusoidal waveforms to generate the electric and magnetic fields.

5.4.3 Horizontal Flow Profile between Working and Counter Microband Electrodes. In past studies, the flow profile between microband electrodes for both solution-based redox species and PEDOT-modified electrodes has been shown to be relatively flat during DC-MHD experiments.[24] Similar results are seen in AC-MHD experiments (see Figure 5.5). For the majority of the 5600 µm gap, the fluid flow is approximately 115 $\mu m \cdot s^{1}$. Impressively, these fluid flows are within error of velocities observed in

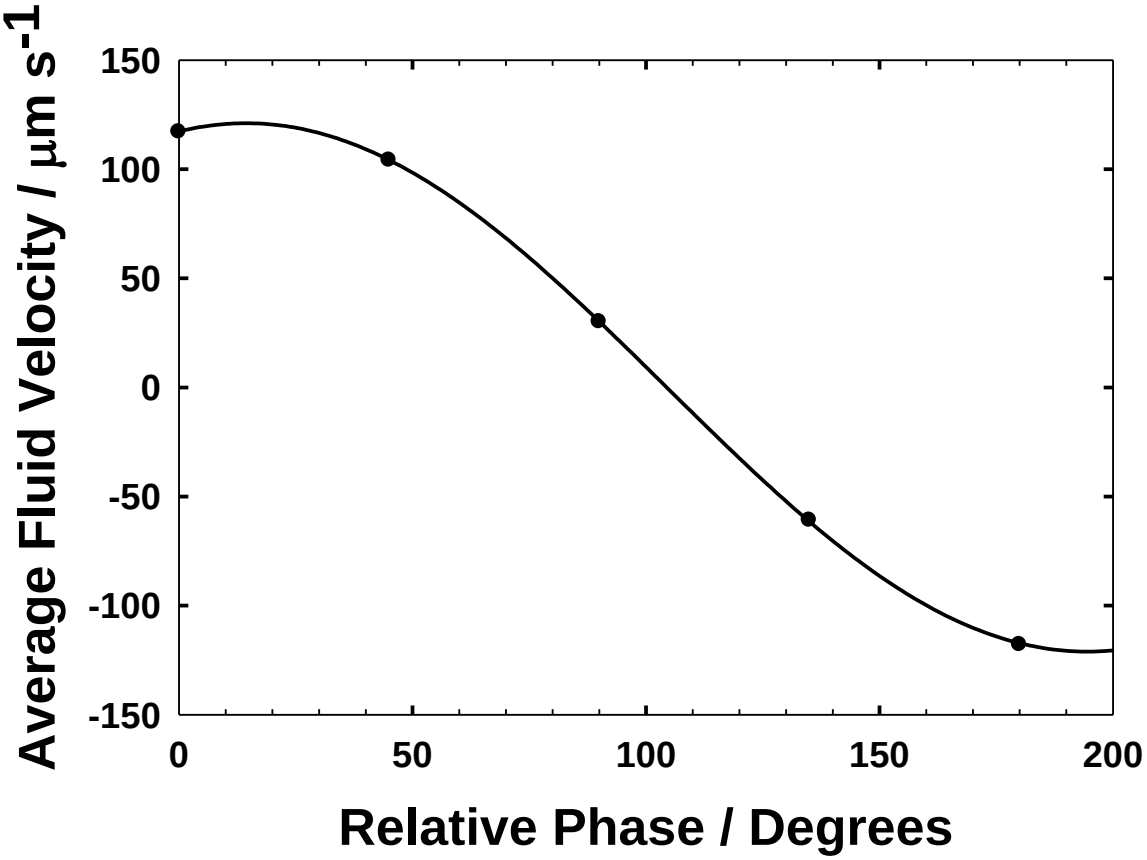

Figure 5.4 Dependence of average fluid flow velocity (µm·s^{-1}) on the relative phase (°) between the potential waveforms applied to the electrodes and to the electromagnet for sinusoidal potential waveform.

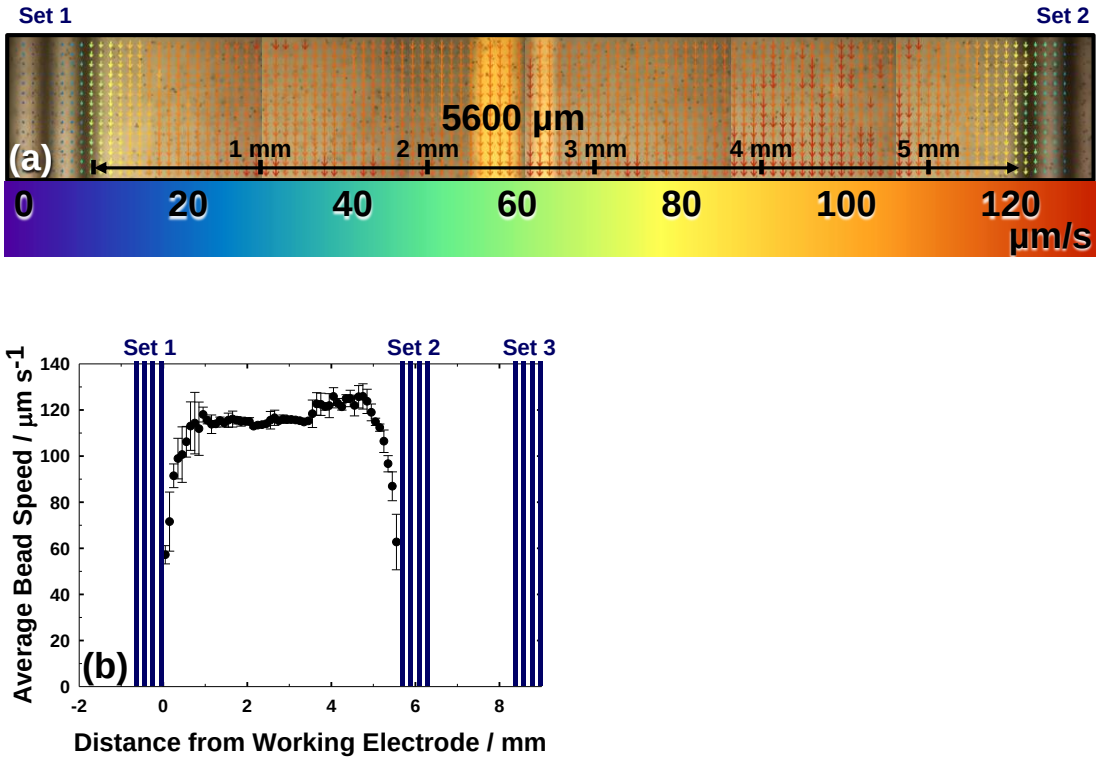

Figure 5.5 (a) PIV images illustrating flow profile in the 5600 µm gap between PEDOT-modified microband electrodes. (b) Average bead velocity (µm·s^{-1}) versus distance from working electrodes (mm). Error bars are the standard deviation for each of the data points.

DC-MHD using 0.095 M $K_3Fe(CN)_6$, 0.095 M $K_4Fe(CN)_6$, and 0.095 M KCl at the same electrode design in the presence of a 0.36 T permanent magnet which is much higher than the field generated by the electromagnet used in these studies.[24] Therefore, there must be an increase in current observed at PEDOT-modified electrodes as compared to solution-based redox species to offset the decrease in magnetic field strength. DC redox-MHD has been performed at the same electrode geometry with the same PEDOT films. The average fluid velocity across the gap during an applied current experiment of -500 μA in the presence of a 0.37 T magnet was 268 $\mu m \cdot s^{-1}$. Because the PEDOT films are being charged and discharged at a frequency of 10 Hz, the transient faradaic and charging current is being utilized. A multimeter connected in series with one of the leads to the electrodes measure the AC current to be 2.27 mA. The non-oscillating equivalent of a sine wave is known as root mean square (r.m.s) amplitude and is found by dividing the amplitude of a sine wave by $\sqrt{2}$. Therefore, the amplitude of the AC current is 1.61 mA r.m.s. The average of the measured AC B-field over the length of the bands was 0.047 T. The r.m.s. amplitude of the AC B-field is 0.033 T r.m.s. The flow velocity is lowest in the middle of the gap which has been observed in solution based and immobilized redox species. The highest velocities are observed just to the inside of the counter electrodes.

5.4.4 Fluid Flow at PEDOT-modified Concentric Disk-Ring Microelectrodes. Rotational fluid flow has been demonstrated for PEDOT-modified disk and ring electrodes; however, fluid flow in one direction can only be maintained in one direction for a limited amount of time. The fluid flow velocity was highest close to the disk electrode for a given height. As the distance increased radially from the disk electrode, the fluid velocity decreased. This non-uniform flow profile is due to the ionic current density distribution which is caused by the difference in electrode area of the disk and ring. This creates a spiraling fluid flow which could be of value for on-chip mixing applications. Figure 5.6 shows a top-down view (a) and a cross-sectional view (b) of the AC-MHD setup for concentric disk and ring electrodes. The flow profile obtained with AC-MHD at PEDOT-modified electrodes was similar to DC-MHD experiments. Figure 5.7a shows the PIV image for the fluid flow around the disk electrode at 150 μm above the chip. This same data is also portrayed in Figure 5.7b, which plots fluid speed vs the distance from the center of the disk electrode. This plot highlights another interesting flow profile features of redox-MHD at ring-disk

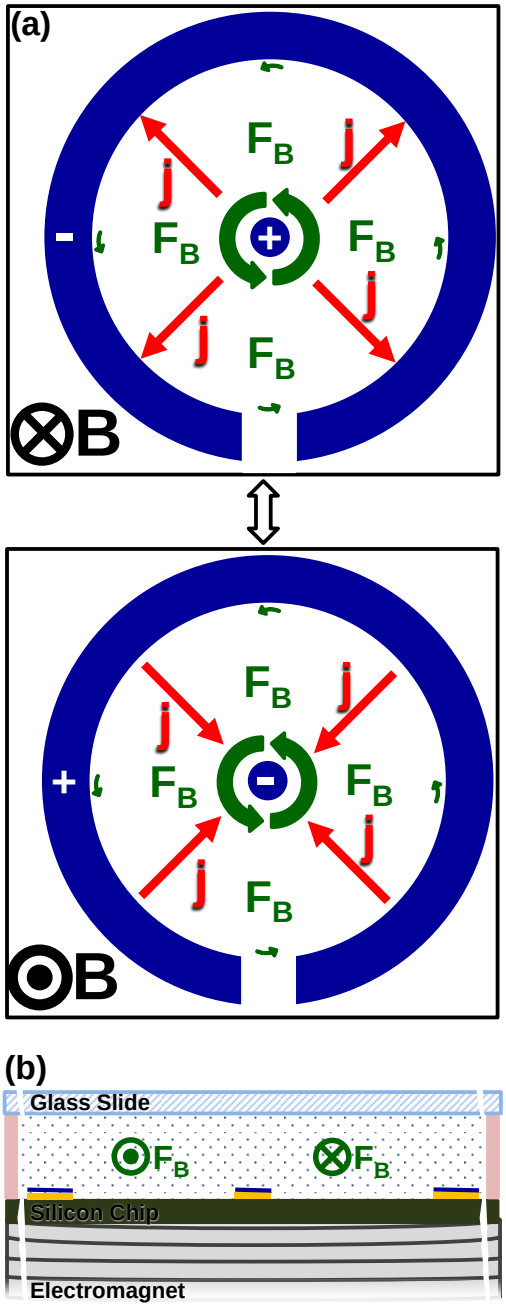

Figure 5.6 (a) Illustration of AC-MHD at PEDOT-modified concentric disk and ring microelectrodes. (b) Schematic of cross-section of chip, PDMS gasket, electrolyte, and glass slide.

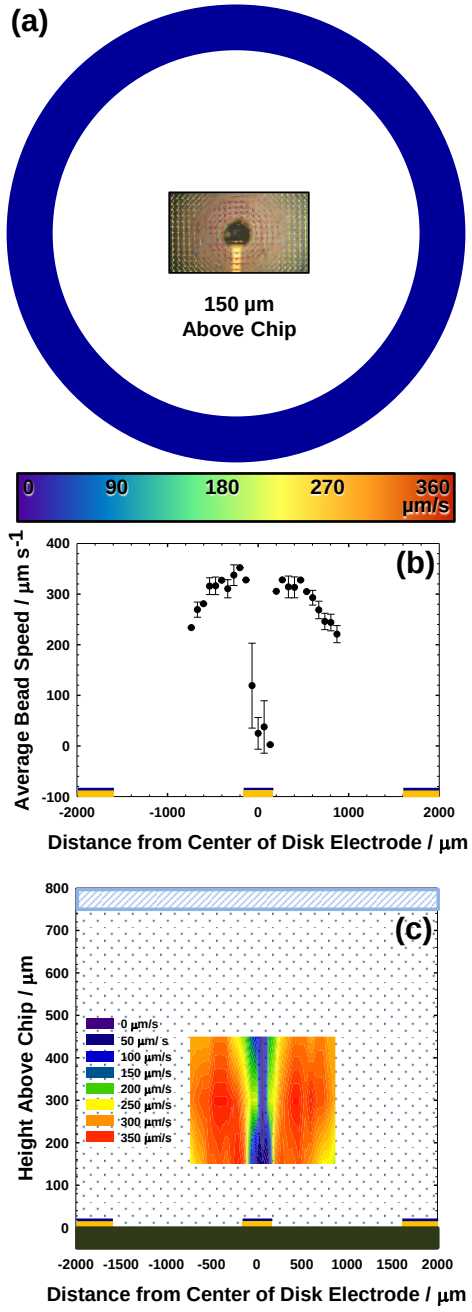

Figure 5.7 (a) PIV image of fluid flow recorded around the disk electrode at 150 µm above the chip. (b) Bead speed (µm·s^{-1}) versus the distance from the center of the disk electrode (µm). (c) Contour plot showing flow profile around the disk electrode throughout the height of the cell.

electrodes: the low speeds directly above the disk electrode. This feature is a reflection of the ionic current distribution. Directly over the disk electrode, the main component of the ionic current density is parallel to the B-field, which means it makes no contribution to the MHD force. As seen in Figure 5.7c, the highest fluid flow (350 $\mu m \cdot s^{-1}$) was observed at 300 µm above the chip and was located just outside of the disk electrode. These speeds are 10 times higher than DC-MHD experiments done at concentric disk and ring electrodes (that were half the area of the ring-disk set used in this study) for PEDOT-modified electrodes and 25 times higher than solution-based redox species. Fluid flow speed decreased radially from the disk electrode. Rotational convection of this velocity would certainly be of value for microfluidic mixing applications where laminar conditions exist.

5.5 Conclusions

In this study, a new microfluidic technique, AC redox-MHD was established. Through the ionic current density generated by PEDOT-modified electrodes and the AC-magnetic field generated by an electromagnet, continuous microfluidic pumping and rotational flow which would be useful for microfluidic mixing applications was demonstrated. This fluid manipulation was accomplished on a chip with no channels without the need of moving parts or valves. Future work will focus on using AC redox-MHD in a LOAC application.

5.6 Supporting Information

Video clips of microbead movement during AC redox-MHD experiments at PEDOT-modified electrodes showing flow patterns in the middle of the gap between working and counter microband electrodes while the relative phasing of the potential waveforms driving the electrodes

and the electromagnet is changing. Video of rotational flow at ring-disk electrodes is also shown. The supplemental section includes a discussion on the inductive heating of the magnet over time as well as the heat transfer to the solution in the cell. This material is available free of charge via the Internet at http://pubs.acs.org.

5.7 Acknowledgements

Research was supported through the National Science Foundation (NSF) (CBET-1336853) and the Arkansas Biosciences Institute, the major research component of the Arkansas Tobacco Settlement Proceeds Act of 2000. Research was also supported by an Electrochemical Society (ECS) Summer Fellowship to Christena K. Nash. We are grateful to Jerry Homesley for extensive discussions in designing the electronics for the power amplifier and electromagnet. We also want to extend our gratitude to Dr. Anupama Aggarwal and Dr. Vishal Sahore for fabricating the chip used in this study.

5.8 Abbreviations

MHD, magnetohydrodynamics; PEDOT, poly(3,4-ethylenedioxythiophene); SDS, sodium dodecyl sulfate; CA, chronoamperometry; CP, chronopotentiometry.

Notes

The authors declare the following competing financial interest(s): The author has declared a potential conflict of interest due to her equity stake of >5% in SFC Fluidics, LLC. Dr. Fritsch created intellectual property on redox-MHD which is licensed to SFC Fluidics.

5.9 References

(1) Figeys, D.; Pinto, D. *Analytical Chemistry* **2000**, *72*, 330 A-335 A.

(2) Haeberle, S.; Zengerle, R. *Lab on a Chip* **2007**, *7*.

(3) Abgrall, P.; Gue, A. M. *Journal of Micromechanics and Microengineering* **2007**, *17*, R15.

(4) Stone, H. A.; Stroock, A. D.; Ajdari, A. *Annu. Rev. Fluid Mech.* **2004**, *36*, 381-411.

(5) Weston, M. C.; Gerner, M. D.; Fritsch, I. *Analytical Chemistry* **2010**, *82*, 3411-3418.

(6) Ragsdale, S. R.; Lee, J.; White, H. S. *Analytical chemistry* **1997**, *69*, 2070-2076.

(7) Leventis, N.; Gao, X. *The Journal of Physical Chemistry B* **1999**, *103*, 5832-5840.

(8) Leventis, N. *J. Phys. Chem. B* **1998**, *102*, 3512-3522.

(9) Anderson, E. C.; Weston, M. C.; Fritsch, I. *Analytical Chemistry* **2010**, *82*, 2643-2651.

(10) Jang, J.; Lee, S. S. *Sensors and Actuators A: Physical* **2000**, *80*, 84-89.

(11) Pamme, N. *Lab on a Chip* **2006**, *6*, 24-38.

(12) Qian, S.; Bau, H. H. *Mechanics Research Communications* **2009**, *36*, 10-21.

(13) Bau, H. H.; Zhu, J.; Qian, S.; Xiang, Y. *Sensors and Actuators B: Chemical* **2003**, *88*, 205-216.

(14) Zhong, J.; Yi, M.; Bau, H. H. *Sensors and Actuators A: Physical* **2002**, *96*, 59-66.

(15) Homsy, A.; Koster, S.; Eijkel, J. C. T.; van den Berg, A.; Lucklum, F.; Verpoorte, E.; de Rooij, N. F. *Lab on a Chip* **2005**, *5*, 466-471.

(16) A. Homsy, S. K., J. C. T. Eijkel, A. van den Berg, E. Verpoorte, and N. F. de Rooija, Malmö, Sweden, Sept 26-30 2004.

(17) Weston, M. C.; Nash, C. K.; Fritsch, I. *Analytical Chemistry*, *82*, 7068-7072.

(18) Scrape, P. G.; Gerner, M. D.; Weston, M. C.; Fritsch, I. *Journal of The Electrochemical Society* **2013**, *160*, H338-H343.

(19) Sahore, V.; Fritsch, I. *Analytical chemistry*.

(20) Weston, M. C.; Nash, C. K.; Fritsch, I. *Analytical Chemistry* **2010**, *82*, 7068-7072.

(21) Weston, M. C.; Nash, C. K.; Homesley, J. J.; Fritsch, I. *Analytical Chemistry* **2012**, *84*, 9402-9409.

(22) Leventis, N.; Gao, X. *Analytical Chemistry* **2001**, *73*, 3981-3992.

(23) Cheah, L. T.; Fritsch, I.; Haswell, S. J.; Greenman, J. *Biotechnology and Bioengineering* **2012**, *109*, 1827-1834.

(24) Sahore, V.; Fritsch, I. *Analytical Chemistry* **2013**.

(25) Sahore, V.; Fritsch, I. *Microfluidics and Nanofluidics* **2014**, 1-8.

(26) Groenendaal, L.; Zotti, G.; Aubert, P. H.; Waybright, S. M.; Reynolds, J. R. *Advanced Materials* **2003**, *15*, 855-879.

(27) Lemoff, A. V.; Lee, A. P. *Sensors and Actuators B: chemical* **2000**, *63*, 178-185.

(28) Lee, C.-Y.; Chang, C.-L.; Wang, Y.-N.; Fu, L.-M. *International journal of molecular sciences*, *12*, 3263-3287.

(29) West, J.; Gleeson, J. P.; Alderman, J.; Collins, J. K.; Berney, H. *Sensors and Actuators B: Chemical* **2003**, *96*, 190-199.

(30) West, J.; Karamata, B.; Lillis, B.; Gleeson, J. P.; Alderman, J.; Collins, J. K.; Lane, W.; Mathewson, A.; Berney, H. *Lab on a Chip* **2002**, *2*, 224-230.

(31) Eijkel, J. C. T.; Dalton, C.; Hayden, C. J.; Burt, J. P. H.; Manz, A. *Sensors and Actuators B: Chemical* **2003**, *92*, 215-221.

(32) Kabbani, H. S.; Mack, M. J.; Joo, S. W.; Qian, S. *Journal of Fluids Engineering* **2008**, *130*, 091204.

(33) Nguyen, N.-T. *Microfluidics and Nanofluidics* **2012**, *12*, 1-16.

(34) Eijkel, J. C. T.; Dalton, C.; Hayden, C. J.; Burt, J. P. H.; Manz, A. *Sensors and Actuators B: Chemical* **2003**, *92*, 215-221.

5.S Poly(3,4-ethylenedioxythiophene)-Modified Electrodes for AC-Magnetohydrodynamic (AC-MHD) Microfluidic Pumping

Supporting Information

Video clips of microbead movement during AC redox-MHD experiments at PEDOT-modified electrodes are available here. Files are available showing flow between microband electrodes as the relative phasing of the potential waveforms of the electrodes and of electromagnet (5S_001.mpg) and flow around concentric ring-disk electrodes (5S_002.mpg). A graph showing the temperature increase of the electromagnet and the solution in the cell over time can also be found here for sine wave and square wave potential waveforms. A graph of fluid velocity vs relative phasing between the potential waveforms is also shown here.

5.S1 Captions to Video Clips

5S_001.mpg Video of microbead movement between working and counter/quasi-reference PEDOT-modified microband electrodes during an AC redox-MHD experiment. A 620 μm thick PDMS gasket was placed on the chip and filled with 325 μL of a solution containing 0.095 M NaCl and polystyrene beads. During this video, the relative phasing of the potential waveforms driving the electrodes and the electromagnet was being adjusted by 45˚ ever 10 s. For this video, the microscope was focused 300 μm above the chip surface.

5S_002.mpg Video of microbead movement between concentric PEDOT-modified ring-disk experiments during AC redox-MHD experiment. A 620 μm thick PDMS gasket was placed on the chip and filled with 325 μL of a solution containing 0.095 M NaCl and polystyrene beads.

5.S2 Temperature of Electromagnet and Solution in Cell over Time.

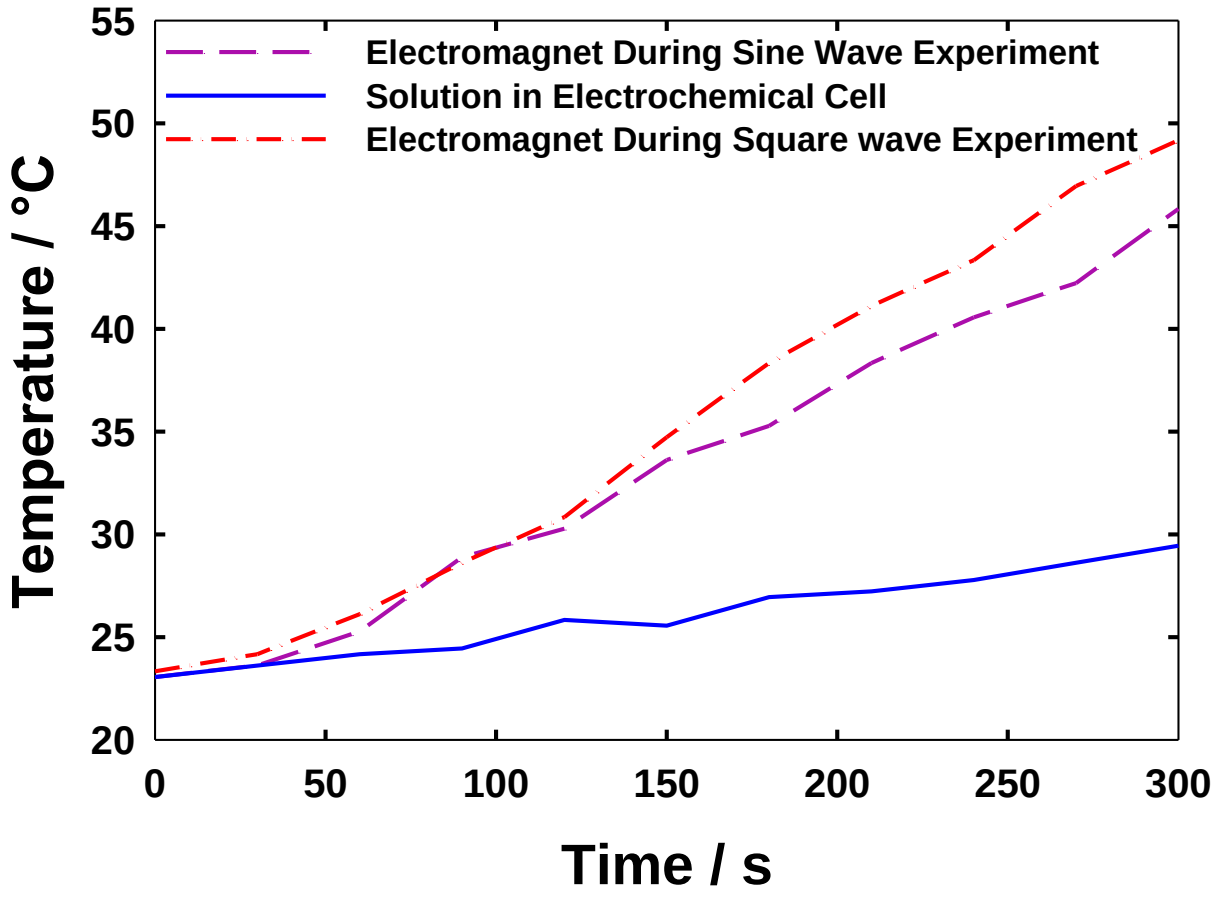

Figure 5.S1 Temperature of electromagnet and solution in electrochemical cell over time. Temperature readings were taken every 30 s. The electromagnet heated up dramatically over time from 23 ˚C initially to 115 ˚C after 5 min of use, in spite of the low frequency of switching. The heat shield paste did help to slow down the heat transfer from the electromagnet to the solution in the cell, thus, minimizing natural convection due to the solution heating.

5.S3 Relationship between Fluid Flow and Relative Phasing

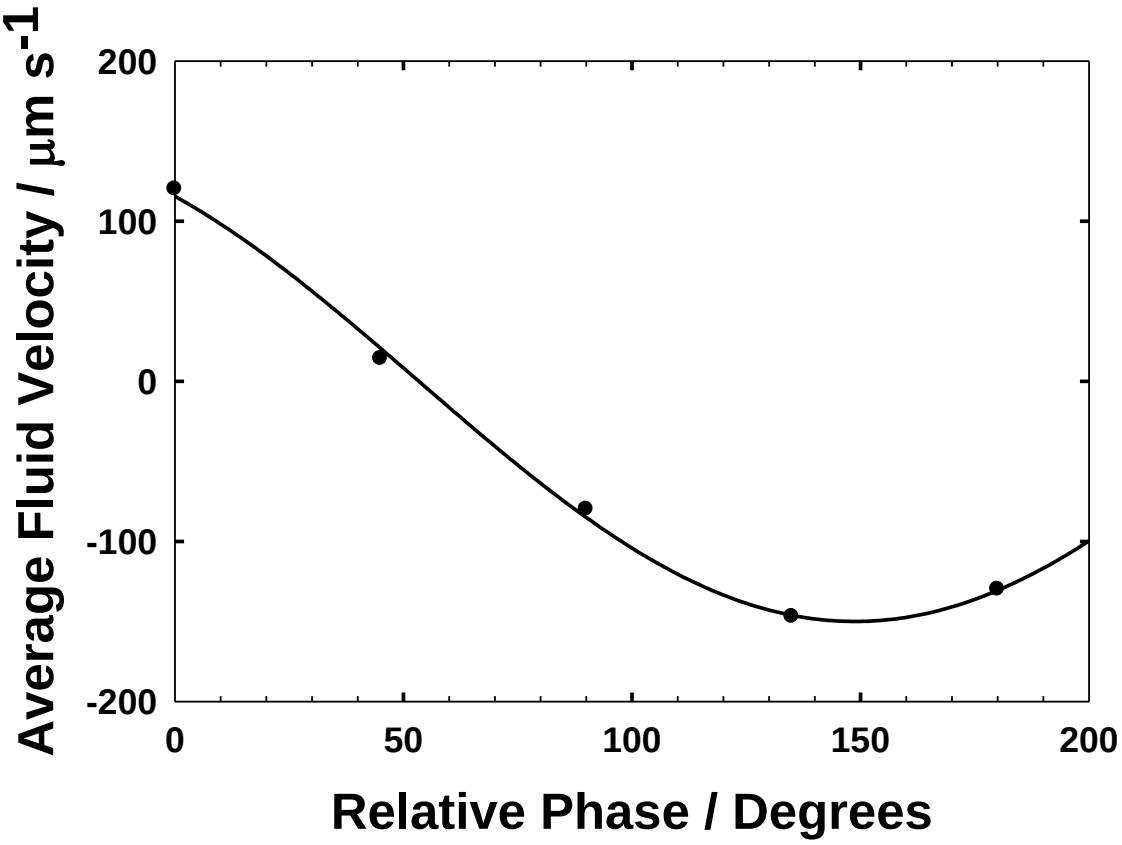

Figure 5.S2 Average fluid velocity vs the relative phase of the two square-wave potential waveforms (10 Hz) running to the electrodes and electromagnet.

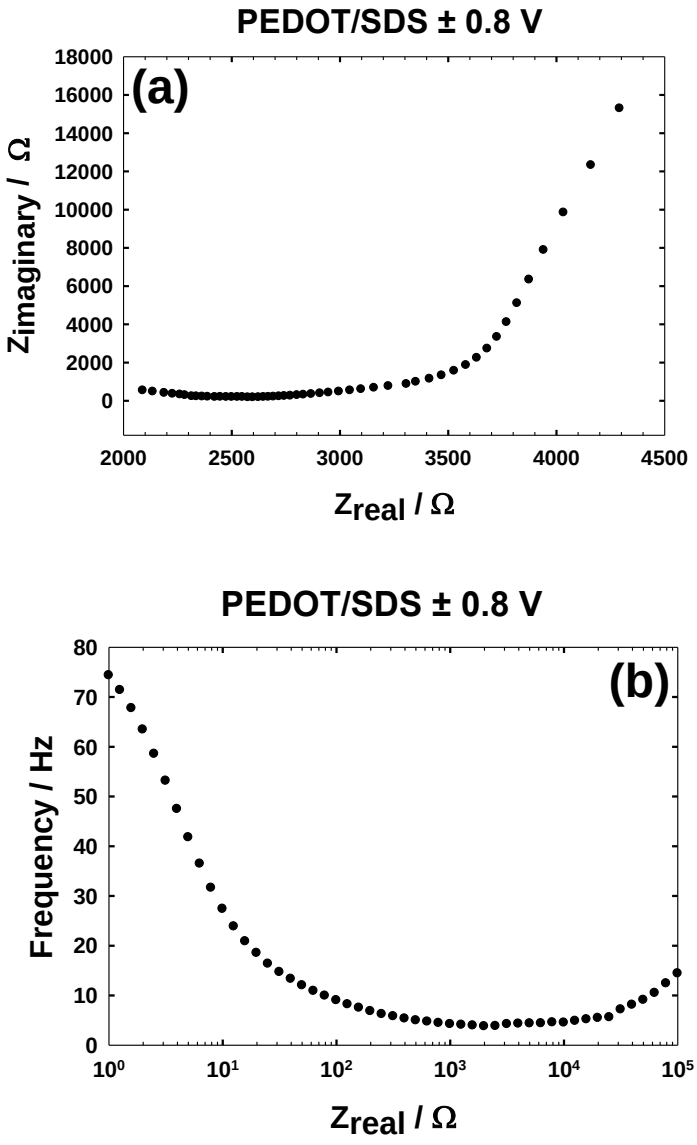

Figure 5.S3 EIS analysis of PEDOT-modified microelectrodes in 0.100 M NaCl. (a) Nyquist plot. (b) Bode plot.

6. Conclusions and Future Work

6.1 Conclusions

The work done in this dissertation demonstrates the usefulness of PEDOT-modified electrodes for redox-MHD convection. These modified electrodes are capable of high currents, and therefore, high fluid velocities without the presence of redox species in solution. This minimizes the risk of interference of detection of analytes for chemical analysis applications and reduces biocompatibility issues that can occur at high concentrations of redox species. The fluid flow presented around PEDOT-modified microband electrodes was shown to be fairly flat over long distances (5.6 mm) between the working and counter electrodes. This flat flow could be of use for separations applications or for delivery of components to specific sites on chip such as immunoassay applications or on-chip microreactors. In addition, the fluid velocity could be adjusted simply by adjusting the magnitude of the applied current, thus allowing for more fine-tuning of the microfluidic flow for the requirements of the applications. However, the amount of time that pumping can be sustained is a function of the current applied and the number of coulombs available within the PEDOT films. Once the coulombs are exhausted, the film must be electrochemically reversed before further pumping can occur. This could limit the number of microfluidic applications which would benefit from DC redox-MHD generated at PEDOT-modified electrodes. This problem was addressed in the previous chapter of this dissertation by taking advantage of the electrochemical reversibility of PEDOT.

Secondly, rotational fluid flow around PEDOT-modified concentric ring-disk microelectrodes was demonstrated. The fluid velocity was shown to be highest adjacent to the disk electrode and decreasing with radial distance from the disk. This generated a spiraling flow that could be of use for stirring applications and eventually mixing applications if the time that pumping can occur could be extended. Two electrochemical cell heights were examined in this work: 750 μm and 1050 μm. It was shown that the flow profiles between the chip surface and approximately 600 μm above the chip, where the flow was the highest, were very similar. Solution at the top of the electrochemical cell experienced very little fluid flow because the horizontal component of the ionic current density there is low. The linear dependence of the fluid velocity on the applied current and magnetic field strength was demonstrated. Unfortunately, the magnetic field strength is limited to what is commercially available. However, the magnitude of the current which can be applied is dependent on the properties of the PEDOT film. Even among

electropolymerized PEDOT films, there are a variety of procedures which can be found in the literature. The next chapter explored some of the deposition conditions which are responsible for the electrochemical properties of the film.

Work was done to electropolymerize PEDOT films which were capable of high coulombic capacity, fast current response, good electrochemical reversibility, and mechanical stability. To achieve this, several anionic solubilizers were explored with differing number of deposition cycles. The films were characterized visually with SEM to assess the morphology of the films. They were further characterized electrochemically in electrolyte alone using cyclic voltammetry, chronoamperometry, and electrochemical impedance spectroscopy. The monomer solution, which produced the films with the highest current response and coulombic capacity, contained EDOT and sodium dodecyl sulfate. These conditions were used for the final redox-MHD studies.

Finally, an AC-MHD approach was taken to solve the issue of limited time scales capable of PEDOT-modified electrodes. Due to the highly electrochemically reversible nature of PEDOT films, a sinusoidal potential waveform was used to discharge and charge the PEDOT films. A synchronized potential waveform of the same frequency was used to drive an electromagnet, generating an AC-magnetic field. In addition the use of a sinusoidal potential waveform to the PEDOT-modified electrodes switches the bias of the electrodes at such a rate that the transient faradaic current is observed. This increase in observed current can be seen from the high fluid velocities that occur in spite of the weaker magnetic field that is being produced (as opposed to the magnetic fields generated by permanent magnets). It was also demonstrated that careful control of the phasing of the AC electric and magnetic fields can be used to control the fluid flow speed and direction. The use of electromagnets does affect the portability of possible microfluidic devices from handheld devices to bench-top apparatuses. Nevertheless, the ability to pump continuously without channels or moving parts in common buffers and electrolytes with the ability to fine-tune fluid flow in different directions is powerful.

6.2 Future Work

The work contained in this dissertation explores the ability of PEDOT-modified electrodes to perform routine fluid handling needed in microfluidic applications such as pumping and stirring. The results suggest that microfluidic mixing and trapping of certain volumes of fluid could be possible at ring-

disk geometries. AC redox-MHD at PEDOT-modified electrodes is capable of continuous pumping or mixing without the need of redox species in solution, making it a viable microfluidic technique for chemical analysis applications and projects involving biological species. As of yet, AC redox-MHD has not been battletested. Therefore, future work must include a lab-on-a-chip application where it is used to accomplish the microfluidics.

To prove the worth of AC redox-MHD at PEDOT-modified electrodes as a microfluidic technique, an on-chip separation of neurotransmitters is proposed. The electrochemical detection of neurotransmitters, which are relevant to addition and diseases of the brain, has been an area of study in our lab. The brain has several neurotransmitters present including norepinephrine, dopamine, epinephrine, dihydroxyphenylacetic acid, and serotonin. All of these neurotransmitters are electrochemically active to some degree and have similar electrochemical responses.[1, 2] Thus, there is a need to separate the components prior to electrochemical detection.

MHD does not generated high pressures, but it can be easily miniaturized. Also, flow profiles can be tailored to improve separation efficiencies by controlling the current and magnetic field. For this application, the chip used in the MHD studies in this dissertation will be used to demonstrate the on-chip separation of two neurotransmitters. The microband electrodes (2.5 cm × 100 μm) on the chip will be modified with the conducting polymer PEDOT using a deposition solution containing 0.01 M SDS and 0.01 M EDOT, which was found to deposit ideal films for redox-MHD. The microband electrodes will be used to pump the sample and mobile phase through the stationary phase at a sufficient velocity to achieve efficient separation. The stationary phase will be made using acrylate chemistry that has been photoinitiated so that the polyacrylate can be deposited onto certain area of the chip using a mask. The stationary phase will be deposited on the ceiling also. This will create an open channel stationary phase for the neurotransmitters to interact with to achieve separation. MHD has been used chromatography applications in the past with limited success.[3]

Once the sample plug has been pumped through the area with stationary phase, it will reach a bare disk microelectrode where it will be detected using square-wave voltammetry without generating enough ionic current density to significantly affect the flow profile. If separation has been has been

achieved, the entrance and exit of each band of neurotransmitters should be evident from the current response over time. Figure 6.1 is an illustration of the stages of the on-chip separation.

6.3 References

(1) Vandaveer Iv, W. R.; Woodward, D. J.; Fritsch, I. *Electrochimica acta* **2003**, *48*, 3341-3348.

(2) Aggarwal, A.; Hu, M.; Fritsch, I. *Analytical and bioanalytical chemistry* **2013**, *405*, 3859-3869.

(3) Eijkel, J. C. T.; Dalton, C.; Hayden, C. J.; Burt, J. P. H.; Manz, A. *Sensors and Actuators B: Chemical* **2003**, *92*, 215-221.

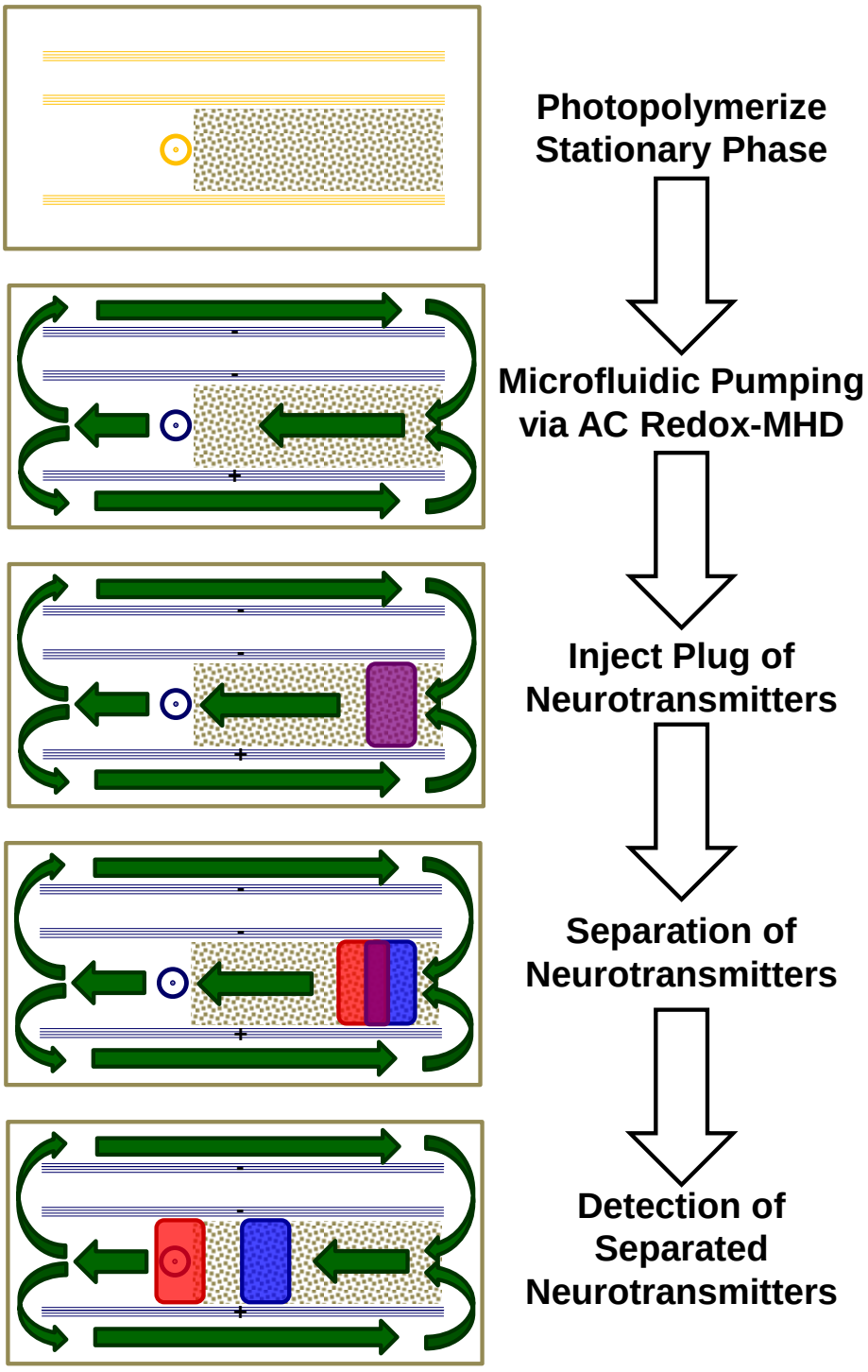

Figure 6.1 Illustration of different stages of the on-chip separation including photopolymerization of stationary phase, AC redox-MHD pumping, injection, separation, and detection of neurotransmitters.